INDUCING AND CHARACTERIZING STRUCTURAL CHANGES IN $RuO_2 \cdot xH_2O$

by

Zachary R. Cormier

Submitted in partial fulfillment of the requirements
for the degree of Master of Science

at

Dalhousie University
Halifax, Nova Scotia
August 2011

DALHOUSIE UNIVERSITY

DEPARTMENT OF CHEMISTRY

The undersigned hereby certify that they have read and recommend to the Faculty of Graduate Studies for acceptance a thesis entitled "Inducing and Characterizing Structural Changes in $RuO_2 \cdot xH_2O$" by Zachary R. Cormier in partial fulfillment of the requirements for degree of Master of Science.

Date: August 4th, 2011

Supervisors: _____

_____

Readers: _____

_____

_____

DALHOUSIE UNIVERSITY

DATE: August 4th, 2011

AUTHOR: Zachary R. Cormier

TITLE: Inducing and Characterizing Structural Changes in $RuO_2 \cdot xH_2O$

DEPARTMENT: Department of Chemistry

DEGREE: MSc CONVOCATION: October YEAR: 2011

_____

Signature of Author

TABLE OF CONTENTS

LIST OF FIGURES

ix

LIST OF SCHEMES

LIST OF TABLES

LIST OF ABBREVIATIONS AND SYMBOLS USED

°C	degrees Celsius
Å	Ångstrom
$\hbar$	reduced Planck's constant (6.582×10^{-16} eV·s)
δ_j	phase shift
δR	resolution in R-space
$\Delta \mu_0$	edge jump at the absorption edge
Δk	k range
ΔR	R range
θ	angle
λ	wavelength (Chapter 2.4), mean-free path (Chapter 2.5)
μ	absorption coefficient
μ_0	smoothed absorption background
μF	microfarads
μm	micrometer
π	pi
ρ	resistivity
σ	mean-square displacement (Debye-Waller factor)
σ^o	area of one gas molecule
χ	EXAFS intensity
A	Amp
A	cross-sectional area
Ag/AgCl	Ag/AgCl reference electrode
A_{sp}	specific surface area
B	full width at half maximum
BET	Brunauer-Emmet-Teller
c	BET constant
C	Coulomb
C	capacitance
CE	counter electrode
cm	centimeter

CV	cyclic voltammogram
d	interatomic spacing
DFT	density functional theory
DL	double layer
DOS	density of states
E	potential
E	X-ray energy
E_0	absorption edge energy
E^o	standard reduction potential
eV	electronvolt
EDS	energy dispersive spectroscopy
EXAFS	extended X-ray absorption fine structure
F	Farads
F	Faraday Constant (96 485 C mol^{-1}), backscattered amplitude (Chapter 2.5)
FLY	fluorescence yield
FT	Fourier transform
g	gram
G	energy
l	length
i	current-density
I	X-ray beam intensity after transmission
I_0	X-ray beam intensity before transmission
I_f	fluorescence intensity
k	wavenumber
K	shape factor
K-edge	excitation of 1s electrons
keV	kiloelectronvolt
kg	kilogram
kV	kilovolt
L-edge	excitation of 2s, 2p electrons
m	mass of an electron (9.11×10^{-31} kg)

m	meter
mA	milliamp
mg	milligram
mL	milliliter
mm	millimeter
mM	millimolar
mol	mole
mV	millivolt
M	molar
MΩ	megaohm
n	integer
N	coordination number
N_A	Avogadro's number (6.022×10^{23} mol^{-1})
N_{ind}	number of independent variables in a refinement
N_{max}	maximum number of independent variables in a refinement
nm	nanometer
PSD	pore-size distribution
PTFE	poly(tetrafluoroethylene)
q	scattering vector in SAXS
R	resistance (Chapter 1), bond distance (Chapter 2.5)
RE	reference electrode
s	second
S_0^2	amplitude scaling factor
SA	surface area
SAXS	small angle X-ray diffraction
SEM	scanning electron microscopy
SHE	standard hydrogen electrode
t	grain size (Chapter 2.4), sample thickness (Chapter 2.5)
TEM	transmission electron microscopy
TEY	total electron yield
TGA	thermogravimetric analysis

v	sweep rate
V	volt
V	volume adsorbed (Chapter 2.2), potential (Chapter 2.6)
V_m	volume of gas for monolayer coverage
WE	working electrode
x	partial pressure
XANES	X-ray absorption near-edge structure
XAS	X-ray absorption spectroscopy
XRD	X-ray diffraction

ABSTRACT

RuO$_2$/carbon composites have attracted a lot of attention for use as supercapacitor electrodes due to their high power and energy capabilities. Methods for loading the RuO$_2$ into the carbon include impregnation and electrochemical deposition. The first project involves impregnation of RuO$_2$ nanoparticles into a mesoporous carbon powder. Structural changes of the RuO$_2$ nanoparticles in the composite were induced by annealing at high temperatures, and X-ray diffraction (XRD) and X-ray absorption (XAS) were used to study the changes.

In situ electrochemical-XAS experiments were also developed and performed to study the structural stability of the RuO$_2$ nanoparticles in the composite as well as bulk RuO$_2$·xH$_2$O, with respect to changing potential.

Preliminary work on the electrodeposition of RuO$_2$·xH$_2$O onto Au foil and carbon cloth was performed. An electrode with a high specific capacitance of the RuO$_2$·xH$_2$O component was achieved. However, further studies need to be performed to optimize the deposition solution.

ACKNOWLEDGEMENTS

CHAPTER 1: INTRODUCTION

In recent years, the price and production reliability of fossil fuels has become a concern, so alternate sources of power are being aggressively sought, such as windmills, solar panels, *etc*. With these sources, the energy that is not immediately used must be stored. Also, combustion of said fossil fuels, such as gasoline in a vehicle engine, produces greenhouse gases and nitrogen oxides, which are harmful to the environment, so the development of emission-free, environmentally friendly energy/power sources is necessary. An alternative method for energy storage is through electrochemical reactions. The three most popular systems for electrochemical energy storage and production are fuel cells, batteries, and supercapacitors.[1, 2] There are common features to each of these systems, but they also have fundamental differences in the way the energy is stored and converted. Fuel cells and batteries primarily use Faradaic reactions for electrochemical energy storage, while supercapacitors store their charge either in an electrochemical double layer at an electrode/electrolyte boundary, or through fast, reversible Faradaic reactions called pseudocapacitance.[2] Pseudocapacitance will be described in further detail below.

When a solid (such as a supercapacitor electrode) is placed in contact with a solution (such as an electrolyte), a spontaneous separation of charge develops between the electrode surface and electrolyte based on either dissolution of electrode atoms into the electrolyte, or the adsorption of electrolyte ions onto the electrode surface.[2] This forms the electrochemical double layer, and this double layer can be used to store charge. The amount of charge stored can be increased by applying a voltage to the electrode, placing excess charges on the electrode surface and forcing ions (of the opposite charge)

1

from solution to arrange in the electrolyte near the electrode. When the electrode is disconnected from the power source and when no external circuit is provided for electron flow, the charge remains at the electrode/electrolyte boundary and is stored until an external circuit is provided (in the form of an electronic component by the user). The ability to store charge in this particular manner is called double-layer capacitance, and this is how many supercapacitors store most of their charge.[2]

More charge can be stored as the surface area of the electrode increases, therefore supercapacitors often utilize highly porous electrode materials. The double-layer capacitance has a rather complex relationship with the surface area, and this is due to several factors involving the pores. If the electrolyte ions are too large to fit down a pore, then that pore can not be used to add capacitance and the effective surface area of the electrode decreases.[3] Similarly, if the electrolyte ions are small relative to the pore size, the double layer is not formed as effectively because there is not a good attraction of the ions along the pore walls.[3] As the size of the pore decreases, the solution resistance increases meaning the ions move more slowly through the pores.[4] This is expressed by the following equation:[5]

$$R = \frac{\rho l}{A} \tag{1}$$

where R is resistance, ρ is resistivity, l is pore length, and A is the cross-sectional area of the pore. It should be noted that this equation is a simple model of the resistance in a pore, and is used for smooth, simple power, and would not accurately described an electrode with a complex pore structure. Increased solution resistance means that, at high sweep rates, the bottom of the pores are not used, which decreases the effective surface area of the electrode.[4] The accessibility to small pores (micropores) *via* larger pores

(mesopores) is important in double-layer capacitance as the mesopores are necessary for the fast transfer of ions from the depths of the micropores to the bulk of electrolyte solution. Most of these factors concerning pore size and the double layer are also important when performing electrochemical deposition of a material onto a high surface area electrode, which will be discussed in more detail below.

Supercapacitors that employ the double layer for their charge storage are also known as double-layer capacitors. They are advantageous over other energy storage systems because they have a higher power density, which is a result of the faster kinetics of charge rearrangement in the double layer versus the kinetics of charge transfer in redox reactions. This means that it is faster to move ions in and out of a double layer than to have a Faradaic reaction occur. The double layer has a time of formation of approximately 10^{-8} seconds, while a redox reaction is much slower at approximately 10^{-2} to 10^{-4} seconds.[1] Another main advantage of double-layer capacitors is the high cyclability of the electrochemical double layer charging, which can easily exceed one million cycles versus thousands of cycles for a Faradaic process.[1]

Another way in which supercapacitors store energy is through pseudocapacitance. Pseudocapacitance is a term which denotes a particular reaction as having the electrochemical characteristics of a capacitor, where the electron transfer is so fast the system is always at equilibrium.[6] The three main processes which can involve pseudocapacitive charge transfer are electrosorption, intercalation, and redox processes, with the latter being relevant to the present work.[4] These pseudocapacitive redox reactions occur in some transition metal hydrous oxides, including iridium oxide (IrO_2), manganese oxide (MnO_2), and ruthenium oxide (RuO_2).[6] Hydrous ruthenium oxide

($RuO_2 \cdot xH_2O$), in particular, has received a lot of attention due to its high capacitance of 720 F g^{-1} (when not in a composite).[7] A carbon double-layer electrode capacitance is only *ca.* 300 F g^{-1}. In addition, the $RuO_2 \cdot xH_2O$ component of a $RuO_2 \cdot xH_2O$/carbon composite has been shown to reach *ca.* 1500 F g^{-1}.[8] RuO_2 has been found to be more stable than other metal oxides,[9] and has a nearly constant current with change in potential (discussed below).[6] RuO_2 in its hydrous form is a mixed proton and electron conductor, while anhydrous RuO_2 is only an electron conductor, which helps to explain the extremely high capacitance of hydrous RuO_2.[10] The charge storage in $RuO_2 \cdot xH_2O$ occurs through a double-insertion of the electrons and protons into the structure:[11]

$$RuO_x(OH)_y + \delta H^+ + \delta e^- \rightleftharpoons RuO_{x-\delta}(OH)_{y+\delta}$$
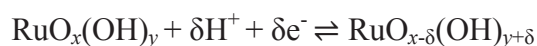
Scheme 1: Charge storage mechanism in $RuO_2 \cdot xH_2O$.

From the mechanism, it is seen that when the Ru^{4+} is reduced, protons enter the lattice and protonate the oxygens. It has been found that increasing the annealing temperature of $RuO_2 \cdot xH_2O$ decreases the water content and increases structural ordering in the material, thus changing the electron and proton conduction characteristics. Annealing at *ca.* 150 °C results in a molar ratio of *ca.* $RuO_2 \cdot 0.5H_2O$, which typically results in the highest energy storage capabilities.[12] One of the major disadvantages of RuO_2, as with IrO_2, is that it is expensive compared to other supercapacitor electrodes like carbon, which is relatively easily obtainable and inexpensive.[9] Currently, 100 g of an activated carbon powder is *ca.* \$20, while 1 g of hydrous RuO_2 is *ca.* \$60.

A typical cyclic voltammogram of a double-layer capacitor electrode (*e.g.* high surface area carbon) is similar to a regular capacitor in the fact that when the voltage (potential) switches direction, the current immediately switches from anodic to cathodic,

4

or *vice versa*, without a significant change in magnitude, and the cyclic voltammogram is a mirror image above and below the zero current line.[2] Ideally, the current of a capacitor is constant with potential, and this will result in a perfect rectangle on the cyclic voltammogram. However, with high surface-area carbons, there is often a dependence of the current on potential, giving rise to slight peaks on the cyclic voltammogram which are a result of pseudocapacitive redox reactions involving carbon surface functionalities. The primary carbon surface functionality thought to add pseudocapacitance are quinone groups, which would reduce to hydroquinones via the following reaction:[13]
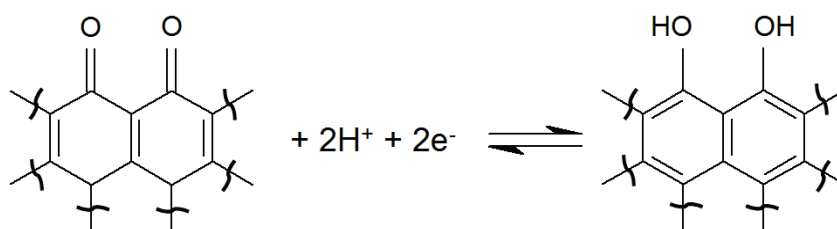
Scheme 2: Reduction of quinone (left) to hydroquinone (right).

The black curved lines in Scheme 2 represent bonds to the bulk carbon lattice. A typical cyclic voltammogram of a pseudocapacitive material like $RuO_2 \cdot xH_2O$ has characteristics similar to that of a double-layer capacitor, and is said to be reversible. In contrast, typical cyclic voltammograms of battery electrodes, which rely on normal redox reactions and not pseudocapacitive redox reactions, are not mirror images about the zero current line, and the current does not immediately change signs upon switching the voltage direction, and are said to be irreversible.[6]

A pseudocapacitive redox reaction, like those occurring with $RuO_2 \cdot xH_2O$ or carbon surface functionalities, has the capability of storing 1 or 2 electrons per surface atom, while the carbon electrode itself can only store *ca.* 0.18 electrons per surface atom in double-layer capacitance when using an aqueous electrolyte before the electrolyte

5

begins to break down.[2] The value of 0.18 electrons was estimated by Conway based on a capacitance of 30 μF cm^{-2}, 1×10^{15} atoms per cm^2, and a 1 V window.[2] More electrons can be stored per surface atom if the potential is increased, and higher potentials can be achieved using non-aqueous electrolytes.[2] It is clear that electrodes based on pseudocapacitive reactions would have higher energy capabilities than double-layer electrodes, but as mentioned previously, the double layer allows for higher power capabilities.[2] Thus an ideal electrode material would be a composite which consists of a small amount of the expensive RuO_2 loaded into an inexpensive activated carbon, with the RuO_2 providing high energy and the carbon providing high power.

Many methods have been developed for loading RuO_2 into or onto carbon, including colloidal[14] and sol-gel methods,[15] impregnation,[16] and electrodeposition,[17] just to name a few. Some syntheses involve the oxidation of the metal precursor $RuCl_3$ (Ru^{3+}) while others involve the reduction of $KRuO_4$ (Ru^{7+}).[18,19] The present work involves the synthesis of RuO_2/carbon composites through use of an impregnation method onto a mesoporous carbon powder, as well as electrodeposition onto a high surface area carbon fabric (Spectracarb 2225, 2131 m^2 g^{-1}).

The effect of annealing temperature on the structure RuO_2 has been investigated with X-ray diffraction (XRD), [14,20-22] and the degree of hydration of bulk RuO_2 has been studied using X-ray absorption spectroscopy (XAS).[10] However, to the best of our knowledge, the effect of annealing temperature on the structure of RuO_2 nanoparticles in a carbon nanocomposite, and the phase changes from hydrous RuO_2 to crystalline RuO_2, and eventually to metallic Ru is yet to be studied using XAS. It is important to understand the way that RuO_2 behaves as nanoparticles and films in a carbon composite,

rather on the bulk scale, as this is where RuO_2 may find the majority of its application. Also, the hydrous RuO_2 present is often amorphous, and in this case XRD (based on long range order) can give limited information relative to XAS (based on the local environment of the absorbing atom).

Background information for the various techniques and instruments used throughout this work is presented in Chapter 2, and the experimental information including instrument names, analysis conditions, and sample preparation is described in Chapter 3.

The composites made from an impregnation method are discussed in Chapter 4, and the goal was to determine the stability and structural changes of RuO_2 nanoparticles in a RuO_2/carbon composite with increasing annealing temperature. The composite was annealed at various temperatures ranging from 25 to 600 °C, and the resulting powders were examined using X-ray diffraction (XRD), transmission electron microscopy (TEM), cyclic voltammetry, and X-ray absorption Spectroscopy (XAS) at the Canadian Light Source (CLS) and Advanced Photon Source (APS) at the Argonne National Lab.

It was hypothesized that the RuO_2 was depositing in the pores of the mesoporous carbon in the composite described in Chapter 4. To determine if this were true, scanning electron microscopy (SEM), small angle X-ray scattering (SAXS), and Brunauer-Emmett-Teller (BET) measurements were performed on the composite annealed at 150 °C, and the results are presented in Chapter 5.

$RuO_2 \cdot xH_2O$ displays an extremely high capacitance, especially when in a carbon composite, and it is desired to understand how the structure of the RuO_2 changes with a change in potential. The goal of Chapter 6 was to develop and perform *in situ*

electrochemical-XAS studies at the CLS. The studies were performed on the 150 °C composite (Chapter 4), as well as bulk $RuO_2 \cdot xH_2O$ to observe changes in the Ru K-edge XAS spectra when the potential applied to the sample is changed.

Chapter 7 involves electrodeposition (through cyclic voltammetric deposition) of $RuO_2 \cdot xH_2O$ onto Au foil and carbon cloth. The goal of this chapter was to utilize different sweep rates to selectively deposit $RuO_2 \cdot xH_2O$ onto specific areas of the carbon cloth electrode and determine the effects on the capacitance of the composite.

2.1 ELECTRON MICROSCOPY

2.1.1 SCANNING ELECTRON MICROSCOPY (SEM) AND ENERGY DISPERSIVE SPECTROSCOPY (EDS)

The two types of electron microscopy used were scanning electron microscopy (SEM) and transmission electron microscopy (TEM). Unlike optical microscopy, where the image is produced by photons in the visible range of the electromagnetic spectrum, electron microscopy uses electrons to produce an image. Electrons can have shorter wavelengths than visible light photons, resulting in an electron microscope with higher resolving power than an optical microscope, while still having a large depth of focus.[23] The topography of the samples was examined using SEM, and an image is created by raster-scanning a sample using a high-energy beam of electrons. The electron source in SEM is called an electron gun, the most common being a tungsten filament cathode.[24]

The high-energy electrons from the electron gun interact with the sample surface either elastically (changing trajectory but not significantly changing energy) or inelastically (transfer of all or part of the electron energy to the solid). Elastically scattered electrons eventually leave the surface as backscattered electrons, while inelastically scattered electrons can produce either secondary electrons or X-ray fluorescence. Secondary electrons are a result of interactions between the high-energy electrons and weakly bound conduction electrons in the solid, causing ejection of the conduction band electrons.[24] X-ray fluorescence occurs when a high-energy electron excites a core electron from an atom, leaving a core-hole. When an electron from an outer orbital fills the core-hole, energy is released in the form of an X-ray which is characteristic of the type of element.[25] The backscattered and secondary electrons are

detected using an electron detector (typically a scintillation detector),[24] while an additional X-ray detector is required if Energy Dispersive Spectroscopy (EDS) studies of the X-ray fluorescence are to be performed. In EDS, the fluorescence X-rays from the sample are detected by a semiconductor detector, and typically all X-rays lines are measured simultaneously.[25]

There are a variety of sample holders available for SEM that can accommodate solids of many sizes and types (glasses, powders, cloths, *etc.*). Commonly, a two-sided piece of conductive tape is used to hold the sample on the stub, and to allow for grounding of the sample. If the sample is insulating, it must first be coated with a conductive metal such as gold to help ground it and prevent build-up of static electric charge. This build up of charge is known as charging, and can be seen as bright areas on the sample and causes a poor image.[24] High electron conductivity often correlates with high thermal conductivity, and coating a sample can therefore reduce the possibility of thermal degradation as well.[25]

2.1.2 TRANSMISSION ELECTRON MICROSCOPY (TEM)

In TEM, it is the electrons that are transmitted through the sample that are detected, rather than those scattered from the sample, as in SEM. The transmitted electrons are focussed and magnified by magnetic lenses, and imaged onto a sensing screen.[23] The intensity of the transmitted electron beam depends on the thickness of the sample, as well as the atomic number of the elements in the sample. Elements with a larger atomic number scatter electrons more than those with a smaller atomic number, and thus appear as darker areas on a TEM image.[23] In order for electrons to be passed

through the specimen, the specimen must often be less than 100 nm thick and can require an involved sample preparation, unless it is nanoparticles which are being imaged.

2.2 BRUNAUER-EMMET-TELLER (BET) ISOTHERMS

BET isotherms give useful information on the specific surface area of a sample, and can be further used to determine pore-size distribution. In a BET gas adsorption experiment, gas molecules, typically N_2 or Ar, are passed through a sample chamber and adsorb onto the surface of the solid sample.[23] Measuring the gas flow in and out of the sample chamber allows the volume of gas adsorbed on the sample to be determined, and from this the specific surface area, A_{sp}, can be calculated using the formula:[23]

$$A_{sp} = \frac{V_m N_A \sigma^o}{22414} \tag{2}$$

where V_m is the volume of gas needed for monolayer coverage, N_A is Avogadro's number, σ^o is the cross-sectional area of one gas molecule (1.62×10^{-19} m^2 for N_2) adsorbed to the substrate surface, and the value 22414 is the molar volume of the gas, in cm^3 mol^{-1} at standard temperature and pressure. Unlike the Langmuir isotherm which describes only chemisorption of a monolayer, BET theory has no limitation to the number of layers of molecules which adsorb to the surface, with the first layer being chemisorbed and the following layers being physisorbed. Therefore, V_m must be calculated from the total volume adsorbed, V, which can be done using the BET equation:[23]

$$\frac{V}{V_m} = \frac{cx}{(1-x)[1-(1-c)x]} \tag{3}$$

where c is the BET constant and x is the partial pressure, p/p_0. The BET equation can be rearranged into a linear form, and from the slope and intercept the V_m can be calculated. Performing density functional theory (DFT) calculations on the BET isotherm results in a

pore-size distribution.[26] For BET experiments, the sample must be solid and fit in the sample chamber.

2.3 THERMOGRAVIMETRIC ANALYSIS (TGA)

Thermogravimetric analysis is a technique in which the mass of a sample is measured continuously as the temperature of the sample is increased. The mass (or mass percent) can be plotted as a function of either temperature or time, and the analysis is performed in a controlled environment (oxidizing, reducing, inert, *etc.*) by gas flow.[25] If desired, the atmosphere may be changed while the analysis proceeds by changing the type of gas in the system. The balance in a TGA instrument typically has a range of 5 to 20 mg. The sample holder is in the furnace of the instrument while the rest of the balance is thermally isolated from the furnace. Ideally, the temperature recorded in TGA is the exact temperature of the sample, but in reality the temperature of the sample lags or leads the recorded temperature by a small amount because the thermocouple is not located inside the sample. If the thermocouple is inside the sample, it can result in contamination and weighing errors, so the thermocouple is placed very close to the sample, and only a small amount of sample is used.[25]

The information TGA provides can be limited compared to other thermal methods, as it is necessary there be a change in mass. However, TGA is useful in characterizing oxidation and decomposition reactions, as well as vaporization, sublimation, and desorption processes.[25] If one knows approximately at which temperatures certain processes will occur (*e.g.* desorption of CO and CO_2 species from carbon, water loss from RuO_2, or decomposition from RuO_2 to Ru) then original concentrations or molar ratios can be calculated from the mass difference.

Thermogravimetric analysis is typically performed on solids, but has been used to study liquids as well.[27] For sample preparation, the sample must be small enough to fit in the sample pan.

2.4 X-RAY DIFFRACTION (XRD) AND SMALL ANGLE X-RAY SCATTERING (SAXS)

The scattering of X-rays by a material occurs when the electric vector of electromagnetic radiation interacts with the electrons of the atoms comprising the material.[25] If the wavelength of the incident X-rays is on the same order of magnitude as the interatomic spacing (Angstroms), and the atoms are highly ordered as in a crystal, then constructive and destructive interference of the scattered X-rays occurs, resulting in diffraction of the X-rays. X-ray diffraction is often described using the Bragg equation:[25]

$$n\lambda = 2d \sin \theta \tag{4}$$

where n is an integer, λ is the X-ray wavelength (typically 1.54 Å for a Cu Kα radiation source), d is the interatomic spacing, and θ is the incident angle of the X-ray beam. Constructive interference only occurs at angles which satisfy the Bragg equation and destructive interference occurs at all other angles. A representation of the diffraction of X-rays by a crystal is shown in Figure 1.
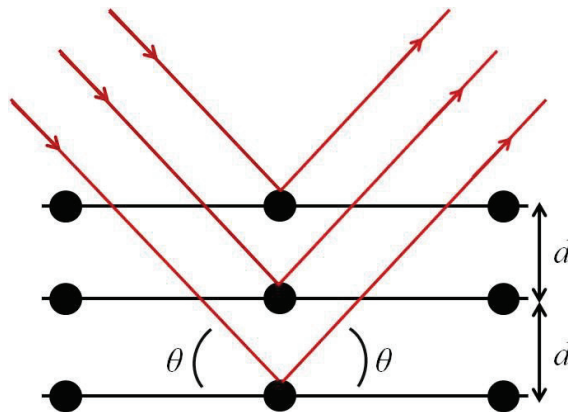
Figure 1: Diffraction of X-rays by a crystal.

The interatomic spacings in a crystal can be calculated from the peak positions in an X-ray diffraction (XRD) pattern using the Bragg equation. The Scherrer equation can then be used to approximate the size of the crystal grains (or particles) in the sample. The Scherrer equation is described by:[28]

$$t_{(hkl)} = \frac{K\lambda}{B_{(hkl)}\cos\theta} \tag{5}$$

where t is the grain size, K is the shape factor (typically $0.89 \leq K \leq 1.0$, depending on the distribution of grain sizes), λ is the incident X-ray wavelength, B is the full width at half maximum (FWHM) of the peak, θ is the Bragg angle, and (hkl) is the Miller index for the crystal plane from which the peak arises.

Small angle X-ray scattering (SAXS) relies on the scattering of X-rays as they travel through contrasting electron densities in a sample at very small angles.[29] A typical SAXS profile is a log-log plot of the intensity of the transmitted X-rays (I) through a sample as a function of the wavevector (q). The scattering vector can be calculated using the equation:[30]

$$q = \frac{4\pi}{\lambda}\sin\theta \tag{6}$$

where λ and θ are the incident X-ray wavelength and Bragg angle, respectively. The SAXS profile has a maximum intensity at $0°$ when the detector is directly in line with the X-ray source. As the angle is increased, the detected X-ray intensity decreases. However, scattering of the transmitted X-rays from contrasting electron densities in the sample causes broad features in the SAXS profile. The SAXS profile can be fit using a model equation which accurately describes the sample to obtain values related to pore size

and/or particle size, and their relative contributions. The following model was used for the carbon samples in this work:[31]

$$I(q) = \frac{A}{q^n} + \frac{Ba_1^6}{\left(1 + a_1^6 q^2\right)^2} + \frac{Ca_2^6}{\left(1 + a_2^6 q^2\right)^2} + D \tag{7}$$

where a_1 and a_2 represent two characteristic pore dimensions (Debye correlation lengths) in the medium, A is a bulk scattering contribution, B is the contribution from small pores of correlation length a_1, C is the contribution from larger pores of correlation length a_2, D is a constant background contribution and n is to account for smearing effects from having fixed slits rather than a pinhole.

As SAXS relies on contrasting electron densities, it can be used to study both crystalline and amorphous particles in a medium, as well as voids in the medium. Furthermore, it is the particle size in the medium which is determined from the SAXS profile and not the grain size (as in XRD). Grain size and particle size are not necessarily the same magnitude if the particle is polycrystalline (Figure 2).[31]
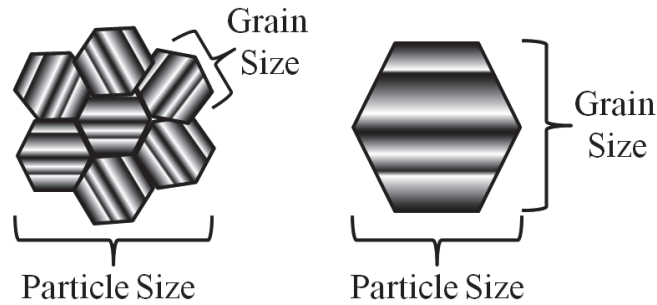
Figure 2: Conceptual difference between grain size and particle size.

If a large amount of powder is to be used in an XRD experiment, a sample holder is used which has a hollow space, and the powder must be packed such that it is level with the top of the sample holder. If a small amount of powder is used, it can be

deposited directly onto a zero background wafer (typically Si) to minimize any competing diffraction lines that may be caused by the holder. In SAXS, the sample is held in a vertical sample holder between two windows which are transparent to X-rays, typically polyimide film.

2.5 X-RAY ABSORPTION SPECTROSCOPY (XAS)

In X-ray absorption spectroscopy (XAS), a core-level electron from either the K-edge (1s), L-edge (2s, 2p), or M-edge (3s, 3p, 3d) is excited by absorption (destruction) of a photon. The excited electron is called a photoelectron, and the excitation process is referred to as the photoelectric effect.[32] Core-level electrons have specific binding energies associated with them which makes XAS an element-specific technique, and it can therefore be useful in characterizing elements of low abundance. Crystallinity is not necessary for XAS, and measurements can be performed on solid, liquid, or even gas phase species.[33] These factors, among others, make XAS ideal for studying RuO_2/carbon composites, which can contain low loadings of non-crystalline RuO_2.

The probability of an X-ray being absorbed is described by:[33]

$$I = I_0 e^{-\mu t} \tag{8}$$

where I is the transmitted X-ray intensity, I_0 is the incident intensity, t is the sample thickness, and μ is the absorption coefficient. At most energies, μ is a smooth function of energy. However, when the X-ray energy reaches the binding energy of a core electron, an absorption edge results (Figure 3). For measurements collected in transmission mode, the energy dependence of the absorption coefficient can be written as:[33]

$$\mu(E) = \log\left(\frac{I_0}{I}\right) \tag{9}$$

16

The energy dependence of the absorption coefficient can also be described for fluorescence mode by:

$$\mu(E) \propto \left(\frac{I_f}{I_0}\right) \tag{10}$$

where I_f is the fluorescence intensity emitted from the sample.

A typical XAS spectrum collected at high energies (>2000 eV) can be divided into two main regions; the X-ray Absorption Near-Edge Structure (XANES) and the Extended X-ray Absorption Fine Structure (EXAFS), as indicated in the Figure 3.
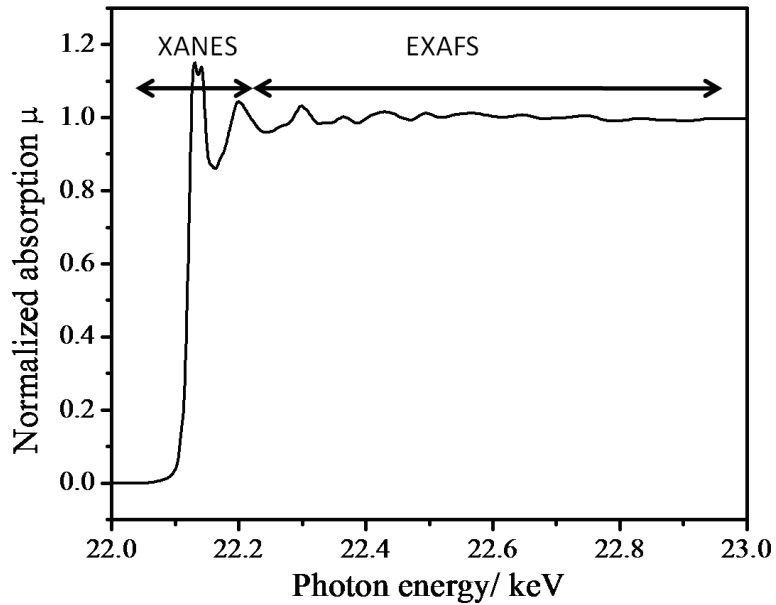
Figure 3: XAS spectrum of RuO$_2$ showing XANES and EXAFS regions.

The XANES region contains the absorption edge, and extends to *ca.* 30 eV above and below the edge. XANES is sensitive to the oxidation state and coordination environment of the absorbing atom. The EXAFS region is comprised of low-intensity oscillations, and provides information on bond distance (R), coordination number (N), and species of neighbouring atoms. Often, it is useful to express the measured absorption coefficient, $\mu(E)$, in terms of the XAFS spectrum, $\chi(E)$:[33]

17

$$\chi(E)=\frac{\mu(E)-\mu_0(E)}{\Delta\mu_0(E)} \tag{11}$$

where μ_0 is a smoothed background representing the absorption of a single atom, and $\Delta\mu_0$

is the edge jump at the absorption edge energy, E_0. The EXAFS region can be converted

to the k-space, with the photon energy being converted to the photoelectron wavenumber

using the formula:[33]

$$k=\sqrt{\frac{2m(E-E_0)}{\hbar^2}} \tag{12}$$

where m is the mass of an electron, and $\hbar$ is the reduced Planck's constant. Therefore, the

function $\chi(E)$ becomes $\chi(k)$, which describes the oscillations in the EXAFS as a function

of the wavenumber. An example of a typical k-space spectrum is shown in Figure 4a.
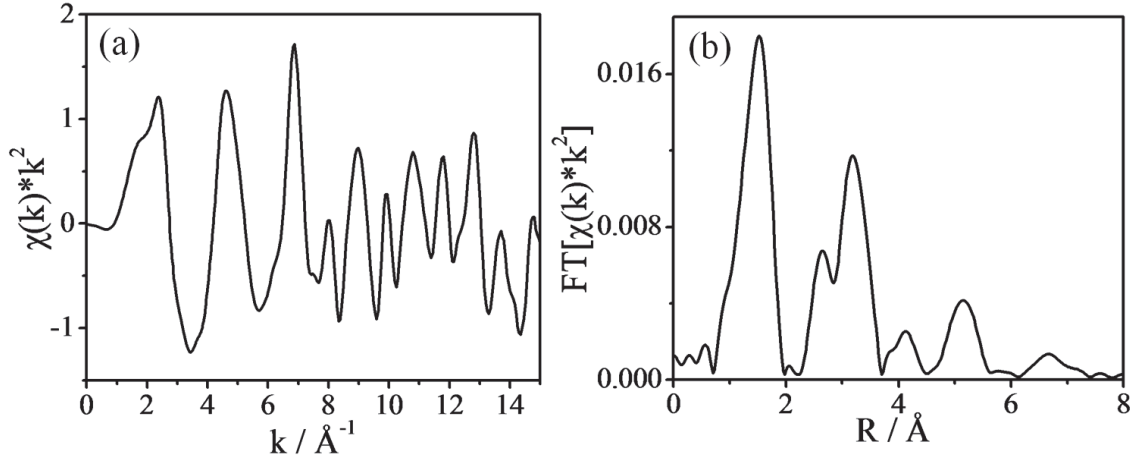
Figure 4: Typical k-space (a) and R-space (b) spectra of RuO_2.

The oscillations at higher k values are often low in intensity, and are increased by

multiplying $\chi(k)$ by k^2 or k^3. This is indicated in the y-axis label of Figure 4a. Typically

the k weighting is an integer, although any value could theoretically be chosen.

According to theory, $\chi(k)$ can be modeled using the EXAFS equation:[33]

$$\chi(k) = \sum_j \frac{N_j S_0^2 F_j(k)}{k R_j^2} e^{(-2k^2\sigma_j^2)} e^{(\frac{-2R_j}{\lambda})} \sin\left[2kR_j + \delta_j(k)\right] \tag{13}$$

where N_j is the number of neighbouring atoms of the *jth* type, at an interatomic distance R_j from the excited atom, with a Debye-Waller factor σ_j to account for thermal vibrations and static disorder. $F_j(k)$ is the backscattered amplitude, S_0^2 is an amplitude scaling factor to account for multielectron excitations, λ is the photoelectron mean-free path, and δ_j is the total phase shift experienced by the photoelectron. The $\chi(k)$ is essentially a sum of dampened spherical waves, and therefore can be deconvoluted into its constituent frequencies by a Fourier transformation (FT) of the k-space into the R-space, shown in Figure 4b. The R-space is a more intuitive representation of the EXAFS data, where the peaks correspond to groups of atoms at different distances (referred to as shells). The peak positions and intensities are analogous to, but do not directly correspond to, the distance of the shell and the coordination number of the shell, respectively. However, as seen in the EXAFS equation, the peak positions are shifted (typically by *ca.* -0.5 Å) and there are many factors which affect peak intensity.

The exact values for R, N, and σ^2 can be obtained by refining the experimental data. A list of coordinates for atoms in the theoretical structure (RuO_2 or metallic Ru in this work) is produced by generating a model cluster. This can be done using a variety of programs, including CrystalMaker software.[34] The program FEFF8 is then used to simulate the XAS spectrum based on an *ab initio* self-consistent multiple scattering code using Green's functions to simulate fine structure.[35] Computations begin by calculating the electronic structure of each of the atom types in the material, as isolated free atoms. The electronic structures are then superimposed onto the desired geometry, given by the

atomic coordinates, and averaged to create a muffin-tin potential with a certain amount of overlap.[33] The muffin-tin approximation estimates atomic potentials as spherically symmetric out to a finite radius, and the remaining interstitial region potential is approximated as constant. The mean-free path of the photoelectron is then calculated, as well as the primary scattering paths and their amplitudes.[33] For the EXAFS region, the FEFF8 output contains a list of the theoretical bond distances and coordination numbers which are then used to refine the experimental EXAFS using WinXAS software.[36] FEFF8 can also calculate the theoretical XANES spectrum, as well as local density of states (lDOS) information.

Synchrotron radiation is used to perform XAS because the X-rays produced are intense, collimated and tuneable. In a synchrotron, electrons are accelerated to relativistic speeds, where changes in acceleration are induced by magnetic fields, generating the electromagnetic radiation. The radiation is then collimated, filtered, and monochromated through a beamline, which is where the experiment is performed.[33]

2.6 ELECTROCHEMICAL MEASUREMENTS

Electrochemistry experiments were performed using a three electrode system. The working electrode is the electrode on which the reaction of interest is occurring. The reference electrode is the electrode to which all of the potential measurements on the working electrode are referenced, and the counter electrode is the electrode from and to which the current from the working electrode flows.[2] Cyclic voltammetry experiments were performed on the working electrode by varying the applied potential of the electrode and measuring the current that results. The applied potential is initiated at E_1 and then swept linearly to some other potential E_2 and back to E_1, producing a triangular (or saw-

20

tooth) potential wave.[2] The rate at which the potential changes as a function of time is termed the "sweep rate".

The capacitance (C) of the working electrode can be determined from the cyclic voltammogram through the following equation:

$$C=i/v \tag{14}$$

where i is the current-density and v is the sweep rate. The energy of the electrode can then be determined from the equation:[2]

$$G=\left(\frac{1}{2}\right)CV^2 \tag{15}$$

where G is the energy, C is the capacitance and V is the voltage.

Cyclic voltammetry can also be used to deposit a species in solution onto a substrate electrochemically.[37] In general, one begins with a metal salt, M^{n+} (where n is an integer), of which the standard reduction potential (E^o) is known. The potential of the electrode is cycled negative of the E^o on the reverse scan of the cyclic voltammogram, and the metal salt is reduced onto the working electrode. Upon sweeping the potential in the positive direction, a portion of the reduced metal will be re-oxidized, although much will remain deposited. In other words, the cathodic current (due to reduction) will be greater than the anodic current (due to oxidation).[38] Subsequent sweeps in the cyclic voltammogram will deposit more and more of the metal species onto the electrode. The cycling is continued until a desired thickness of the electrodeposited species is achieved, or until a plot of the current against cycle number no longer increases linearly. In the latter case, either less of the species is being deposited, or that which is being deposited is less electroactive, which is undesirable in a supercapacitor electrode.[38] The electrodeposition conditions, including the solution pH, supporting electrolyte, upper and

lower limits of the cyclic voltammogram, temperature, stirring, *etc.* can play an important

role in the deposited species.[38]

CHAPTER 3: EXPERIMENTAL

3.1 MATERIALS USED

Mesoporous carbon powder (100 Å pore size), graphite powder, ruthenium (III) chloride hydrate ($RuCl_3 \cdot xH_2O$, ReagentPlus grade), potassium chloride (KCl, 99.999 %), hydrochloric acid (HCl, 37 wt. % in water, 99.999 %), and conc. sulphuric acid (H_2SO_4, 99.999 %) were obtained from Sigma-Aldrich Co. Ruthenium (IV) oxide hydrate ($RuO_2 \cdot xH_2O$, 99.99 %) was obtained from Alfa Aesar. Sodium hydroxide (NaOH, min. 97.0 %) and sodium bicarbonate ($NaHCO_3$, 100.0 ± 0.3 %) were obtained from ACP Chemicals Inc. Potassium nitrate (KNO_3, reagent grade) was obtained from Caledon Laboratories Ltd. The water used was 18 MΩ water. The Spectracarb 2225 carbon cloth was purchased from Engineered Fibers Technology LLC.

3.2 SYNTHESIS OF $RuO_2 \cdot xH_2O$/CARBON NANOCOMPOSITES

The $RuO_2 \cdot xH_2O$/carbon nanocomposites were prepared using impregnation followed by oxidation, as demonstrated previously in the literature. [39] The term "nanocomposite" is used throughout Chapter 4, rather than composite, to signify that the RuO_2 is on the nano scale. Approximately 50 mg of mesoporous carbon powder was added to 15 mL of 16 mM $RuCl_3$ aqueous solution and stirred for 24 hours. The Ru^{3+}/carbon powder was then suction-filtered, washed thoroughly with water, and redispersed in water by sonicating the filter paper for *ca.* 15 seconds. The powder was then stirred for 24 hours in 30 mM HCO_3^- aqueous solution, causing [$Ru(OH)_3$] to precipitate onto the carbon. This powder was collected as before, and the deposition process was repeated with two more iterations. The resulting powder was annealed at either 25 °C (non-annealed), 100 °C, or 150 °C for 22 hours. To further study the effects

of elevated temperature on the 150 °C composite, this sample was annealed at either 200 °C, 300 °C, 350 °C, 400 °C, 500 °C, or 600 °C for 22 hours in an inert atmosphere. The inert atmosphere was chosen for the higher temperatures to prevent the carbon from burning off during the annealing process.

Additional samples were prepared, including an unloaded mesoporous carbon sample from the same process as the 150 °C RuO_2/carbon nanocomposite, except in the absence of $RuCl_3$. This powder will be referred to as the blank carbon. Also, a sample was prepared from the same process as the RuO_2/carbon nanocomposite, but in the absence of carbon and only one iteration was performed. The $[Ru(OH)_3]$ that precipitated was annealed at 150 °C for 22 hours. These two samples were prepared to help further characterize the 150 °C RuO_2/carbon nanocomposite. Annealing at 150 °C forms $RuO_2 \cdot 0.5H_2O$, which is thought to be the best material for charge storage as a supercapacitor electrode.[12,10] The structure of the RuO_2 nanoparticles in all nanocomposites were investigated using XAS (at the Ru K and L_3-edges) and XRD. The 150 °C nanocomposite was further characterized using TGA, TEM, cyclic voltammetry, and *in situ* XAS. The results are presented in Chapter 4.

3.3 ELECTRON MICROSCOPY AND EDS

For SEM and EDS, the powder sample was mounted on the stub using double-sided carbon tape. Excess powder was blown off the stub using a compressed air canister. The SEM instrument used was a Hitachi S-4700, coupled with an Oxford Instruments Inca x-sight EDS system. For TEM, the powder samples were dispersed in water and deposited onto a formvar/carbon-coated 300-mesh Cu grid via water evaporation. The

TEM instrument used was a JEOL JEM 1230, operated at 80 kV, and the images were captured with a Hamamatsu ORCA-HR digital camera.

3.4 BET MEASUREMENTS

The two BET instruments used were the Micrometrics ASAP 2000 and the Micrometrics Flowsorb II 2300, both from Folio Instruments Inc. The gas being adsorbed onto the sample was N_2 for both instruments. Before taking any measurements, the sample had to first be degassed to remove any unwanted molecules which may have been attached to the surface. The time allotted for the degassing was 24 hours for the carbon samples which were run on the Micrometrics ASAP 2000, and 30 minutes for the carbon samples run on the Micrometrics Flowsorb II 2300. When the sample was run on the Micrometrics Flowsorb II 2300 instrument, only a single point measurement of the surface area was obtained. The information from the Micrometrics ASAP 2000 instrument was analyzed using the Micrometrics program ASAP 2010 V. 4.00 to obtain the surface area. The BET isotherm was imported into the Micrometrics program DFT-plus, which calculated the pore-size distributions of the sample.

3.5 THERMOGRAVIMETRIC ANALYSIS

TGA studies were performed in an alumina pan with a ramp rate of 5 °C min^{-1} from 30 to 580 °C in argon gas to determine the degree of hydration of the 150 °C sample. Also, TGA studies were performed with a ramp rate of 20 °C min^{-1} from 30 to 900 °C in air to determine the RuO_2 loading in the 150 °C sample. Approximately 7 mg of sample was used. The thermogravimetric analyzer used was a TA Instruments SDT-Q600.

3.6 XRD AND SAXS

For X-ray diffraction (XRD), the samples were deposited on a Si(100) wafer via ethanol evaporation. The X-ray diffraction patterns were collected on a JD2000 diffractometer equipped with a diffracted beam monochromator and a Cu-target X-ray tube. The patterns were collected from 10 to 90°, in 0.05° increments with a dwell time of ten seconds (s). SAXS measurements were made on a Siemens D5000 diffractometer equipped with a Cu-target and a graphite monochromator. The measurements were collected in transmission mode, with the sample held between two polyimide film windows in a vertical sample holder. The patterns were collected from 0.3 to 15°, in 0.02° increments with a dwell time of five seconds.

3.7 XAS

Ru K-edge (22117 eV) data were collected at the Hard X-ray MicroAnalysis (HXMA) beamline of the Canadian Light Source (CLS, operated at 2.9 GeV) and the Pacific Northwest Consortium Collaborative Access Team (PNC-CAT) beamline of the Advanced Photon Source (APS, operated at 7 GeV). The HXMA beamline has an energy range of 5 to 40 keV, and is equipped with a Si(220) monochromator and platinum mirrors, and the PNC-CAT beamline energy range is 2.7 to 35 keV, and is equipped with a Si(111) monochromator. For the *ex situ* samples, the pre-edge range was collected from -200 to -30 eV below the adsorption edge, in 10 eV steps and a 1 s dwell. The XANES region was collected from -30 eV below the absorption edge to 80 eV above the absorption edge, in 0.35 eV steps and a 1 s dwell. The EXAFS region was collected from 80 eV above the edge to 16 k, in 0.05 k steps with an 8 s dwell. The *in situ* parameters were the same except for the EXAFS region, which was collected to 14 k and with a 12 s

dwell. For *ex situ* measurements, the samples were loaded into a polyimide film cell and scanned using transmission or fluorescence modes. The sample preparation for the i*n situ* measurements is discussed below.

Ru L_3-edge (2838 eV) data were collected at the Soft X-ray Microcharacterization Beamline (SXRMB) of the CLS, which has an energy range of 1.7 to 10 keV. The samples were attached to the sample holder using double-sided carbon tape. The pre-edge region was collected from 2800 to 2835 eV in 0.5 eV steps. The XANES region was collected from 2835.15 to 2885.3 eV in 0.15 eV steps. The region above the edge was collected from 2885.8 to 2930 eV in 0.5 eV steps. XANES spectra were recorded in total electron yield (TEY) and fluorescence yield (FLY) simultaneously using specimen current and multichannel plate detectors, respectively. FLY is bulk sensitive while TEY is surface sensitive, and thus these complementary yields can give information on the overall structure and composition of the RuO_2 nanoparticles.[40] XAS data from both the K and L_3-edges were analyzed using WinXAS software.

In the XAS theoretical calculations, the atomic coordinates used in the FEFF8 input files were taken from models of anhydrous rutile ruthenium dioxide and hexagonal close-packed (HCP) metallic ruthenium (Figure 5), which were created in the CrystalMaker program.
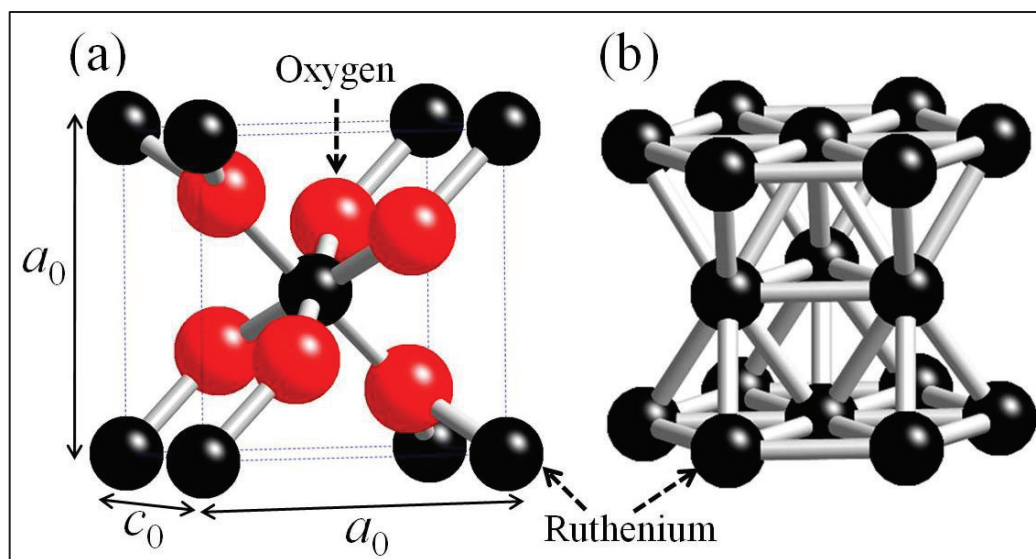
Figure 5: a) Anhydrous rutile ruthenium dioxide structure (tetragonal unit cell) and b) metallic ruthenium structure (hexagonal close-packed). Ruthenium atoms (black) and oxygen atoms (red) are labelled.

Rutile RuO_2 (Figure 5a) has unit cell dimensions of $a_0 = 4.51$ Å and $c_0 = 3.11$ Å, and the Ru atoms are octahedrally coordinated to six surrounding O atoms; four at 1.98 Å and two at 1.94 Å. The shortest Ru-Ru distance is 3.11 Å along the c-axis of the unit cell, corresponding to a coordination number (N) of 2.[12] The next shortest Ru-Ru distance is 3.54 Å from the central Ru to the corner Ru atoms, and thus corresponds to a N of 8.[12] Metallic ruthenium (Figure 5b) has first nearest neighbours located at 2.68 Å, with a N of 12.

3.8 ELECTROCHEMISTRY

The electrochemical cell used for the cyclic voltammetry measurements on prepared RuO_2/carbon powder nanocomposites (Chapter 4) was a three-compartment all-glass cell with a three electrode setup. The reference electrode used was a standard hydrogen electrode (SHE) and the counter electrode used was a piece of Spectracarb 2225 carbon cloth, wrapped in Pt wire for electrical contact. The working electrodes were

ca. 3 mg of sample pressed against a sticky carbon (1:1 mixture of graphite to beeswax) current collector held in a Teflon Swagelok system PFA tube fitting. The electrolyte was bubbled with N_2 at least one half hour prior to experiments and during the experiments. Electrical contact was made with the sticky carbon via a platinum wire sealed in a glass tube. The electrolyte used was 1.0 M H_2SO_4. The cyclic voltammetry experiments in Chapter 4 were originally performed from 0.0 to 1.0 V, but due to a large cathodic reduction at potentials below 0.4 V which originated from the sticky carbon (observed in other studies), the potential window was changed to 0.4 to 1.1 V. The upper limit of the cyclic voltammogram was increased to 1.1 V because, as Equation 15 shows, a larger potential window results in more energy being stored. The applied sweep rates ranged from 0.5 to 50 mV s^{-1}.

The electrochemical cell used for electrochemical deposition (Chapter 7) was a one-compartment glass cell of approximately 100 mL volume. The working electrode was either *ca.* 1 cm × 1 cm piece of gold foil attached to gold wire, or a *ca.* 1 cm diameter piece of Spectracarb 2225 carbon cloth in a custom-made holder, attached to a gold wire. The reference electrode used was a Ag/AgCl electrode (0.222 V vs. SHE) and the counter electrode used was a piece of Spectracarb 2225 carbon cloth, wrapped in Pt wire for electrical contact. All experiments were conducted at 22 ± 3 ^{o}C, and the instrument used for all measurements was either a Princeton Applied Research (PAR) VMP3 multi-potentiostat under EC-Lab software control, or CHI 660C Electrochemical Workstation. The cyclic voltammetry deposition experiments for Chapter 7 were conducted with potential windows of either -0.2 to 1.0 V or -0.2 to 0.8 V, at sweep rates ranging from 1 mV s^{-1} to 50 mV s^{-1},. Cyclic voltammetry experiments on the prepared composites were

performed in 1.0 H_2SO_4, bubbled with N_2 at least one half hour prior to the experiments and during the experiments. The potential windows used for these studies were -0.2 to 1.0 V, 0.0 to 1.0 V, 0.2 to 0.8 V, and 0.4 to 0.6 V vs. Ag/AgCl and sweep rates ranged from 0.5 to 50 mV s^{-1}.

3.9 *IN SITU* ELECTROCHEMICAL-XAS

In situ electrochemical-XAS experiments were conducted (at the CLS) on the 150 °C nanocomposite (described in Chapter 4) and bulk $RuO_2 \cdot xH_2O$ (from Alfa Aesar) to observe changes in the Ru K-edge XAS spectra with changes in potential. The working electrode was made from sticky carbon (*ca.* 10 mm × 10 mm × 5 mm) formed around platinum wire, with approximately 3 mg of sample pressed on one 10 mm × 10 mm face.

A three electrode setup was used with a poly(tetrafluoroethylene) [PTFE] cylindrical vial (*ca.* 13 mm diameter and 53 mm height) as the electrochemical cell. The reference electrode used was a Ag/AgCl electrode (0.222 V vs. SHE) and the counter electrode was a piece of platinized platinum mesh. The electrolyte was 1.0 M H_2SO_4, and all potentials were referenced to the Ag/AgCl electrode. The electrolyte was bubbled with N_2 for one half hour before experiments, but not during the experiments. The instrument used for these measurements was a CHI 660C Electrochemical Workstation.

The working electrode in the electrochemical cell was placed in the X-ray beam path at the HXMA workstation. The working electrode was held at either a reducing potential (0.0 V for the 150 °C nanocomposite and 0.2 V for the bulk $RuO_2 \cdot xH_2O$) or oxidizing potential (1.0 V for both samples), and Ru K-edge data were collected at these potentials. Note that 0.0 V vs Ag/AgCl is *ca.* 0.2 V vs. SHE. As mentioned, the cathodic reduction seen in the cyclic voltammograms originated from the sticky carbon substrate,

but its presence is not consistent. As the cathodic wave was absent for this particular electrode, lower potentials could be used than in the cyclic voltammetry experiments on the 150 °C composite (Chapter 4).

CHAPTER 4: ON THE TEMPERATURE DEPENDENT STRUCTURE OF RU IN A RuO₂/CARBON NANOCOMPOSITE

4.1 INTRODUCTION

The present work involves characterization of $RuO_2 \cdot xH_2O$/carbon nanocomposites annealed at various temperatures ranging from 25 °C (non-annealed) to 600 °C. The structure of the RuO_2 nanoparticles were investigated using XAS (at the Ru K and L_3-edges) and XRD. The 150 °C nanocomposite was further characterized using TGA, TEM, cyclic voltammetry, and *in situ* XAS.

4.3 RESULTS AND DISCUSSION

4.3.1 XRD

Figure 6a shows the offset XRD patterns for the nanocomposites annealed from 25-600 °C. The broad peaks seen for the 25 and 100 °C nanocomposites indicate that the RuO_2 present is amorphous. The peak positions and intensities for the 150, 200 and 300 °C nanocomposites are similar to those seen in the XRD pattern for rutile RuO_2 (ICDD #43-1027) suggesting that the RuO_2 nanoparticles present in these samples have the rutile structure. Also, the peak positions and intensities for the 400, 500, and 600 °C nanocomposites are similar to those seen in the XRD pattern for metallic Ru (ICDD #89-4903), suggesting that metallic Ru nanoparticles are present in these nanocomposites.
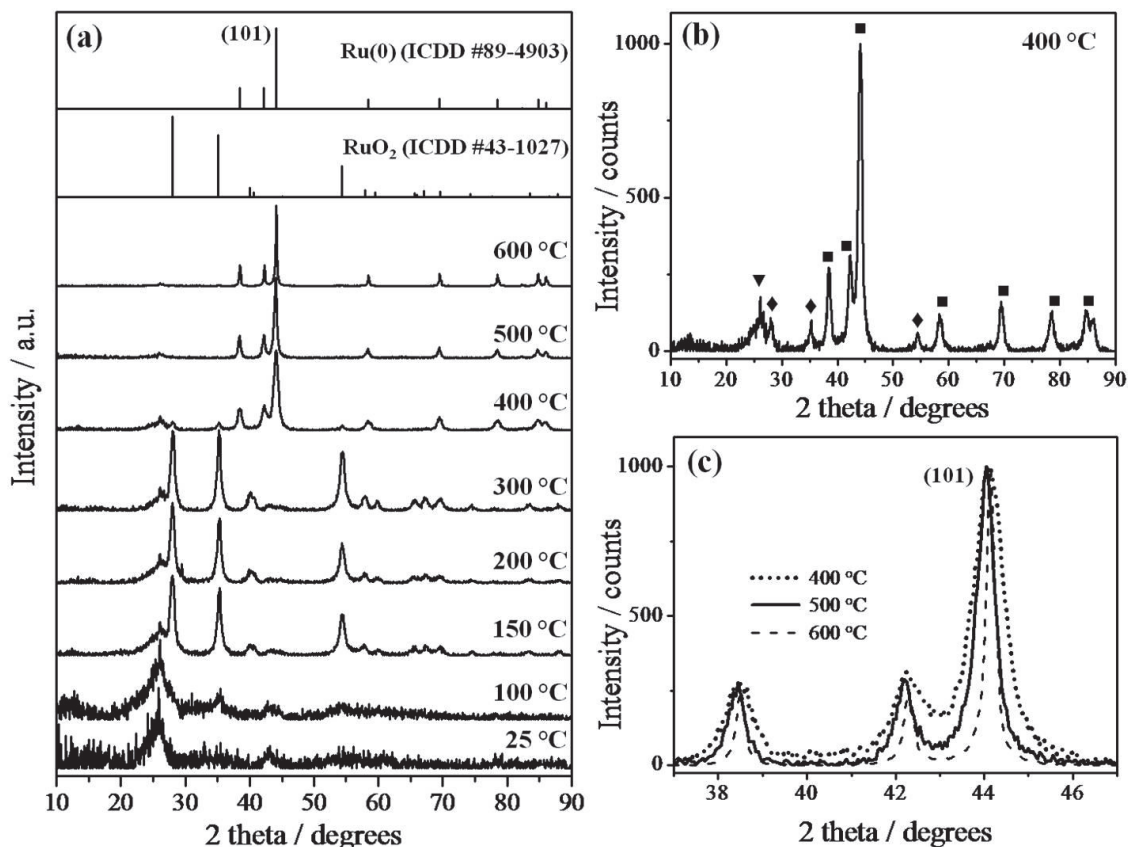
Figure 6: a) XRD patterns of all nanocomposites, and literature patterns for anhydrous rutile RuO$_2$ (ICDD #43-1027) and metallic Ru (ICDD #89-4903). b) 400 °C nanocomposite pattern only, with peaks from carbon, RuO$_2$ and Ru(0) indicated by ▼, ♦, and ■ respectively. c) Overlain 400 to 600 °C patterns to show peak narrowing.

Based on Figure 6a, the Ru-containing nanoparticles present in the nanocomposites change from amorphous to crystalline RuO$_2$ between 100 and 150 °C, and from crystalline RuO$_2$ to metallic Ru between 300 and 400 °C. In literature, the transition from amorphous to crystalline RuO$_2$ in similar RuO$_2$/carbon composites occurs at higher temperatures, from just above 200 °C (see references [18, 41]) to as high as 400 °C.[15, 42] This suggests that the RuO$_2$ in our impregnation synthesis develops long range order at lower temperatures than in literature, while still maintaining hydration, as indicated by the TGA results below.

Figure 6b contains the XRD pattern of the 400 °C sample alone, as to more clearly see the features present. The peak at 26.5°, indicated by the inverted triangle symbol, is a result of the (002) reflection plane in graphitic carbon.[43] This same peak is also visible in most patterns in Figure 6a and most prominently in the 25 and 100 °C samples. The peaks of low intensity in Figure 6b at 28.1°, 35.1°, and 54.4°, indicated by the diamond symbol, are a result of the (110), (101), and (211) reflection planes in rutile RuO_2, respectively.[44] Finally, the most intense and well-defined peaks in Figure 6b are indicated by the square symbol, and are a result of metallic Ru (ICDD #89-4903). The peaks at 38.4°, 42.2°, 44.1°, and 58.5° correspond to the (100), (002), (101), and (102) reflection planes in metallic Ru, respectively. This XRD pattern indicates that by annealing at 400 °C, a nanocomposite was produced which contains both rutile RuO_2 and metallic Ru nanoparticles, and thus represents a thermal phase transition from the metal oxide to the pure metal. This phase change occurs at a lower temperature than for bulk RuO_2.[45] This can possibly be attributed to the fact that RuO_2 in the nanocomposite is in direct contact with carbon, which has been shown to aid in the reduction metal oxides to metals.[46] Conversely, this could be regarded as the catalytic oxidation of the carbon powder by RuO_2.[47] A RuO_2/carbon composite with 3 nm RuO_2 particles prepared by Kim et al.[14] did not show crystallinity until annealing at 200 °C, suggesting that the lower transition temperature is not a result of the higher surface area associated with nanoparticles compared to bulk RuO_2. The intensities of the peaks indicate that at this temperature, there is much more metallic Ru present than RuO_2, which will also be confirmed with XAS below. The fact that XRD peaks from the metal oxide are still visible after the phase change has begun shows that the RuO_2 maintains its long-range

order throughout the phase change process. The amount of hydration of the RuO_2 present, if any, can't be deduced from the XRD patterns alone.

In Figure 6a, as the annealing temperature is increased from 150 to 300 °C, the peaks in the corresponding XRD patterns narrow. This same trend occurs in the metallic Ru nanocomposites as the annealing temperature increases from 400 to 600 °C. To more clearly see this trend, Figure 6c contains a magnification of the overlain 400 °C (dotted line), 500 °C (solid line) and 600 °C (dashed line) XRD patterns.

The size of the RuO_2 and metallic Ru nanoparticles in the annealed nanocomposites was estimated from the XRD patterns using the Scherrer equation. For the RuO_2 containing nanocomposites (150, 200, and 300 °C), the particle size of the RuO_2 was calculated based on the (101) and (211) peaks, and the uncertainty was calculated from the deviation of these two values. The size of the metallic Ru nanoparticles in the 400, 500, and 600 °C nanocomposites were calculated from the (100) and (102) peaks in the respective XRD patterns, and all particle sizes are presented in Table 1. It should be noted that although RuO_2 peaks were also observed in the 400 °C sample along with the metallic Ru peaks, they were of such a low intensity that the Scherrer equation could not be accurately applied.

Table 1: Estimated particle sizes from XRD.

Nanocomposite	Particle structure	Particle size / nm
150 °C	RuO_2	10 ± 2
200 °C	RuO_2	11 ± 2
300 °C	RuO_2	11 ± 2
400 °C	Ru(0)	10 ± 1
500 °C	Ru(0)	19 ± 3
600 °C	Ru(0)	35 ± 2

The RuO_2 particle sizes in the 150, 200 and 300 °C nanocomposites were *ca.* 10 nm. The results indicate that there is no statistically relevant change in the size of the RuO_2 particles in this temperature range, within one standard deviation. The RuO_2 particles are therefore stable against aggreagation with respect to temperature in the range of 150-300 °C. However, the size of the metallic Ru nanoparticles in the 400, 500, and 600 °C nanocomposites increase drastically, and are therefore less stable with respect to temperature changes than RuO_2. It has been found that RuO_2 bonds to carbon through Ru-O-C interactions,[48,49] and this may aid in the structural stability of the RuO_2 nanoparticles in the nanocomposites. These bonds are thought to be formed with carboxylic oxygens on the carbon surface.[48] It was found that carboxylic oxygen groups can be released from carbon as CO_2 and CO beginning at temperatures of around 200 °C from carbon fibers in a study by Zielke *et al*.[50] The exact temperature of release of these groups varied between different samples, but CO_2 was most strongly released at *ca.* 300 °C and CO at *ca.* 600 °C from the carbon fibers.[50] It is thought that a similar process is occurring in the mesoporous carbon powder used in this synthesis. The release CO_2 and

CO might break the Ru-O-C bonds and cause the resulting metallic Ru nanoparticles (annealed at 400 to 600 °C) to be less stable than their RuO_2 counterparts.

It should be noted that an XRD pattern was collected on the RuO_2 sample prepared in the absence of carbon (annealed at 150 °C), which showed broad diffraction peaks indicating an amorphous structure of the RuO_2. There is clearly an interaction between the RuO_2 and the carbon in the nanocomposite material which results in crystalline RuO_2 being present in the 150 °C nanocomposite. It is important to understand the structural stability of RuO_2 nanoparticles in composites, including the present temperature-induced phase changes, as well as changes due potential as in the *in situ* XAS studies below.

4.3.2 TEM

Transmission electron microscope (TEM) images were taken of the various nanocomposites prepared. Figure 7 shows TEM images of the 150 °C (a) and 600 °C (b) nanocomposites.
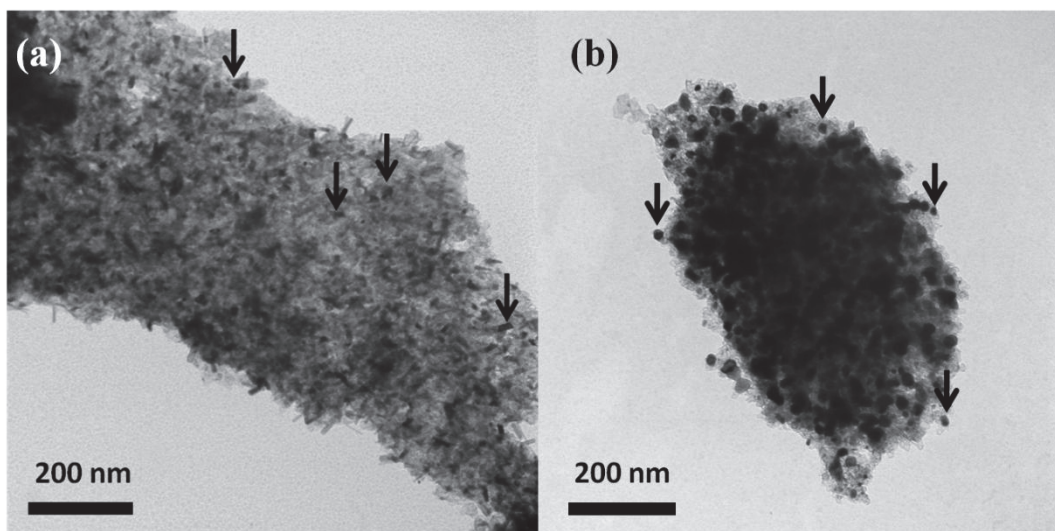
Figure 7: TEM images of a) 150 °C and b) 600 °C nanocomposites. The dark spots, some of which are marked by arrows, are a) RuO$_2$ nanoparticles and b) metallic Ru nanoparticles.

It can be seen that the carbon powder has many darker areas (some of which are indicated by arrows), which are thought to be RuO$_2$ and metallic Ru nanopoarticles in (a) and (b), respectively. Ruthenium has a much larger atomic number than carbon and thus would appear darker in a TEM image because the electrons would not be transmitted as easily. From the TEM images, the majority of the RuO$_2$ nanoparticles are in the range of 4-18 nm in the 150 °C nanocomposite, and 13-40 nm in the 600 °C nanocomposite. These ranges encompass the nanoparticle size estimated from the XRD patterns.

4.3.3 TGA

Thermogravimetric analysis was performed on the 150 °C nanocomposite, as well as the blank carbon sample to determine the degree of hydration in the RuO$_2$ nanoparticles present in the 150 °C sample and also to track the RuO$_2$ decomposition with increasing temperature. The blank carbon sample was used as a reference so that any weight loss from the carbon powder could be removed from the 150 °C nanocomposite

spectrum, and the resulting TGA scan would represent only weight loss from the RuO_2 nanoparticles. Note that the TGA was performed in argon, so decomposition of the carbon is not expected, but weight loss due to adsorbed species may occur. The background-subtracted TGA scan is shown in Figure 8.
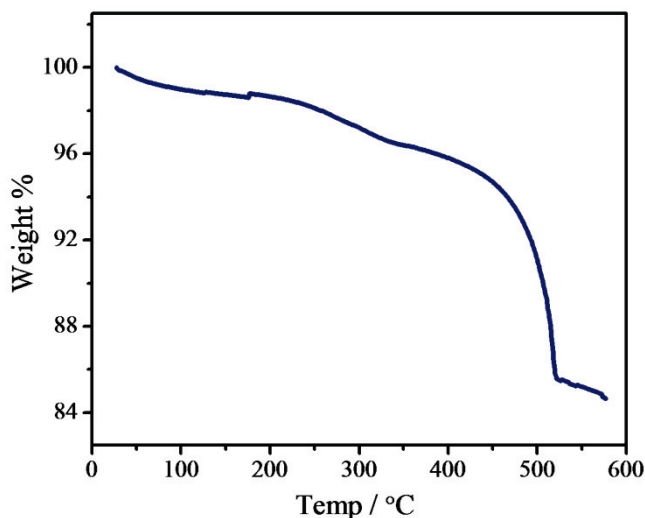
Figure 8: TGA scan in argon for the 150 °C nanocomposite. Temperature ramp rate was 5 °C min^{-1}. The weight loss beginning at *ca.* 350 °C corresponds to loss of O_2 and transition from RuO_2 to metallic Ru.

There is a gradual weight loss from 25 °C to *ca.* 325 °C, before a more drastic weight loss from 350 to 580 °C. Comparing these observations with the phase changes seen earlier in XRD, one can conclude that the gradual weight loss below 325 °C is associated with a loss of water and an increase in crystallinity of the RuO_2. This loss of water is consistent with what is seen in bulk RuO_2 up to a temperature of 600 °C.[51] The weight loss from 350 to 580 °C is from a loss of O_2 and thus a transition from RuO_2 to metallic Ru. The loss of CO_2 could possibly contribute to the weight loss at 350 to 580 °C, for if the Ru^{4+} is being reduced then the carbon may be oxidized. The TGA scan of bulk RuO_2 in literature shows that O_2 loss begins at a lower temperature for the

nanocomposite (*ca.* 350 °C) than for the bulk (*ca.* 1000 °C).[51] Possible reasons for this were discussed in the XRD results regarding the transition from crystalline RuO_2 to metallic Ru.

The molar composition of water in the RuO_2 nanoparticles for the 150 °C nanocomposite was calculated based on the weight of water lost from 25 to 325 °C in the TGA. A ratio of $RuO_2 \cdot 0.59H_2O$ was obtained, which as mentioned previously is close to the optimum molar ratio of water for electron and proton transport in hydrous RuO_2, which was found to be $RuO_2 \cdot 0.5H_2O$.[7,10,12,52] It is possible that RuO_2 oxidizes the carbon and causes additional loss of CO and CO_2 which overlaps with the dehydration process.[13] However, this additional loss would most likely be small and could potentially explain why our hydration number is slightly higher than those reported in literature, which were performed without carbon. The TGA results indicate that the RuO_2 nanoparticles present in the 150 °C nanocomposite are crystalline (observed in XRD), with some degree of hydration present. TGA was also performed on the 150 °C composite in air, to determine the loading of Ru. The loading was determined to be 33 %.

4.3.4 RU K-EDGE XAS

4.3.4.1 XANES

X-ray absorption was also employed to characterize the prepared nanocomposites. The XAS data can be divided into two main regions, which are X-ray absorption near-edge structure (XANES) and extended X-ray absorption fine structure (EXAFS). The Ru K-edge XANES spectra are shown in Figure 9.

Figure 9: Ru K-edge XANES spectra of the nanocomposites annealed at 25 °C (i), 100 °C (ii), 150 °C (iii), 200 °C (iv), 300 °C (v), 350 °C (vi), 400 °C (vii), 500 (viii), and 600 °C (ix).

The 25 and 100 °C spectra (i and ii) contain one broad peak in the XANES region, and closely resemble those seen in literature for heavily hydrated RuO_2 samples[10,53,54] (see Figure 2b in Ref. [10]). The XANES spectra for the 150-300 °C nanocomposites (iii-v) contain a broad peak with a trough in the middle, similar to those seen in literature for slightly hydrated and anhydrous RuO_2[10,53] (see Figure 2a,b in Ref. [10]). The 400-600 °C XANES spectra contain two resolved peaks, and are similar to that of the metallic Ru reference and those seen in literature for metallic Ru[10,53] (see Figure 2a in Ref. [10]), and finally the 350 °C spectrum (vi) looks like it has contributions from both RuO_2 and metallic Ru. These results suggest that there is a change from hydrous RuO_2 to

41

less hydrated or anhydrous RuO_2 between 100 and 150 °C, and a transition from RuO_2 to metallic Ru at *ca.* 350 °C.

4.3.4.2 COMPOSITIONAL ANALYSIS BY XANES FITTING

The 350 and 400 °C nanocomposites contain both RuO_2 and metallic Ru, and the relative amounts of each species can be determined by compositional analysis of the XANES region using WinXAS. The 300 °C sample was used as the RuO_2 reference in the fitting because it presumably represents the structure of RuO_2 which would be present in the 350 and 400 °C samples (*i.e.* the nanoparticles present never reach a perfectly crystalline RuO_2 structure). The 500 °C sample was used as the metallic Ru reference for the same reasons. The compositional fits of the nanocomposites were performed over the range of 22.08 to 22.21 keV.

Figure 10 shows the 350 and 400 °C XANES spectra (black, solid lines) and their compositional fits (red, dotted lines).
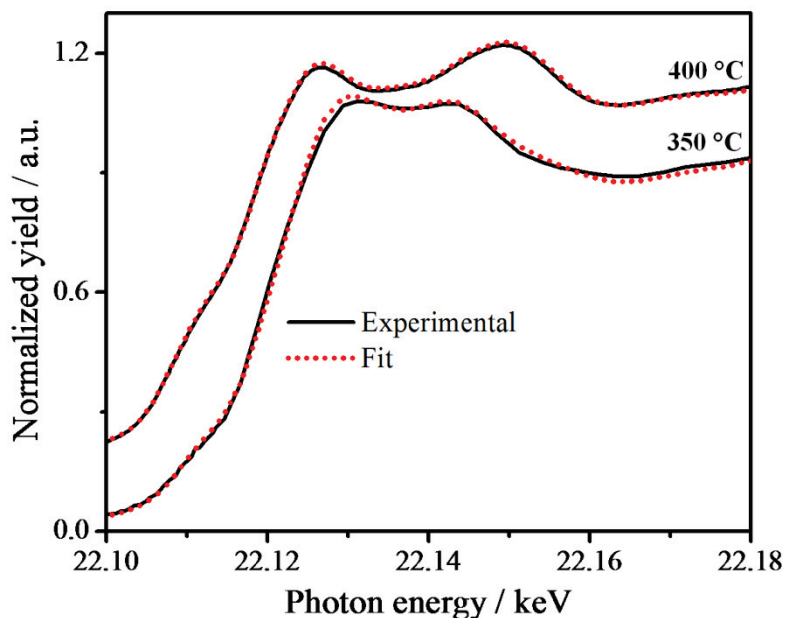
Figure 10: Compositional analysis fits of the Ru K-edge XANES region for the 350 and 400 °C samples.

The obtained results indicate that the 350 °C sample has Ru present as *ca.* 70 %

RuO_2 and 30 % metallic Ru, and the 400 °C sample has Ru present as *ca*. 20 % RuO_2 and

80 % metallic Ru. This raises the question as to whether there is one type of particle

present, containing on average these ratios of RuO_2 to metallic Ru, or whether there are

two types of particles present, one which is RuO_2 and one which is metallic Ru. The

former case is supported in the Ru L-edge results below. Also, compositional values

correlate well with the observed contributions in the R-space spectra for these samples

below. It is should be noted that this is not a discussion of the ratio of Ru to carbon in the

sample, but the ratio of RuO_2 to metallic Ru in the nanoparticles.

4.3.4.3 EXAFS

The EXAFS regions for the samples were converted to k-space over the range of

2.0 to 13.5 $Å^{-1}$. Figure 11a shows the offset k-spaces [with a $(\chi)k*k^2$ weighting] of the

nanocomposites. The intensity of the spectra for the 400 to 600 °C samples have been

multiplied by 0.5 to more easily compare their features with the other spectra. To more

easily see the difference in oscillation intensity, a plot of overlain 400 to 600 °C spectra
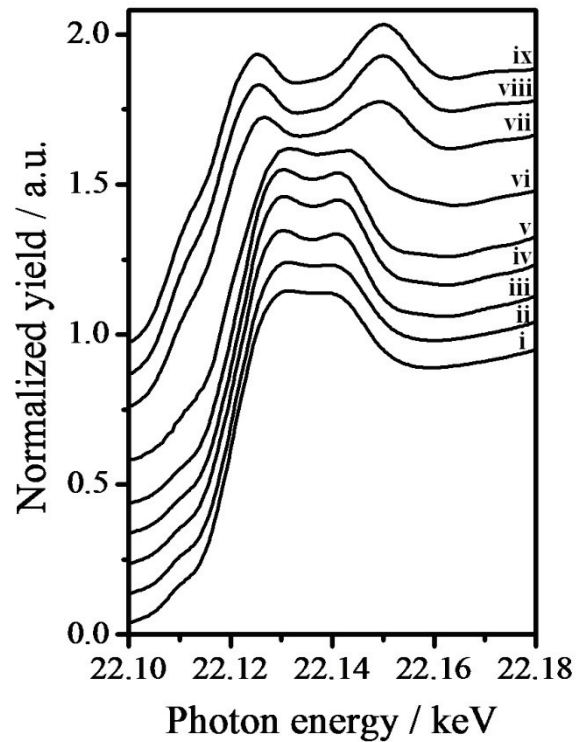
from 7.5 to 11.5 $Å^{-1}$ is shown in Figure 11b.
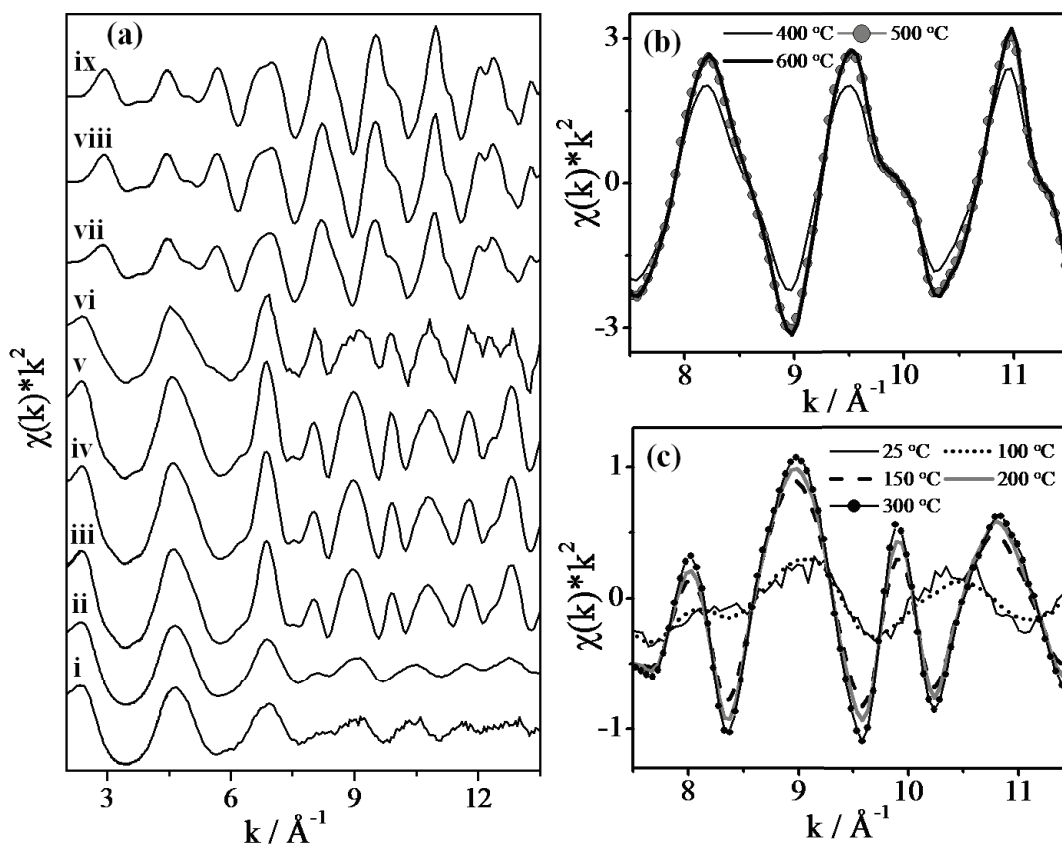
Figure 11: a) k-space spectra of the nanocomposites annealed at 25 °C (i), 100 °C (ii), 150 °C (iii), 200 °C (iv), 300 °C (v), 350 °C (vi), 400 °C (vii), 500 (viii), and 600 °C (ix). A narrow k range and overlain spectra shows subtle differences between b) 400-600 °C and c) 25-300 °C nanocomposites.

As the annealing temperature increases from 400 to 500 °C, there is a clear increase in oscillation intensity. However, the difference between 500 and 600 °C intensity is slight. Figure 11c contains the overlain 25 to 300 °C k-space spectra over a range of 7.5 to 11.5 Å^{-1}. The large difference in oscillation intensity as the temperature increases from 100 to 150 °C is observed in this plot. The nanocomposite annealed at 350 °C was not included in Figures 11b,c because, as shown in the R-space spectra in Figure 12, the nanoparticles present contain both RuO_2 and metallic Ru and thus does not fit with the trends displayed in either plot.

The k-space data were Fourier transformed (FT) over the range of 3-12 $Å^{-1}$, and

the offset $FT[\chi(k)*k^2]$ for each annealing temperature are shown in Figure 12a. Again, the

intensity of the 400 to 600 °C spectra have been multiplied by 0.5 to more easily compare

with the others.
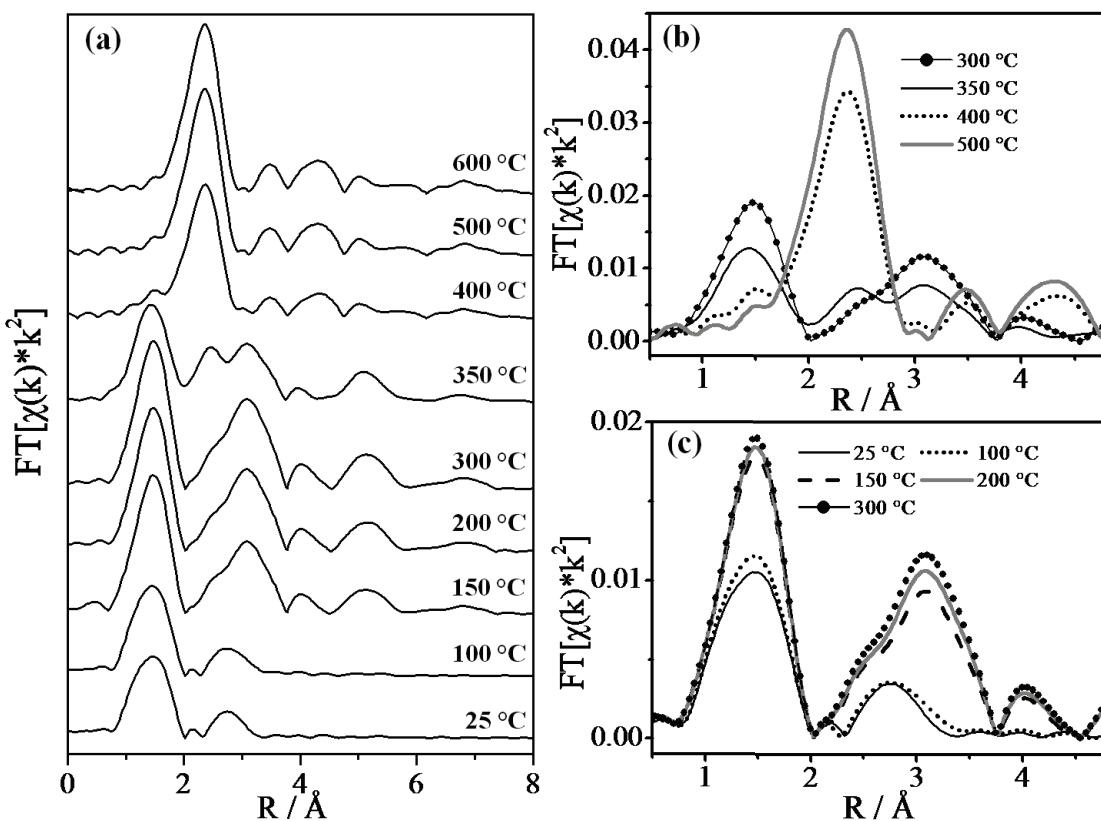
Figure 12: a) R-space spectra of all nanocomposites. b) R-space spectra for the 300, 350, 400, and 500 °C nanocomposites to show the transition from RuO$_2$ to metallic Ru. c) Overlain R-space spectra for the 25 to 300 °C nanocomposites.

As with the XANES spectra, the 25 and 100 °C spectra are similar to those seen

in literature for heavily hydrated RuO$_2$, while the spectra for the 150-300 °C are more

similar to those for only slightly hydrated samples[10,54-56] (see Figures 4,5 in Ref. [10]). A

short k range used for the FT results in poorer resolution of the Ru-Ru peaks (located at

3.11 and 3.54 Å) in the R-space than a longer k range would, which can explain

discrepancies between the R-space spectra seen here and seen in literature. Although most of the spectra collected allow for a longer k range to be used for the FT, the lowest quality spectra, 350 °C, is noisy above $k = 12$ Å^{-1} and thus all spectra were presented with this range for consistency.

The R-space spectra for the 400 to 600 °C nanocomposites are similar to those seen in literature for metallic Ru,[53,55,56] and the 350 °C spectra appears to have contributions from both RuO_2 and metallic Ru. Figure 12a confirms that, as seen in XRD and TGA, the nanoparticles present in the nanocomposites transition from heavily hydrated (amorphous) to slightly hydrated RuO_2 at *ca.* 100-150 °C, and from RuO_2 to metallic Ru at *ca.* 300-400 °C.

Figure 12b shows overlain 300 °C, 350 °C, 400 °C, and 500 °C R-space spectra. The peaks resulting from RuO_2 are less intense in the 350 °C spectrum than the 300 °C spectrum, and there is an increased intensity in the area of the metallic Ru peak (at 2.68 Å). These observations suggest that the 350 °C nanocomposite contains nanoparticles which are predominantly RuO_2, with a small amount of metallic Ru present. The 400 °C spectrum has a less intense metallic Ru peak than the 500 °C spectrum, but it has an increased intensity at 1.96 and 3.54 Å where the RuO_2 peaks should be located. This suggests the 400 °C nanocomposite contains nanoparticles that are predominantly metallic Ru with a small amount of RuO_2, as observed with XRD. The 600 °C spectrum was not included in this plot as it is essentially identical to the 500 °C spectrum, as suggested by the similarities in the k-space (Figure 11b).

Figure 12c is a plot of the overlain 25 to 300 °C R-space spectra. As the annealing temperature increases from 25 to 100 °C, there is a slight increase in intensity of the Ru-

O peak at 1.96 Å, indicating that the octahedral Ru-O shell becomes more ordered. As well, there is a slight increase in intensity at *ca.* 3.54 Å, which will be discussed in the R-space fitting results. The 25 and 100 °C spectra also have an increased intensity at 2.2 Å, relative to the other three spectra in this plot, which has been attributed to Ru-OH$_2$ or Ru-OH bonds in heavily hydrated RuO$_2$.[10,54] Also seen in Figure 12c is that as the annealing temperature is increased from 150 to 300 °C, the intensities of the peaks increase slightly, indicating that the structure of the RuO$_2$ becomes more ordered, as expected with an increased annealing temperature.

The fits of all of the R-space spectra are shown in Figure 13, excluding the 350 °C sample. A fit was not obtained for this sample because it clearly has significant contributions from both the RuO$_2$ and metallic Ru, and thus obtained fitting values would not be reliable.
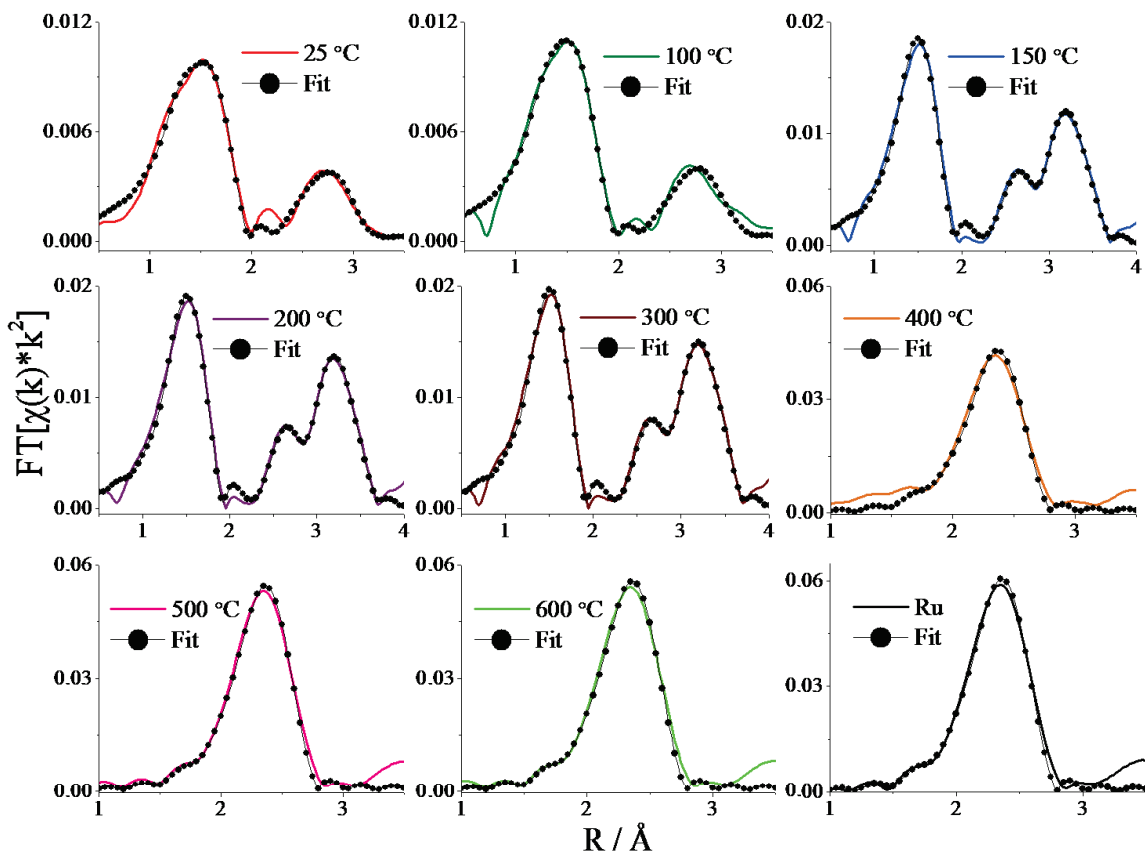
Figure 13: R-space spectra fits for all nanocomposites, excluding the 350 °C nanocomposite. The coloured, solid lines are experimental spectra and the line with black circles are the fits. All spectra were fit from 1Å≤R≤4Å.

For the fits, the nanocomposites were divided into those containing RuO_2 nanoparticles (25-300 °C) and those containing metallic Ru nanoparticles (400-600 °C). The R-space spectra shown in Figure 13 have more resolved peaks than those shown previously because a FT range of 3-14 $Å^{-1}$ was used (rather than 3-12 $Å^{-1}$), which was possible because the 350 °C sample was not included. It should be pointed out that although the peaks are more resolved, the obtained values for coordination number and bond distance will be the same as if a shorter FT range were used.

For the set of data containing RuO_2 nanoparticles , the highest quality spectrum (300 °C) was fit first to obtain values for the amplitude scaling factor (S_0^2), energy

48

threshold (E_0), coordination number (N), bond distance (R), and Debye-Waller factor (σ^2). Then the other spectra in the set (25-200 °C) were fit by varying N, R, and σ^2 while fixing the S_0^2 and E_0 to the values obtained for the 300 °C spectrum, and these results are presented in Table 2. Each of the spectra in this set was fit over the range of 1.15-3.60 Å. The S_0^2 obtained was 0.89, and the E_0 (Ru-O) and E_0 (Ru-Ru) were -5.3 and -5.0 eV, respectively. For the metal oxide refinements, once the optimum fit was obtained, one parameter (either R, N, or σ^2 for a specific shell) was changed until the χ^2 value of the refinement doubled.[57] The difference between the value obtained during the fitting and the value at which the χ^2 doubled is the presented uncertainty.

Table 2: R-space fitting results for the nanocomposites containing RuO$_2$.*

Nanocomposite	Shell	R / Å	N / atoms	σ^2 / Å^2
25 °C	Ru-O	1.98±0.02	6.0±1.1	0.010±0.003
	Ru-Ru	3.12±0.05	1.7±0.8	0.006±0.003
100 °C	Ru-O	1.98±0.02	6.4±0.9	0.009±0.002
	Ru-Ru	3.11±0.04	1.6±0.7	0.005±0.004
	Ru-Ru	3.57±0.10	0.8±1.0	0.006±0.004
150 °C	Ru-O	1.97±0.02	6.2±0.9	0.004±0.002
	Ru-Ru	3.12±0.03	1.6±0.7	0.003±0.002
	Ru-Ru	3.56±0.02	4.4±1.0	0.003±0.002
200 °C	Ru-O	1.98±0.02	6.1±0.9	0.004±0.002
	Ru-Ru	3.13±0.03	1.7±0.7	0.003±0.001
	Ru-Ru	3.56±0.02	4.8±1.0	0.003±0.001
300 °C	Ru-O	1.98±0.02	6.2±1.0	0.004±0.002
	Ru-Ru	3.13±0.03	1.8±0.8	0.002±0.001
	Ru-Ru	3.56±0.02	5.0±1.0	0.002±0.001

*The highest quality fit was obtained with S_0^2 = 0.89, E_0 (Ru-O) = -5.3 eV and E_0 (Ru-Ru) = -5.0 eV.

According to standard EXAFS analysis, the maximum number of independent variables (N_{max}) in a refinement is defined by $2\Delta k\Delta R/\pi$,[58] where Δk and ΔR are the k and R ranges, respectively. This produces N_{max}=17 for the RuO$_2$ refinements, well above the number of independent variables (N_{ind}) of 8 used in these refinements. Also, the resolution in the R-space, δR can be estimated by $\pi/2\Delta k$,[59] which yields δR=0.14 Å for these refinements. The Ru-O bonds at 1.94 and 1.98 Å in the theoretical structure are thus 0.04 Å apart and are too close to be resolved from one another. Therefore, the Ru-O peak was fit with one shell.

The fitting results of the Ru-O shell indicate that regardless of the degree of hydration, the Ru maintains a N of *ca.* 6 to surrounding oxygen atoms. However, with the samples annealed at 25 and 100 °C the Ru-O peak is clearly less intense, suggesting that the high degree of hydration causes a distorted octahedral geometry.[10]

The first Ru-Ru shell is present in all of the RuO$_2$ samples, regardless of the degree of hydration, and is positioned at *ca.* 3.12 Å. This distance, as mentioned previously, is the length of the c-axis in the anhydrous RuO$_2$ unit cell, and corresponds to a theoretical N of 2. For the nanocomposite annealed at 25 °C, the first Ru-Ru shell has a N of 1.8 and there is no second Ru-Ru shell contribution, suggesting that this nanocomposite contains heavily hydrated RuO$_2$ nanoparticles, which have a structure of chains of disordered RuO$_6$ octrahedra connected along the c-axis of the unit cell, as described in literature.[10,54] The 100 °C nanocomposite has a similar local structure of the RuO$_2$ nanoparticles as the 25 °C based on the fitting results. However, there is also a contribution from the second Ru-Ru shell, located at 3.58 Å. This distance is attributed to the bond between Ru atoms at the center of the RuO$_2$ unit cell and Ru atoms at the corner

the unit cell. Therefore, it is suggested that this sample also contains minor bridging between the disordered RuO_6 chains. The uncertainty in R of the second Ru-Ru shell in the 100 °C composite is larger than the other peaks because of the low peak intensity of this peak.

For the 150 °C nanocomposite, the second Ru-Ru shell N increases to 4.4, indicating that the structure of the RuO_2 nanoparticles has become more crystalline and ordered. As the annealing temperature then approaches 300 °C, the Ns approach the theoretical values of 2 and 8 for the first and second Ru-Ru shell, respectively, suggesting that the structure of the RuO_2 is similar to the anhydrous, rutile RuO_2. Also, σ^2 decreases with an increase in annealing temperature, which is indicative of more order in the structure of the absorbing atom, Ru. However, because the Ru-Ru Ns never reach the theoretical values, it suggests that there is some degree of hydration present in the RuO_2 nanoparticles, which was proven earlier with TGA.

The R-space spectra for nanocomposites containing metallic Ru nanoparticles (400-600 °C) were fit using a similar process as above. The metallic Ru reference was fit first (labeled Ru in Figure 13) and the N and R were fixed at the theoretical values to obtain S_0^2 and E_0, which were then used for fitting the 400 to 600 °C spectra. An S_0^2 of 0.86 and E_0 of -5.3 eV were used for the fits, and all spectra in this set were fit over the range of 1.85-2.70 Å, with the results presented in Table 3.

Table 3: R-space fitting results for the nanocomposites containing metallic Ru.*

Nanocomposite	Shell	R / Å	N / atoms	σ^2 / Å^2
400 °C	Ru-Ru	2.68±0.01	9.7±0.9	0.0044±0.0005
500 °C	Ru-Ru	2.68±0.01	11.4±0.9	0.0040±0.0004
600 °C	Ru-Ru	2.68±0.01	11.2±0.9	0.0038±0.0004

*The highest quality fit was obtained with $S_0^2 = 0.86$ and E_0 (Ru-Ru) = -5.3 eV.

For the metallic Ru refinements, the uncertainties were determined using a similar method as to that of the metal oxide refinements, except the residual of the optimum fit was doubled to obtain the uncertainties, rather than the χ^2. This method is used in the literature for metallic Au.[60] The N_{max} for the metallic Ru fits was 6, which is higher than the N_{ind} of 3 used in the refinements. The 400 °C nanocomposite has a N of only 9.7, which is smaller than a value close to 12 which would be expected for a particle 10 nm in diameter (as determined by XRD). This inconsistency is due to an increased intensity where the RuO_2 peaks are located, as discussed previously. In effect, because there is still RuO_2 present in this sample it makes the peak from metallic Ru decreased in intensity. The Ns for the 500 and 600 °C samples, 11.4 and 11.2 respectively, are approaching the theoretical value of 12 for bulk metallic Ru as expected for such large particles. The uncertainty associated with the Ns is 0.9 and thus the difference between the latter two values can be considered negligible. Also, as with the RuO_2 nanocomposites, σ^2 decreases with an increasing annealing temperature, indicating more order in the structure of the metallic Ru nanoparticles.

4.3.5 Ru L$_3$-edge XAS

Ru L$_3$-edge data were collected on the 350 and 400 °C nanocomposites to gather more information on the transition from metal oxide to metal. The TEY has a probing

depth on the nanometer scale while FLY has a probing depth on the micrometer scale, making TEY surface sensitive and FLY bulk sensitive.[40,61] Figure 14 shows the TEY (red, dotted line) and FLY (black, solid line) for both samples. First, the differences between the two nanocomposites will be discussed, followed by the differences between TEY and FLY within each nanocomposite.
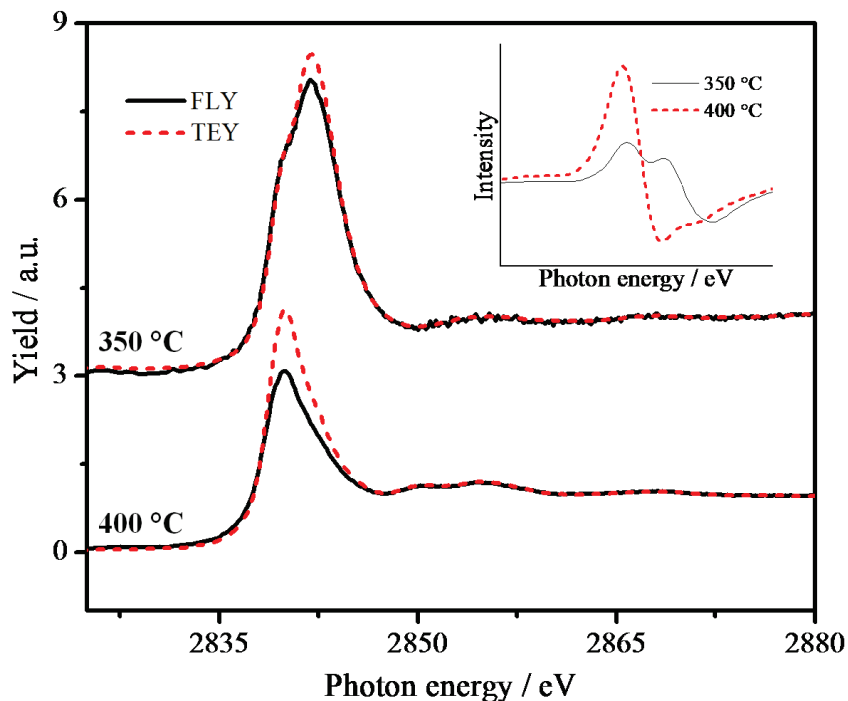
Figure 14: Ru L_3-edge fluorescence yield (FLY) and total electron yield (TEY) for the 350 and 400 °C nanocomposites. The inset shows the first derivative for the 350 and 400 °C TEY spectra.

The whiteline at ~2840 eV, which arises from Ru $2p_{3/2}$ to $3d_{5/2,3/2}$ transition, is more intense for the 350 °C than the 400 °C nanocomposite in both TEY and FLY. This indicates that there is more unoccupied d density of states (dDOS) in the 350 °C nanocomposite,[48] which confirms that this nanocomposite contains nanoparticles which are mostly RuO_2 (Ru^{4+}) while 400 °C contains nanoparticles which are mostly metallic Ru [Ru(0)]. Also, the 350 °C whiteline is located at 2842 eV while the 400 °C whiteline

is at 2840 eV. A shift to higher binding energy is expected if the 350 °C nanocomposite nanoparticles are mostly metal oxide and the 400 °C are mostly metallic.

The 350 °C spectrum has an obvious pre-edge feature that is not present in the 400 °C spectrum. The Figure 14 inset is a plot of the first derivatives of the TEY for each sample, and it is clear that the 350 °C whiteline is a doublet while the 400 °C whiteline is only a singlet. Upon first glance, it appears as though the pre-edge may be due to contributions from metallic Ru, as it occurs at a similar energy to the 400 °C whiteline. To determine the origin of the features in each whiteline, theoretical L_3-edge data were calculated for both RuO_2 and metallic Ru.
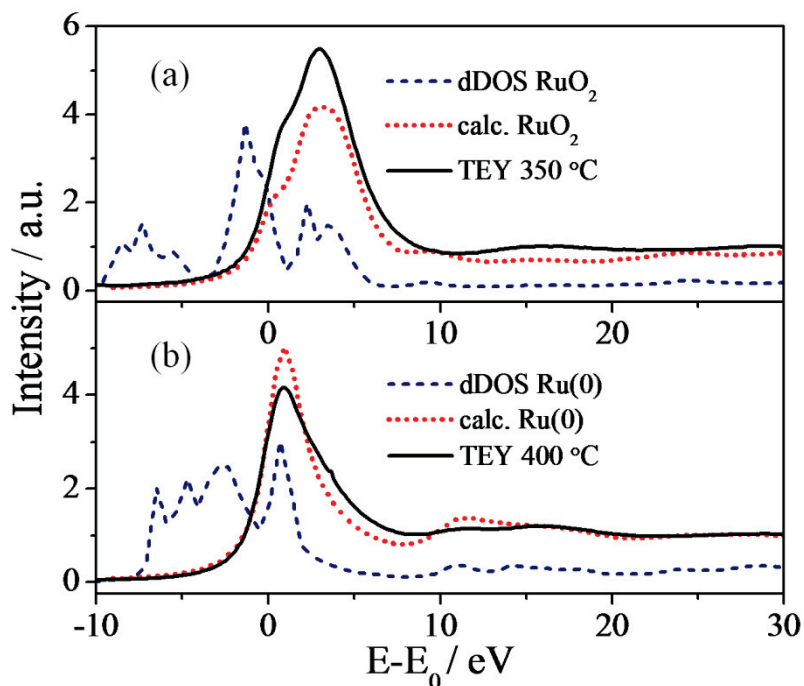
Figure 15: Ru L_3-edge spectra of a) calculated RuO_2 dDOS, calculated RuO_2 XANES and 350°C TEY and b) calculated metallic Ru dDOS, calculated metallic Ru XANES and 400 °C TEY.

Figure 15a contains the RuO_2 dDOS, the calculated RuO_2 XANES spectrum, and the 350 °C TEY, and Figure 15b contains the analogous plot for metallic Ru with the 400

°C TEY. The whiteline peak shape is similar for the 350 °C spectrum and the calculated RuO_2 XANES, as well as for the 400 °C sample and the calculated Ru(0) XANES, confirming again that these are the main species present in each respective sample.

The pre-edge feature in the 350 °C spectrum is present in the calculated RuO_2 spectrum as well, proving that it is not solely due to contributions from metallic Ru. The dDOS shows that above the Fermi level ($E-E_0 = 0$ eV), RuO_2 has two areas in the band structure, indicating there are two electronic transitions possible, which give rise to the pre-edge feature and main peak. The exact transitions which occur in the RuO_2 L_3-edge have been investigated in literature, with the pre-edge and main peak being due to $2p \rightarrow t_{2g}$ and $2p \rightarrow e_g$ transitions, respectively.[62] The energy difference between the two transitions (*i.e.* the splitting) can also give relevant structural information. A splitting of 2.10 eV was observed for the TEY spectrum of the 350 °C composite, which is smaller than that observed for a rutile RuO_2 microcrystal (2.65 eV) in literature.[48] This decrease in splitting could be attributed to the presence of $RuO_2 \cdot xH_2O$ and/or the Ru-O-C interaction.[48]

The 400 °C and calculated Ru(0) spectra contain single peaks, and it can be seen in the dDOS for Ru(0) that there is only one area in the band structure above the Fermi level, indicating there is only one type of electronic transition possible.

As mentioned previously, the intensity of the whiteline is proportional to the dDOS, with an increased intensity indicating RuO_2 is present rather than metallic Ru. In Figure 14, the TEY is more intense than the FLY for both samples. Because TEY is more surface sensitive, this indicates that there must be more oxide present on the surface of the nanoparticles than in the core. Therefore, it is proposed that the transition from metal oxide to metal follows a process similar to Scheme 3.

Scheme 3: Proposed transition of the RuO$_2$ nanoparticles present at 300 °C to metallic Ru nanoparticles present at 500 °C.
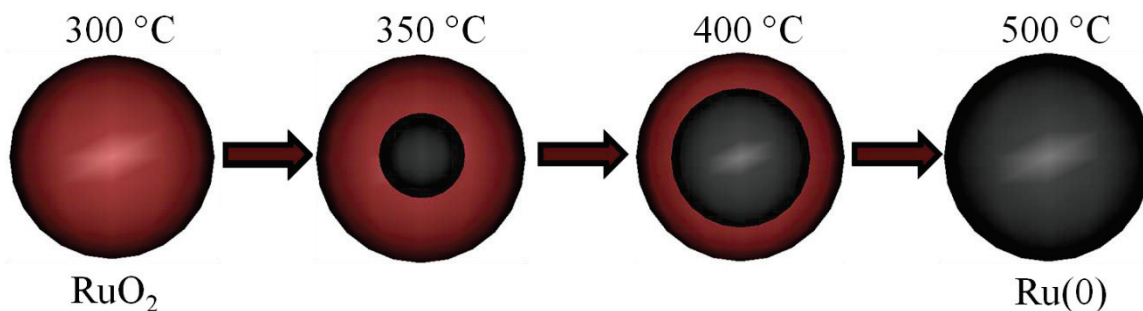
Annealing at 300 °C forms nanoparticles containing only RuO$_2$, and increasing to 350 °C forms nanoparticles which are mostly metal oxide with a metallic core. Annealing at 400 °C forms nanoparticles which are mostly metallic with an oxide-rich surface, and finally annealing at 500 °C forms pure metallic Ru nanoparticles in the nanocomposite.

4.3.6 CYCLIC VOLTAMMETRY

Cyclic voltammetry experiments were performed on the 150 °C and blank carbon samples. Figure 16 shows a cyclic voltammogram of the two samples from 0.4 to 1.1 V vs. SHE, run at 10 mV s^{-1}. Shown in the inset is a cyclic voltammogram of the samples from 0.0 to 1.0 V at 50 mV s^{-1}, showing the large cathodic current at potentials negative of 0.4 V discussed earlier. To avoid this region, the lowest potential of the cyclic voltammograms was increased to 0.4 V.
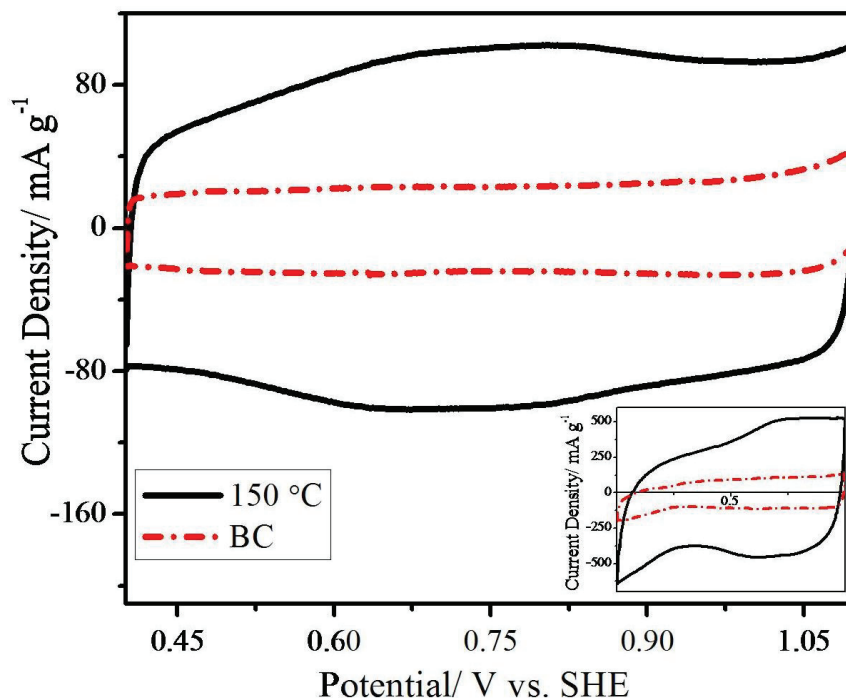
Figure 16: Cyclic voltammogram of 150 °C and blank carbon (labeled BC) samples from 0.4 to 1.1 V vs. SHE at 10 mV s^{-1}, and (*inset*) cyclic voltammogram of 150 °C and blank carbon samples from 0.0 to 1.0 V at 50 mV s^{-1}.

The capacitance of the 150 °C and blank carbon samples was calculated from the cyclic voltammogram at 0.75 V using Equation 14. From this, the 150 °C nanocomposite capacitance was found to be 10.2 F g^{-1} and the blank carbon sample capacitance was 2.3 F g^{-1}. From the loading of RuO$_2$ (33 %), the specific capacitance of the RuO$_2$ component was found to be 24 F g^{-1}. Theoretically for RuO$_2$·0.5H$_2$O the capacitance should be *ca.* 680 F/g per electron,[13] which means that only about 4 % of the RuO$_2$ in the 150 °C composite is being used to store charge, assuming the RuO$_2$ present has the maximum theoretical capacitance, and that only one electron is stored per Ru site. The latter assumption has been supported by *in situ* studies at the Ru L-edge of RuO$_2$ in the literature.[63] This indicates that the triple impregnation synthesis used in this work creates RuO$_2$ which is not accessible by the electrolyte. Perhaps the second inpregnation forms

RuO$_2$ which does not have good electrical contact with that deposited by the first impregnation, and therefore blocks the first RuO$_2$ from the electrolyte, and similarly the third may block the second impregnation. Also, the RuO$_2$ present in the composite may be accessible by the electrolyte, but it may have poor electrical contact with the carbon. A decrease in the specific capacitance of the RuO$_2$ component with high loadings in composites has been observed in the literature due to poor electrical between the carbon and the RuO$_2$.[13] The fact that the specific capacitance of our RuO$_2$ component is so small suggests that is likely a result of a combination of factors.

4.3.7 IN SITU ELECTROCHEMICAL-XAS

Preliminary *in situ* electrochemical-XAS experiments at the Ru K-edge were employed to observe changes in the XANES region with changes in potential. The electrochemical cell containing the working electrode was placed in the X-ray beam path, and XAS spectra were recorded while holding the potential of the working electrode at different values. The development of the experimental setup for the *in situ* studies is described in detail in Chapter 6. Figure 17 shows the XANES spectra collected *in situ* for the 150 °C nanocomposite (labeled Nano) and bulk RuO$_2$·xH$_2$O (labeled Bulk).
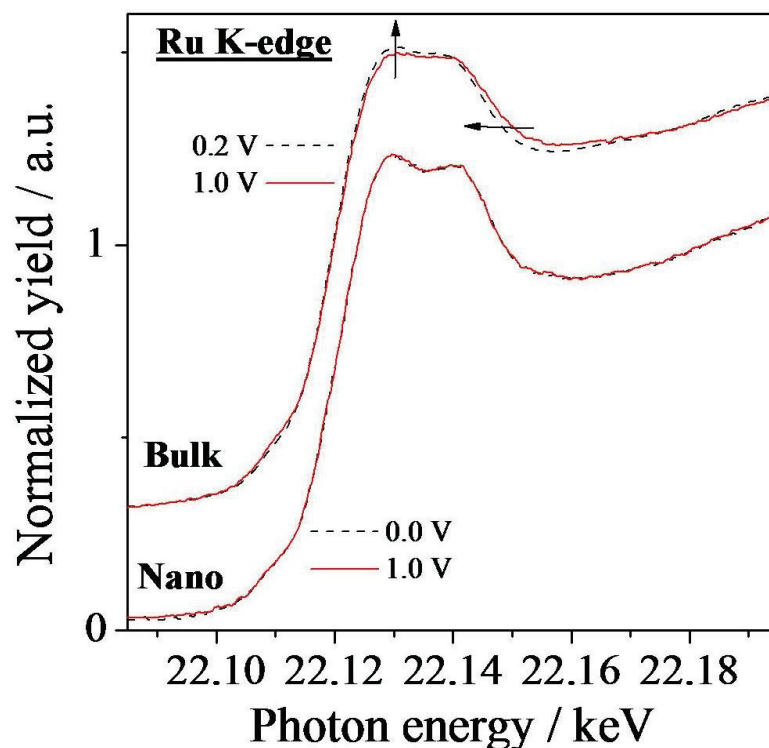
Figure 17: Ru K-edge XANES for the 150 °C nanocomposite (labeled Nano) at 0.0 V and 1.0 V and the bulk RuO$_2$·xH$_2$O (labeled Bulk) at 0.2 V and 1.0 V, collected *in situ*.

The spectra for the nanocomposite sample at 0.0 V and 1.0 V are essentially identical, suggesting that there is no change in the structure of the RuO$_2$ with a change in potential. However, there are notable differences between the spectra for the bulk sample at 0.2 V and 1.0 V. The 0.2 V spectrum has a steeper absorption edge than the 1.0 V spectrum, and also reaches a more intense maximum. The 0.2 V spectrum then becomes less intense than the 1.0 V beginning at *ca.* 22.1425 keV. These observations in the XANES spectra for the bulk sample are consistent with those seen in literature for an *in situ* study RuO$_2$ films electrodeposited on a Au substrate.[64]

The *in situ* results for bulk RuO$_2$·xH$_2$O indicate that Ru K-edge XAS is capable of detecting changes between the reduced and oxidized forms of RuO$_2$·xH$_2$O. The cyclic

voltammograms shown previously suggest that only about 4 % of the RuO_2 present in the 150 °C composite is being used to store charge. Therefore, when the applied potential is changed, only about 4 % of the RuO_2 will undergo an oxidation or reduction, and 96 % will remain unchanged. The K-edge XAS signal is an average of the Ru sites in the sample, and if 96 % of the sample is unchanged, then there should be essentially no difference between the 0.0 V and 1.0 V XANES spectra, which was observed in the *in situ* results. These results are further indication that the synthesis employed formed RuO_2 which is not electroactive and perhaps can not be accessed by the electrolyte, or has poor electrical contact with the carbon.

4.4 CONCLUSIONS

The effect of annealing temperature on the structure of RuO_2 nanoparticles in a RuO_2/carbon nanocomposite was thoroughly investigated using XRD, TGA, TEM, EXAFS, XANES, *ab initio* calculations, cyclic voltammetry and *in situ* electrochemical-XAS. The RuO_2 transitions from a heavily hydrated to slightly hydrated form at *ca.* 100-150 °C, and is further reduced to metallic Ru at *ca.* 350 °C. The latter phase transition occurs at lower temperatures than for bulk RuO_2. RuO_2 nanoparticles (150 to 300 °C nanocomposites) have a higher structural stability with respect to temperature than metallic Ru nanoparticles (400 to 600 °C nanocomposites), possibly due to the presence of Ru-O-C bonds which can stabilize RuO_2 nanoparticles.[48] Ru L_3-edge data showed that the phase transition from RuO_2 to metallic Ru occurs via an inside-out process, with the center of the RuO_2 particle becoming metallic and the surface remaining as crystalline metal oxide.

The specific capacitance of the RuO_2 component in the 150 °C nanocomposite was only 24 F g^{-1}, suggesting that only a small amount of the RuO_2 present is electroactive. This was supported by *in situ* electrochemical-XAS studies, in which no change in the Ru K-edge XANES was observed when the applied potential to the 150 °C composite electrode was changed. The *in situ* studies were able to detect a difference between the reduced and oxidized forms of a bulk $RuO_2·xH_2O$ sample.

CHAPTER 5: DETERMINING THE DEPOSITION LOCATION OF RuO_2 IN THE 150 °C RuO_2/CARBON COMPOSITE

5.1 SEM AND EDS

In Chapter 4, the synthesis and characterization of a RuO_2/carbon composite annealed at 150 °C was described. Additional characterization was performed on this composite, in hopes of gaining information on the effect of the synthesis on the structure of the mesoporous carbon powder, and where the RuO_2 deposited on the carbon. The SEM images presented in Figure 18 are the low resolution images of the 150 °C composite (a) and the untreated mesoporous carbon powder (b). It should be noted that the untreated powder is not the blank carbon powder discussed in the synthesis.
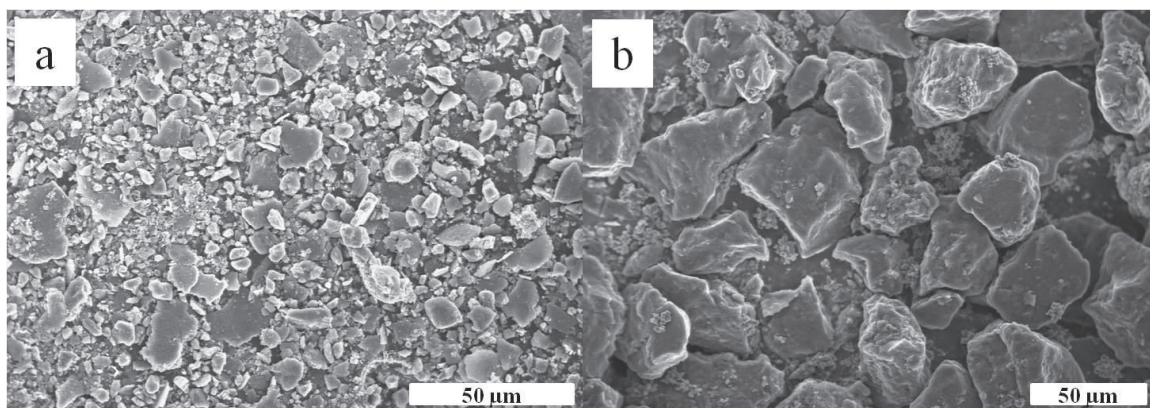
Figure 18: Low magnification SEM images of a) the 150 °C composite and b) untreated mesoporous carbon powder.

The scale bars at the bottom right of the images are not the same. However, the carbon particles are noticeably smaller in the 150 °C composite than in the untreated powder. The largest particles in the 150 °C composite are *ca.* 15-20 µm, with many smaller, while the untreated powder has particles of *ca.* 30-50 µm, and are more uniform in size. It has been found in literature that both sonicating[65] and stirring[66] carbon can

cause degradation, and it is likely that both used in this synthesis fragmented the particles.

Higher magnification images were also taken, shown in Figure 19, with the 150 °C composite in (a) and the untreated mesoporous carbon powder in (b).
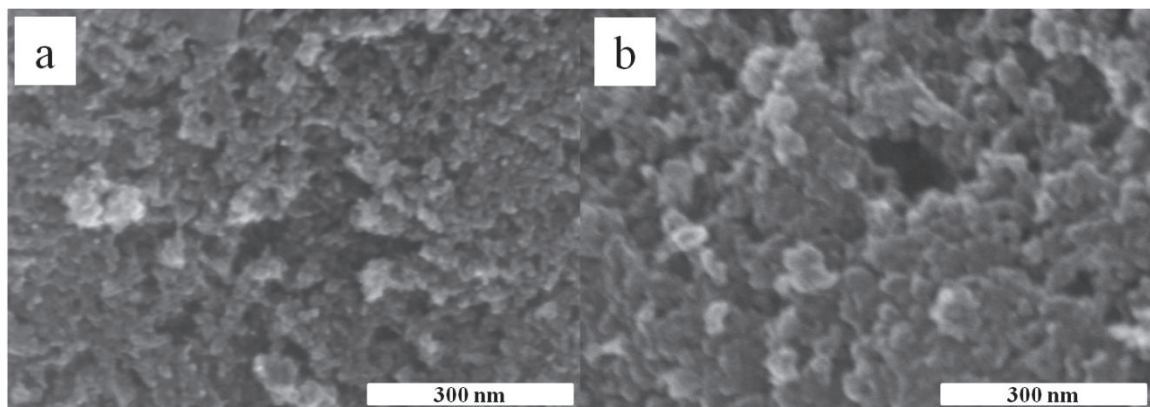
Figure 19: High magnification SEM images of a) 150 °C composite and b) untreated mesoporous carbon powder.

The surface morphologies of the two samples are rough and porous, and are similar to one another. In a literature study, there was also no obvious difference observed for an activated carbon, before and after loading with RuO_2.[15] It is possible that the sonication step in our synthesis removes the RuO_2 from the surface of the carbon, leaving RuO_2 only in the pores. However, RuO_2 remained attached to graphene sheets after a sonication step in a literature study[49], which may suggest that RuO_2 should remain on the surface of our carbon after sonication as well. Little information could be gained on the RuO_2 present in the 150 °C composite. However, it can be hypothesized that the RuO_2 is in the pores of the carbon because there is no difference in the surface morphology.

Energy dispersive spectroscopy (EDS) was used to perform an elemental analysis on the two samples imaged above. Table 4 summarizes the values obtained from the EDS analysis.

Table 4: Elemental analysis values from EDS.

Element	Untreated Mesoporous Carbon		150 °C Composite	
	Weight %	Atomic %	Weight %	Atomic %
C	96.0	96.9	60.3	82.8
O	4.0	3.1	11.0	11.4
F	---	---	1.2	1.0
Na	---	---	0.6	0.5
Ru	---	---	26.9	4.4

All of the elements were probed at their K-edge except for Ru, for which L-edge fluorescence was detected. Multiple measurements were not performed so errors were not determined for the values. For the untreated powder, these results indicate that there exists some sort of oxygen species on the surface of the carbon. This oxygen could be from carbon surface functionalities, which would support the Ru-O-C interactions discussed previously. The 150 °C composite is about 27 % Ru by mass according to the EDS, which is close to the loading of 33 % obtained by TGA. Also, although the carbon weight % decreases from the untreated sample to the composite, the oxygen weight % increases, which is expected as a metal oxide was formed in the composite. Lastly, there are additional minor contributions from sodium and fluorine in the composite. The sodium is most likely from the $NaHCO_3$ used in the synthesis. However the origin of the fluorine is unknown.

5.2 BET

It was originally assumed that the RuO_2 deposited on the carbon in the 150 °C composite was almost exclusively in the pores of the carbon. This was supported by the fact that little change in the surface morphology was observed in the SEM images, and that the particle size range from TEM analysis showed an average size of 11 nm, or 110 Å, and the pore size in the carbon is 100 Å, as indicated by the manufacturer. The size of RuO_2 formed in the absence of carbon was *ca*. 10 nm as well, indicating that the RuO_2 is not being constrained by the size of the pores. It could, however, be filling the pores. To test this hypothesis, BET measurements were collected on the 150 °C composite and the blank carbon sample which was treated like the 150 °C composite in the absence of $RuCl_3 \cdot xH_2O$.

BET single point measurements were performed first, and the blank carbon sample was found to have a surface area (SA) of 208 ± 1 m^2 g^{-1}, while the 150 °C composite had a SA of 153 ± 2 m^2 g^{-1}. The decrease in SA from the blank carbon to the loaded carbon is consistent with the loaded RuO_2 being contained within the pores of the mesoporous carbon powder, and thus the adsorbing gas, N_2, can no longer access the pores. The decrease in SA could also be due to RuO_2 blocking the pores, which is supported by the low capacitance of the RuO_2 component discussed in Chapter 4. Finally, the fact that RuO_2 is denser than the carbon, and the SA is normalized to the weight of the material could account for the decrease in SA as well.[14]

Nitrogen adsorption isotherms give more in depth information about the pores in materials than single point surface area measurements. The isotherms are shown in Figure

20, and are similar to isotherms collected for another mesoporous carbon loaded with RuO$_2$.[16]
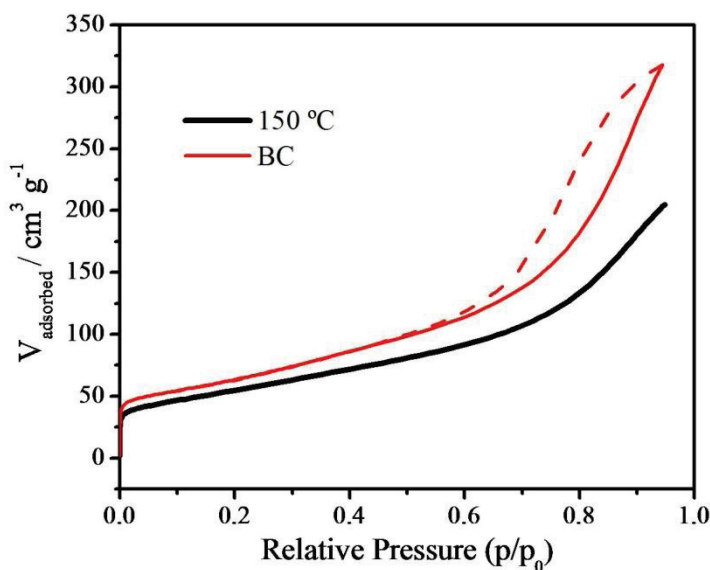
Figure 20: Nitrogen adsorption isotherms of the 150 °C composite and the blank carbon sample (labelled BC).

The shape of the isotherms and the fact that there are hysteresis loops at high pressures (only recorded for the blank carbon sample) indicate the isotherms are of type IV and both micropores and mesopores are present in the samples.[67] Also, there is a higher volume of gas adsorbed on the unloaded sample, which could again indicate that there are more pores accessible, or it could be a result of the higher mass of RuO$_2$.

The nitrogen adsorption isotherms were then converted to pore-size distributions (PSDs) shown in Figure 21. It can be seen that both samples contain micropores with a diameter of 10 Å or less and mesopores with a diameter centered at 100 Å.
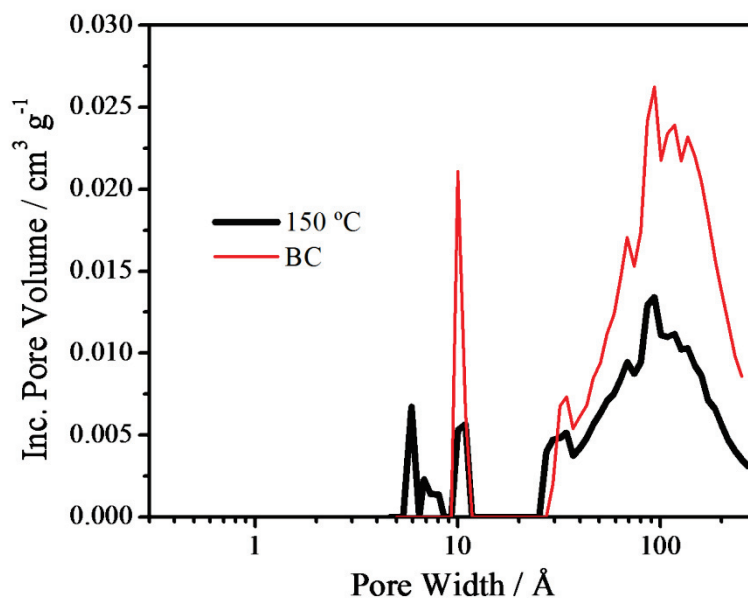
Figure 21: Pore-size distributions of the 150 °C composite and the blank carbon sample, labelled BC.

The most pronounced difference between the pore-size distributions is the decrease in pore volume of the peak centered at 100 Å (10 nm) after loading the carbon with RuO_2. The total pore volume of the blank carbon and 150 °C samples are 0.45 and 0.25 $cm^3 g^{-1}$, respectively. A similar decrease in pore volume after loading a mesoporous carbon powder with RuO_2 in the literature has been attributed to the fact that hydrous RuO_2 has a smaller surface area (SA) than the carbon in that synthesis.[16] The SA of the mesoporous carbon powder in the literature reference was 555 $m^2 g^{-1}$, and $RuO_2 \cdot xH_2O$ has been found to be close to 200 $m^2 g^{-1}$, depending on the degree of hydration.[68] However, it was shown above (pg. 63) that the surface area of the mesoporous carbon used in this synthesis is 208 $m^2 g^{-1}$, which is very similar to that of $RuO_2 \cdot xH_2O$, and therefore the difference in surface area to account for decrease in pore volume can be ruled out.

If RuO_2 is only filling the pores of the carbon, and not blocking access to them, a decrease in the overall pore size of the mesopores would be expected. This would result from partially unfilled pores having smaller diameters because of RuO_2 along the pore walls. There is a slight increase in pore volume in the 150 °C composite at *ca*. 25, 8, and 6 Å which could be a result of partially unfilled larger pores. However, the increased pore volume at 25 Å could also be due to pores in the RuO_2. In a literature study, mesopores of about 2 nm in diameter were found present in a slightly hydrated RuO_2 sample.[68] When looking at the majority of the pore volume centered at 100 Å, it does not appear that there is a decrease in pore size due to partial filling of the pores, but rather just a decreased volume of the pores present, suggesting that the RuO_2 is also blocking access to the pores. This may again correlate with the small capacitance observed for the RuO_2 component, and the fact that much of the RuO_2 is not electroactive.

There is also a decrease in the volume of micropores at 10 Å after loading the mesoporous carbon with RuO_2. The range of nanoparticle sizes in Chapter 4 indicated that there are nanoparticles as small as 4 nm in the 150 °C composite. Therefore, it is possible that there are smaller nanoparticles filling the 10 Å pores which could not be resolved in the TEM images. Also, these micropores could be branched off the mesopores and when the mesopores become filled or blocked by RuO_2, it blocks access of the N_2 to the micropores as well.

5.3 SAXS

Small angle X-ray scattering was also employed to study the blank carbon sample and the 150 °C composite, and the experimental data with fits (performed by Dr. David Stevens at the Department of Physics, Dalhousie University) are shown in Figure 22.
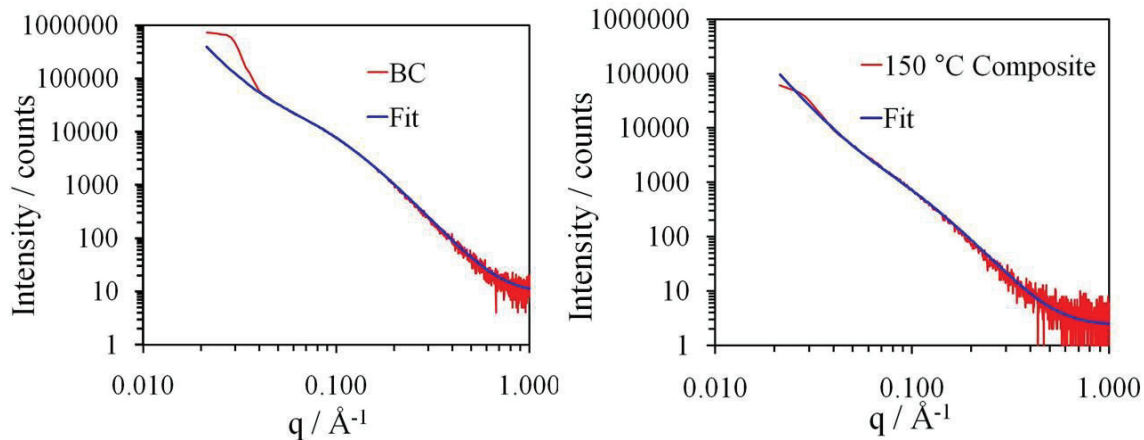
Figure 22: SAXS profiles for the blank carbon sample (labelled BC, left) and the 150 °C composites (right), and the respective fits.

The blank carbon sample has an increased scattered intensity relative to the 150 °C composite across the q range of 0.04 to 0.4 Å^{-1}, which is indicative of more nano-sized porosity in the former.[31] The scattering intensity is related to the difference in electron density between the pore and the surrounding carbon, based on the model used. The difference in electron density would be larger for a completely empty pore than for a pore which is partially filled with RuO_2. This suggests that nanopores in the blank carbon are being partially filled with RuO_2, rather than only blocked by RuO_2. If these nanopores were only being blocked by RuO_2, then the difference in electron density between the pore and surrounding material would be large, and the profile would be more similar to that of the blank carbon. It should be noted that we are discussing the nanopores in the carbon powder, not the mesopores, which are too large to be studied using this method. To obtain an estimation of the nanopore Debye correlation lengths and their contributions to the scattering profile, both experimental data sets were fit using the model equation described in Chapter 2.4, and the optimized fit parameters obtained are shown in Table 5.

Table 5: Parameter values obtained from the SAXS profile fits.

Parameter	BC	150 °C Composite
A	0.10	0.10
B	1.74×10^{-6}	7.12×10^{-5}
a_1	12.2	12.2
C	0.018	0.0059
a_2	4.6	4.6
D	9.0	9.0

*The n value determined from the fit of the blank carbon sample (3.9) was used for the 150 °C composite fitting.

Recall that a_1 and a_2 represent two characteristic pore dimensions, with units of Angstroms, and B and C are the contributions from pores of length a_1 and a_2, respectively. A and D are the bulk scattering and constant background contributions. The small values for the parameter B suggest that there is little to no contribution from larger nanopores with a correlation length of *ca.* 12 Å. The contribution from the smaller pores of correlation length 4.6 Å, C, decreases when the blank mesoporous carbon sample is loaded with RuO_2. This suggests that there is less difference in electron density between the pore and surrounding material after loading, and therefore the nanopores might be partially filled with RuO_2 rather than only blocked. The SAXS measurements and fits in this particular case are useful in determining whether nanopores are present in a sample and the relative contributions of nanopores. However, the model used to describe the system is simple and does not allow for exact pore or particle size determination, and should only serve as an aid to other experimental findings. In general, however, under different conditions and models, SAXS can be used to determine exact pore sizes.

5.4 CONCLUSIONS

The analyses and techniques in this chapter were performed to gain insight into where the RuO_2 was depositing in the carbon composite. The images from SEM contained no observable differences between the surfaces of the untreated carbon and the 150 °C composite, suggesting that the RuO_2 may be in the pores of the carbon. The BET single point measurements showed a decrease in the surface area of the carbon after loading with RuO_2. However, the difference in surface area could be a result of the higher mass of RuO_2 compared to the carbon. The BET nitrogen adsorption isotherms and pore-size distributions show a decrease in the pore volume of the carbon upon loading with RuO_2. However, it can not be concluded whether the RuO_2 is filling the pores or blocking access to them. The SAXS scattering profiles suggest that RuO_2 is partially filling the nanopores in the carbon, decreasing the difference in electron density between the pore and the surrounding material. Although some results indicate that the RuO_2 is filling the pores in the carbon powder, no definite conclusions can be made.

CHAPTER 6: *IN SITU* ELECTROCHEMICAL-XAS STUDIES

6.1 DESIGN OF EXPERIMENTAL SETUP

$RuO_2 \cdot xH_2O$ can display an extraordinarily high pseudocapacitance in acid electrolytes, and thus it is of interest to understand exactly how the structure of this species changes with potential.[63, 64, 69] One method to determine this is *in situ* electrochemical-XAS, in which the potential of the working electrode is held constant, and XAS measurements are performed. Performing Ru K-edge measurements was chosen for the preliminary studies, as opposed to L-edge, as the work station at HXMA beamline (CLS) is not under vacuum. The electrochemical cell chosen was a cylindrical PTFE vial (*ca.* 13 mm diameter and 53 mm height). PTFE was chosen because it is relatively transparent to X-rays around the energy range of the Ru K-edge (22117 eV), compared to other possibilities like glass. The arrangement of the counter electrode (CE), reference electrode (RE), and working electrode (WE) in the cell is demonstrated in Figure 23 (with the electrodes drawn to scale relative to the cell). The counter and reference electrodes were placed below and above the working electrode, respectively, and were also shifted horizontally relative to the working electrode, to ensure that they were not in the X-ray beam path. This was done to minimize beam attenuation through the electrochemical cell.
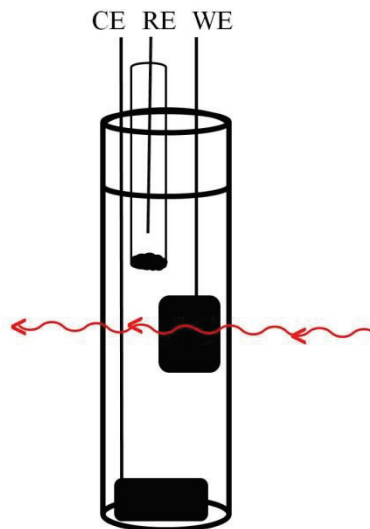
Figure 23: Electrode setup in the PTFE electrochemical cell for *in situ* studies.

The NaCl filling solution for the Ag/AgCl reference electrode was chosen over KCl because K_2SO_4 is more insoluble than Na_2SO_4 and therefore may be more likely to precipitate in the frit of the reference electrode. The cell arrangement at the beamline work station is shown in Figure 24. In the image, the X-rays would be travelling from right to left through the sample.

Figure 24: Alignment of the *in situ* electrochemical cell at the HXMA beamline (CLS).

Before any electrochemistry was performed on the desired working electrodes (RuO$_2$ and/or carbon powders) in the PTFE vial cell, the stability of the vial against acid degradation was tested by running Pt cyclic voltammograms every hour for 11 hours in 1.0 M H$_2$SO$_4$, shown in Figure A.1 of Appendix A. The shape of the cyclic voltammograms remained unchanged, indicating no additional electroactive species were formed from degradation of the PTFE vial in acid media.

The *in situ* studies were to be performed on powder samples which were mounted on a substrate prior to the experimental studies. The substrates attempted were double-sided sticky carbon tabs, carbon tape, and sticky carbon. The carbon tab and carbon tape were quite resistive (as indicated by the tilted cyclic voltammograms obtained using cyclic voltammetry), did not maintain adequate contact with the platinum wire to which they were attached, and additionally the powder did not adhere properly to these

substrates. The sticky carbon did not have any of these initial issues. However, it was observed that if N_2 was bubbled in the electrochemical cell for an extended period of time it would remove powder from the substrate, indicated by a decrease in current shown with continual cycling in Figure 25.
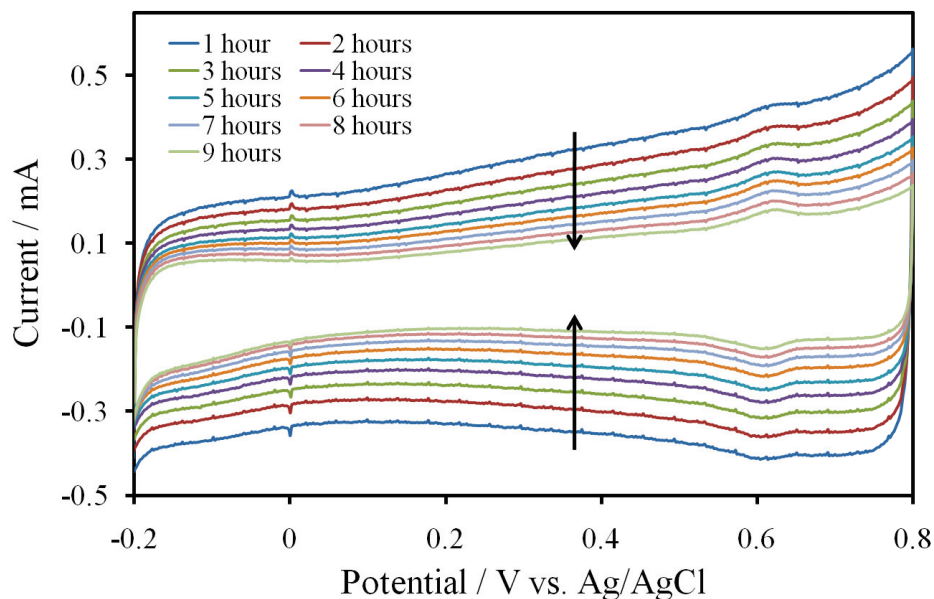

Figure 25: Cyclic voltammograms showing a decrease in current with increasing N_2 bubbling time, indicated by the arrows.

The cyclic voltammograms above were collected on the untreated mesoporous carbon powder, and the arrows indicate increasing N_2 bubbling time, starting at one hour (blue line) to nine hours (dark green line), and once every hour in between. Bubbling with N_2 for the shortest length of time is desired, and therefore the electrolyte was deaerated only briefly (*ca.* five minutes) between electrochemical studies. To test whether short bubbling durations would suffice, the electrolyte was deaerated, and then the N_2 bubbling was stopped and cyclic voltammograms were collected at after 1, 2, and 4 hours, and were compared to the initial cyclic voltammogram, shown in Figure A.2 of Appendix A. There are essentially no changes in the cyclic voltammograms after the first two hours,

and only minor changes after four hours. This indicated that continuous bubbling was not necessary, but the electrolyte should be bubbled with N_2 after two hours. This allowed sufficient time to perform an XAS scan between bubbling, which only takes *ca*. 30 minutes, depending on scan parameters.

6.2 *IN SITU* STUDIES OF THE 150 °C COMPOSITE

The *in situ* electrochemical-XAS studies were performed on the 150 °C composite in both fluorescence and transmission modes to see which mode would give the highest quality data. The EXAFS regions were converted to k-space and overlain to compare the noise, shown in Figure 26.
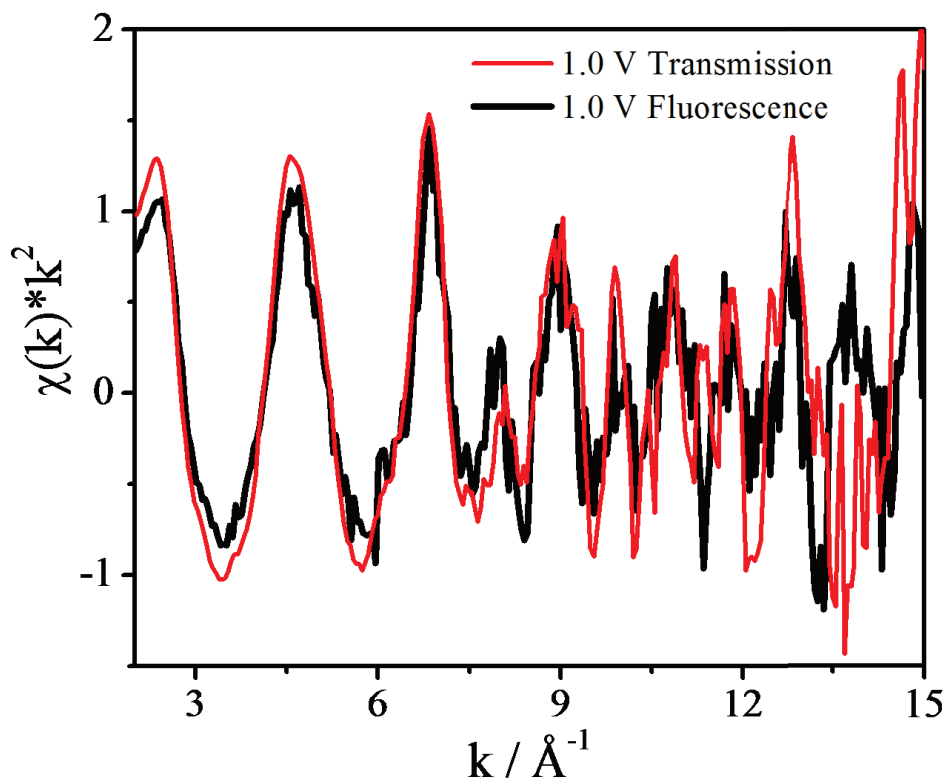

Figure 26: k-space spectra for 150 °C composite collected *in situ* at 1.0 V in transmission mode and fluorescence mode.

Both spectra were collected with the working electrode held at 1.0 V vs. Ag/AgCl, and the transmission mode data (red, thin line) showed less noise than the fluorescence data (black, thick line). Typically, if the element of interest is very dilute in the sample, then the sample will have to be thick to obtain high absorption. This can cause beam attenuation, and therefore fluorescence may be preferred for thick samples over transmission. However, if the fluorescence detector is not of the highest quality then the fluorescence quality may be lower than the transmission quality, even for dilute samples, which may be the cause here. Transmission mode was used for the other potentials of the 150 °C composite, as well as for the other *in situ* data collected. It should be noted that although the transmission mode data is smoother than the fluorescence mode data, it is still noisy in comparison to Figure 11 of the RuO_2/carbon composites not collected *in situ*.

The XANES regions for the 150 °C composite held at 0.0 and 1.0 V vs. Ag/AgCl were previously compared in Chapter 4, showing no difference between one another. The EXAFS region was converted to the k-space and subsequent R-space. As seen in Figure 26, the k-space data is rather noisy at high k, so the Fourier transformation was performed from $3 \leq k \leq 12$ Å^{-1}. The 0.0 V (dashed line) and 1.0 V (solid line) R-space data are shown in Figure 27.
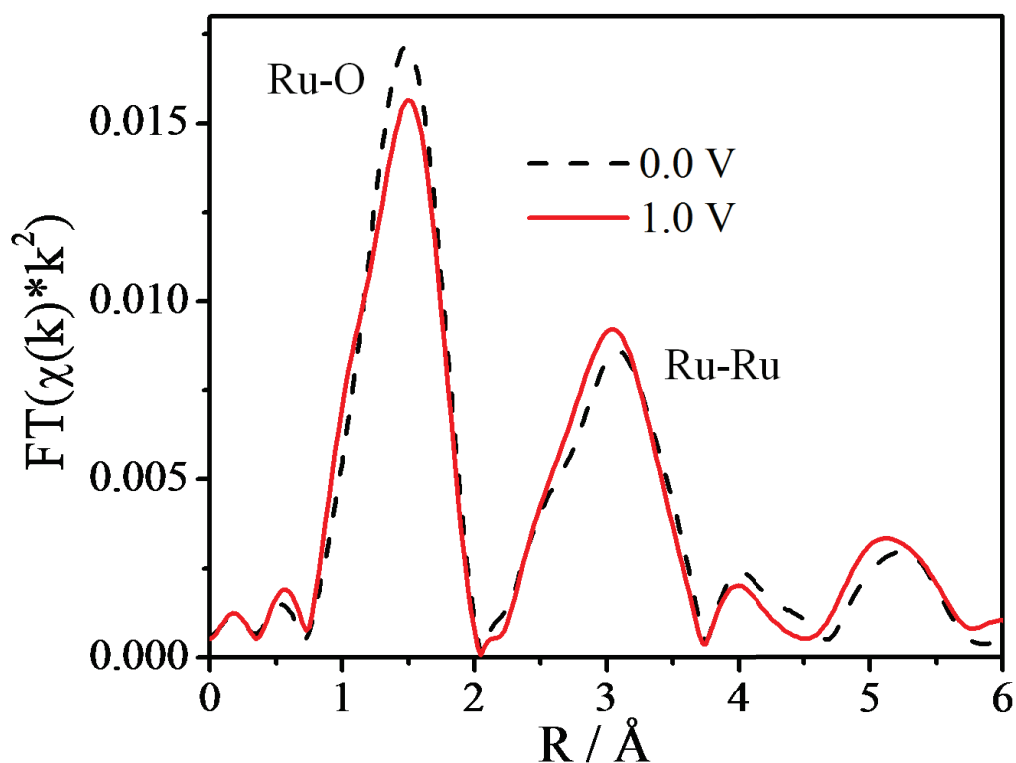
Figure 27: R-space spectra for the 150 °C composite collected *in situ* at both 0.0 V and 1.0 V.

When the working electrode potential was increased from 0.0 to 1.0 V, the intensity of the Ru-O peak decreased slightly, and there was also a slight increase in the Ru-Ru peak intensity. This data could suggest that the octahedral Ru-O shell becomes disordered and there is an ordering of the Ru-Ru shell upon oxidation. However, there were no changes observed in the XANES region with a change in potential for this sample because the majority of the RuO_2 is not electrochemically active. Also, the noise in the k-space data is high, the changes in the R-space are subtle, all indicating that it is not likely these differences in the R-space are reliable. Refinement of the R-space spectra was attempted. However the values obtained were not reliable, yielding values much different than expected, which again could be due to the high noise level of the data.

6.3 *IN SITU* STUDIES OF THE BULK RUO$_2$·xH$_2$O

In situ studies were also performed on bulk $RuO_2 \cdot xH_2O$ powder (Alfa Aesar). Differences between the XANES regions of the sample held at 0.0 V and 1.0 V were previously discussed, and were consistent with changes seen in the literature.[64] Although only the lowest potential (0.2 V) and highest potential (1.0 V) were shown in the XANES graph, intermediate potentials of 0.4, 0.6, and 0.8 V were also collected. The changes with potential in the XANES region are not as apparent when all potentials are plotted on together, shown in Figure A.3 of Appendix A. The EXAFS regions of all potentials were converted to the k-space, shown in Figure 28. The k-space spectra were offset on the y-axis for comparison, and the arrow indicates increasing potential from 0.2 to 1.0 V.
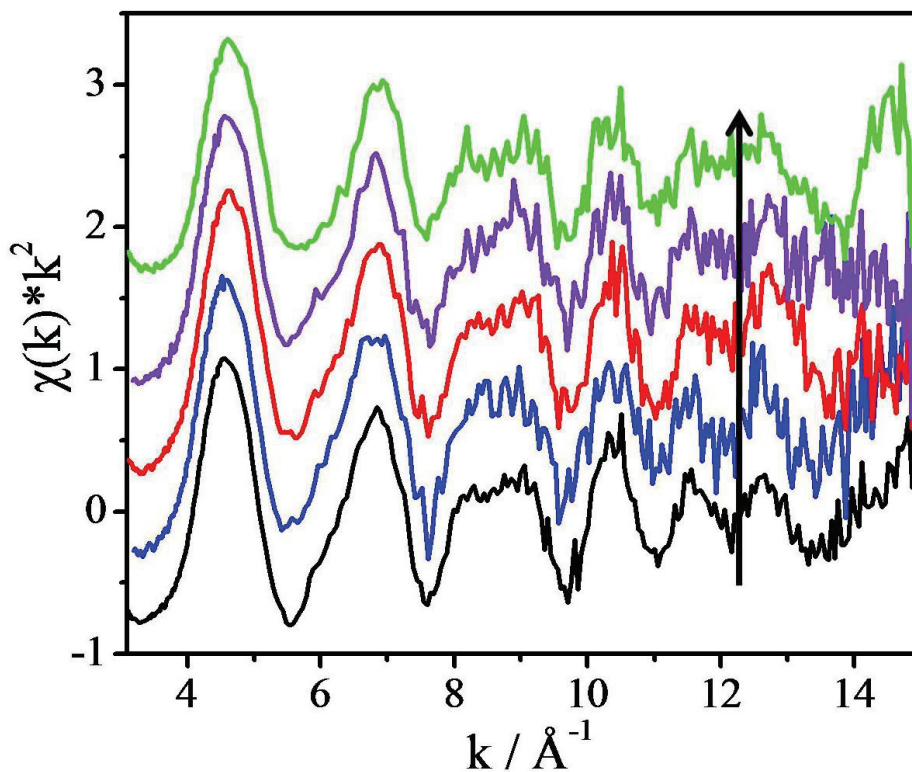

Figure 28: k-space spectra for the bulk RuO$_2$·xH$_2$O collected *in situ* at 0.2 V (black), 0.4 V (blue), 0.6 V (red), 0.8 V (purple), and 1.0 V (green).

The data is again noisy, as with the previous results, and no obvious changes can be discerned between the different potentials in the k-space. However, below k = 12 Å, the oscillations in all the k-space are evident. The Fourier transformation was performed over the range of $3 \leq k \leq 12$ Å^{-1}, and the resulting R-space spectra are shown in Figure 29.
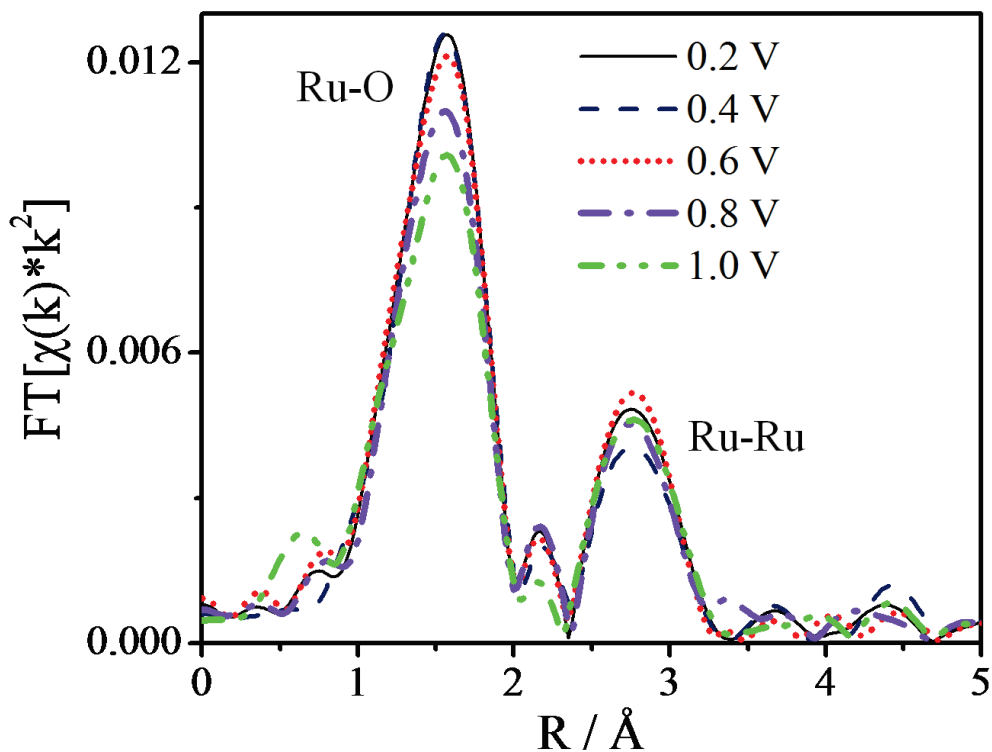

Figure 29: R-space spectra for the bulk RuO$_2$·xH$_2$O collected *in situ* at 0.2, 0.4, 0.6, 0.8, and 1.0 V.

As the potential of the working electrode is increased from 0.4 to 1.0 V, the intensity of the Ru-O peak decreases. This decrease in intensity could be due to a decrease in coordination number, as observed with the different intensities of the Ru-Ru peak in the 150 to 300 °C composites (Chapter 4). Also, a decrease in intensity of this Ru-O peak may indicate a decrease in ordering of the Ru-O, as seen with the 25 and 100

°C composites in Chapter 4, which had a decreased Ru-O peak intensity relative to the 150 to 300 °C composites, but had the same coordination number.

There appears to be no trend in the Ru-Ru peak for the *in situ* bulk $RuO_2 \cdot xH_2O$ R-space. In a study by Mo *et al.*,[64] for a RuO_2 film deposited on Au, the Ru-Ru shell completely disappeared when the RuO_2 film was reduced, indicating a decrease in long range order of the structure. This does not occur in our bulk $RuO_2 \cdot xH_2O$, suggesting the long range order does not change drastically. Perhaps the different forms of RuO_2 (film vs. bulk) behave differently with changes in potential, or perhaps some of the bulk $RuO_2 \cdot xH_2O$ is not electroactive and does not change with potential. The peak at 2.2 Å for the 1.0 V scan is decreased in intensity relative to all other spectra. Recall that this peak is possibly due to Ru-OH interactions. This correlates well with the RuO_2 charge storage mechanism (Scheme 1) as there should be less Ru-OH bonds upon oxidation. This mechanism is discussed in more detail below.

To test whether the observed changes in the R-space were reliable rather than an artifact of noise in the k-space, the FT was performed over the ranges $3 \leq k \leq 11$ Å^{-1} and $3 \leq k \leq 13$ Å^{-1}, shown in (a) and (b) in Figure 30, respectively.

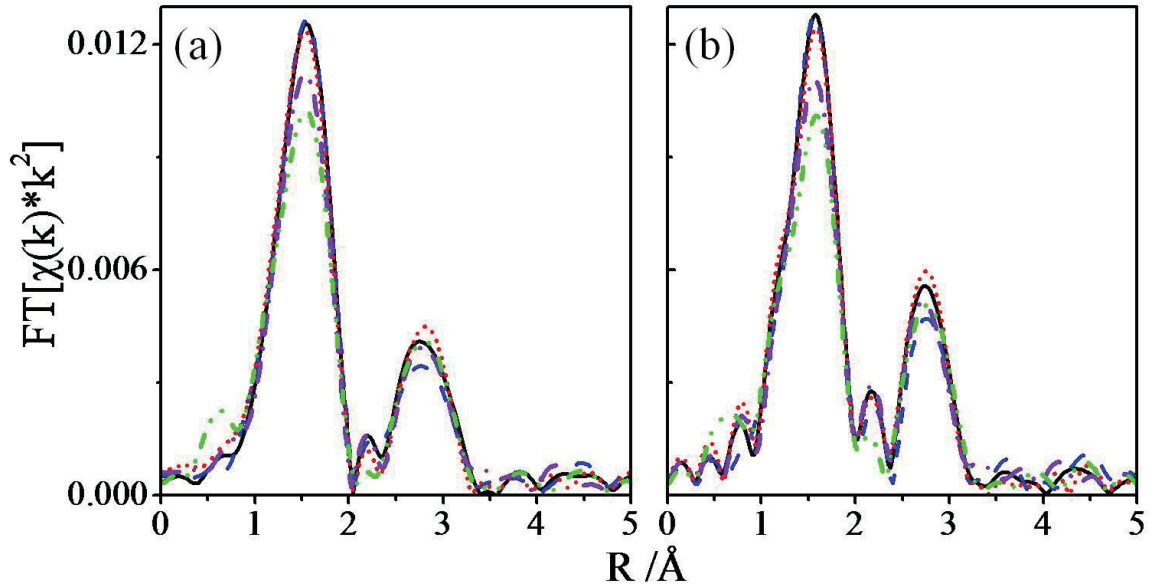**Figure 30: R-space spectra for the bulk $RuO_2 \cdot xH_2O$ collected *in situ*, with FT ranges of a) $3 \leq k \leq 11$ Å^{-1} and b) $3 \leq k \leq 13$ Å^{-1}.**

All of the changes observed for the first k range (3 to 12 Å^{-1}) apply to the latter two (3 to 11 Å^{-1} and 3 to 13 Å^{-1}) as well, indicating that the trends are not simply due to noise in the high k region. All R-space spectra (for $3 \leq k \leq 12$ Å^{-1}) were refined using the method described previously, starting with the least noisy data, 0.2 V, to obtain values for S_0^2 and E_0. The refinements are shown in Figure 31, and the obtained parameters are shown in Table 6. The errors of the refinement were calculated by doubling the χ^2 obtained for the fit, as described previously with the *ex situ* RuO_2 composites in Chapter 4.
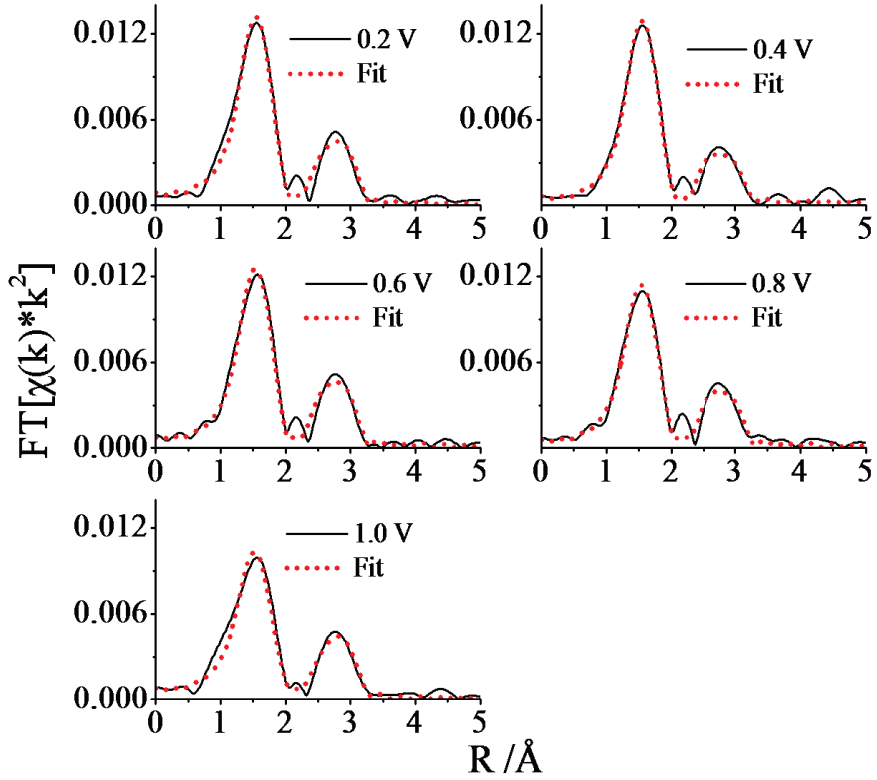
Figure 31: Fits of the R-space spectra for bulk RuO₂·xH₂O collected *in situ* at 0.2, 0.4, 0.6, 0.8, and 1.0 V.

Table 6: R-space fitting results for bulk RuO₂·xH₂O.*

Potential	Shell	R / Å	N / atoms	σ^2 / Å^2
0.2 V	Ru-O	2.03±0.02	4.5±0.8	0.004±0.002
	Ru-Ru	3.11±0.04	1.9±0.7	0.004±0.003
0.4 V	Ru-O	2.03±0.02	4.4±0.6	0.004±0.002
	Ru-Ru	3.11±0.04	1.8±0.7	0.005±0.003
0.6 V	Ru-O	2.02±0.02	4.5±0.7	0.005±0.002
	Ru-Ru	3.10±0.04	1.6±0.6	0.003±0.003
0.8 V	Ru-O	2.02±0.02	4.3±0.7	0.005±0.002
	Ru-Ru	3.12±0.04	1.4±0.6	0.003±0.004
1.0 V	Ru-O	2.01±0.02	3.9±0.6	0.006±0.002
	Ru-Ru	3.11±0.03	2.5±0.7	0.006±0.003

*The optimum fits were obtained with $S_0^2 = 0.90$, E_0 (Ru-O) = -1.87 eV, and E_0 (Ru-Ru) = -6.50 eV.

There are no significant differences in the parameters with changing potential. However, the N of the Ru-O peak may have a slight decreasing trend. If this trend was significant, it would suggest that increasing the potential and oxidizing the bulk $RuO_2 \cdot xH_2O$ causes a lower coordination of Ru to surrounding oxygen atoms. Recall the mechanism for the charge storage in hydrous RuO_2 in Scheme 1. As the RuO_2 is oxidized, it also loses H^+, and should therefore contain more Ru-O bonds and less Ru-OH bonds. The observed trend in the R-space would be contrary to what is expected based on this mechanism. As mentioned, a decrease in intensity of the Ru-O peak could also be a result of a decrease in ordering of the Ru-O shell, which may be more likely given that there are no significant changes in the N. Therefore, it appears that increasing the potential applied to RuO_2 may cause a decrease in the ordering of the Ru-O shell.

Comparing with the RuO_2 nanoparticles in the composites (Chapter 4), all of the Ru-O bonds for bulk $RuO_2 \cdot xH_2O$ are longer (*ca.* 2.02 Å) than those obtained for the heavily hydrated RuO_2 nanoparticles, which were 1.98 Å. This may indicate that the $RuO_2 \cdot xH_2O$ nanoparticle Ru-O shell is more similar in structure to the theoretical crystalline RuO_2 Ru-O shell (with Ru-O bond length of 1.96 Å) than the bulk $RuO_2 \cdot xH_2O$. This is further supported by the N values obtained by the refinement, which show a maximum N of 4.5 for the Ru-O shell, while the hydrated nanoparticle Ru-O shell maintained an N of *ca.* 6.

6.4 CONCLUSIONS

The preliminary *in situ* electrochemical-XAS studies were able to detect changes in both the XANES and EXAFS regions for the Ru K-edge of bulk $RuO_2 \cdot xH_2O$. The XANES changes were subtle, but similar to those seen in literature.[64] For the EXAFS, as

the potential of the working electrode was increased, the intensity of the Ru-O shell decreased. Although the exact reason for this trend is unknown, it is hypothesised that it is due to an increase in disorder of the Ru-O shell with increasing potential. No changes were observed in the XAS spectrum for the 150 °C composite, likely due to the fact that the majority of the material is not electrochemically active.

CHAPTER 7: PRELIMINARY ELECTRODEPOSITION OF $RuO_2 \cdot xH_2O$

7.1 INTRODUCTION

The electrodeposition of $RuO_2 \cdot xH_2O$ on titanium substrates has been extensively researched by Hu *et al.* with regards to many deposition conditions, including the deposition bath initial pH, preheating temperature and deposition temperature, bath storage time, as well as supporting electrolyte concentrations and the potential limits and scan rates of the cyclic voltammogram.[38, 70, 71] Electrodeposition has also been applied to other substrates, including stainless steel,[72] carbon nanotubes,[17, 73] and gold foil.[64] The goal of this work was to perform electrodeposition of $RuO_2 \cdot xH_2O$ onto different areas of the Spectracarb 2225 carbon cloth by varying the deposition sweep rate. Equation 1 shows that solution resistance is higher in smaller pores. By applying a relatively faster sweep rate, deposition may occur on less of the carbon surface, avoiding the most resistive pores (micropores, < 2 nm) and only depositing on the larger pores (mesopores, 2 to 50 nm) or the outer electrode surface. A slow sweep rate may allow for deposition onto more of the carbon cloth surface, however the exact areas of the carbon which will be accessed at certain sweep rates is not known, and determining this is another goal of this project.

7.2 ELECTRODEPOSITION ON Au FOIL

Before electrodepositing $RuO_2 \cdot xH_2O$ on the carbon cloth, a Au foil substrate was used for trial runs. It was presumed that the planar Au surface would be easier to deposit onto than the complex carbon cloth surface. The synthesis performed was similar to that used by Mo *et al.*[64] The deposition bath contained 2.5 mM $RuCl_3 \cdot xH_2O$ and 0.10 M KNO_3, and the deposition was performed at 20 mV s^{-1} from -0.2 to 1.0 V. Figure 32

shows cyclic voltammograms from the electrodeposition, with the arrows indicating an increasing current from cycle 2 (blue line) to cycle 60 (light red line).
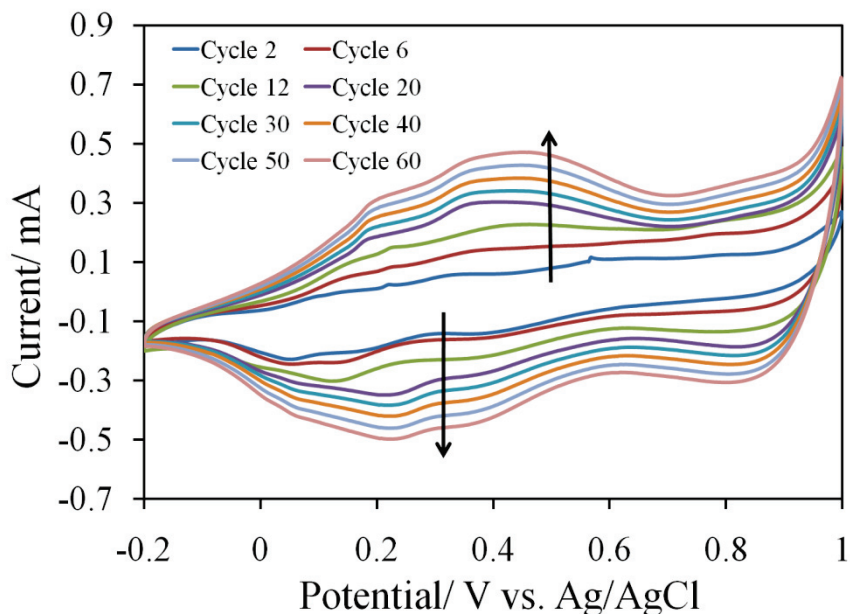

Figure 32: Electrodeposition of RuO$_2$·xH$_2$O onto Au foil at 20 mV s^{-1}, in 2.5 mM RuCl$_3$·xH$_2$O. Arrows indicate increasing current with cycle number.

The current increases during the electrodeposition as the working electrode becomes more capacitive with RuO$_2$·xH$_2$O formed on the Au foil substrate. The increased surface area of porous RuO$_2$·xH$_2$O (surface area of *ca.* 200 F g^{-1})[68] compared to a piece of Au foil, and the high pseudocapacitance of RuO$_2$·xH$_2$O cause the working electrode to become more capacitive. The cyclic voltammograms contain oxidation peaks at *ca.* 0.2, 0.4, and 1.0 V and reduction peaks at *ca.* 0.2, 0.4, and 0.85 V. The reduction peak at *ca.* 0.2 V is associated with the reduction of Ru(III) species to either metallic Ru and/or oxy-chloro-ruthenium species.[38] These species become oxidized to RuO$_x$·nH$_2$O (hydrous ruthenium oxide, assumed to be RuO$_2$·xH$_2$O in this work) when the potential is swept in the positive direction again, indicated by the oxidation peaks at 0.2 and 0.4 V, and further oxidized to hydroxyl Ru(VI) species at 1.0 V.[38] The subsequent negative sweep would

reduce the higher oxidation states back to $RuO_x \cdot nH_2O$ at 0.85 V, and finally at lower potentials deposit more Ru(III).

The Au foil with deposited $RuO_2 \cdot xH_2O$ was then transferred to 1.0 M H_2SO_4, and the cyclic voltammograms collected on the electrode are shown in Figure 33.
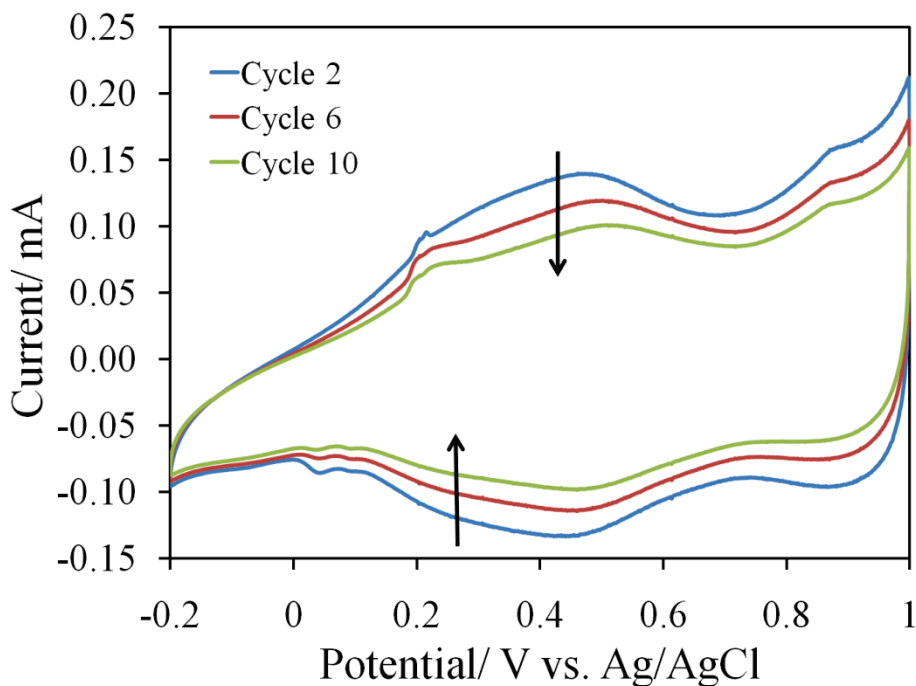

Figure 33: Cyclic voltammograms of $RuO_2 \cdot xH_2O$ onto Au foil in 1 M H_2SO_4, with arrows indicating decreasing current with cycle number.

There are two main oxidation and reduction peaks in the cyclic voltammograms. The first is in the range of 0.2 to 0.6 V, due to Ru(II)/Ru(III)/Ru(IV) transitions, and the second is from 0.7 to 1.0 V, due to Ru(IV)/Ru(VI) redox couples.[38] The arrows indicate increasing cycle number, and it can be seen that the current is decreasing with increasing cycle number from cycle 2 (blue line) to cycle 10 (green line). The current quickly decreased, and the ruthenium oxide species was visually observed dissolving off the Au surface in the electrolyte. The reason for this dissolution was unclear therefore a few modifications to the synthesis were made. In the following electrodeposition experiment,

the deposition bath was bubbled with O_2 to try to promote the formation of ruthenium oxide, as used by Mo *et al.*[64] Also, the sweep rate was increased to 50 mV s^{-1}, which was used in a literature study by Hu *et al.*,[38] and the Au foil was polished before the deposition. The cyclic voltammograms for the deposition are shown in Figure 34.
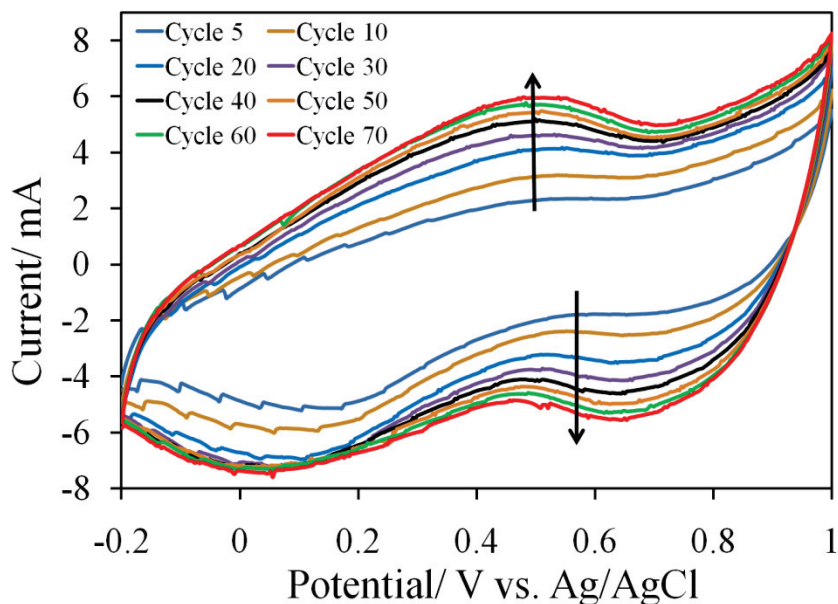

Figure 34: Electrodeposition of RuO$_2$·xH$_2$O onto Au foil at 50 mV s^{-1}, in 2.5 mM RuCl$_3$·xH$_2$O. Arrows indicate increasing current with cycle number.

The arrows indicate increasing cycle number, and shown are cycle 5 (blue line) to cycle 70 (red line). The electrodeposition was stopped when there was no visible change in current between cycles. These cyclic voltammograms have similar characteristics to those seen in Figure 32, however the oxidation/reduction peaks show more irreversible behaviour (they are further apart on the oxidation and reduction curves). This irreversibility may be a result of the faster sweep rate employed, and that the pseudocapacitive redox reactions can not keep up with the potential. After the deposition, the working electrode was rinsed with deionized water. The electrode was then immersed in 1.0 M H$_2$SO$_4$, and cyclic voltammetry experiments were performed with small

potential windows to determine its effect on the stability of the $RuO_2 \cdot xH_2O$ film. The resulting cyclic voltammograms collected at 5 mV s^{-1} are shown in Figure 35.

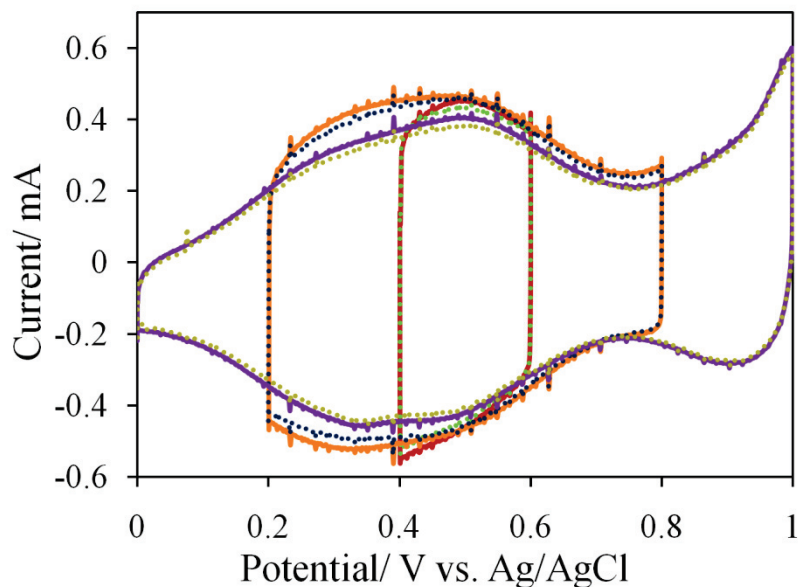**Figure 35: Cyclic voltammograms of $RuO_2 \cdot xH_2O$ on Au foil at 5 mV s^{-1} with small potential windows, in 1 M H_2SO_4.**

The potential ranges used were 0.4 to 0.6 V, 0.2 to 0.8 V, and finally 0.0 to 1.0 V. At each potential range, there is a cyclic voltammogram for cycle 2 (solid line) and cycle 5 (dotted line). The smallest potential window was run first, and there appeared to be little difference between the current of cycle 2 and cycle 5, however, when the 0.2 to 0.8 V window was run, there was an evident decrease in the current, and the $RuO_2 \cdot xH_2O$ was again observed dissolving into solution. A brief annealing step after deposition has been employed in literature,[17] presumably to form a more stable product, and thus annealing the Au foil with $RuO_2 \cdot xH_2O$ for 1 hour at 50 °C was performed. The annealed $RuO_2 \cdot xH_2O$ component was found to also not be stable in the acid electrolyte, and a decrease in capacitance was observed with the larger potential windows of 0.2 to 0.8 V and 0.0 to 1.0 V, shown in Figure B.1 of Appendix B.

With the previous depositions being unsuccessful, it was decided that a synthesis by Hu *et al.*[38] would be followed. The deposition bath consisted of 5 mM $RuCl_3 \cdot xH_2O$, 0.01 M HCl, and 0.1 M KCl, with the initial pH of the bath adjusted to 1.96 via NaOH addition. The deposition was performed at 50 °C with a sweet rate of 50 mV s^{-1} from -0.2 to 0.8 V. The cyclic voltammograms for the electrodeposition are shown in Figure 36. The arrows indicate increasing current with cycle number, from cycle 2 (light red line) to cycle 120 (black line).
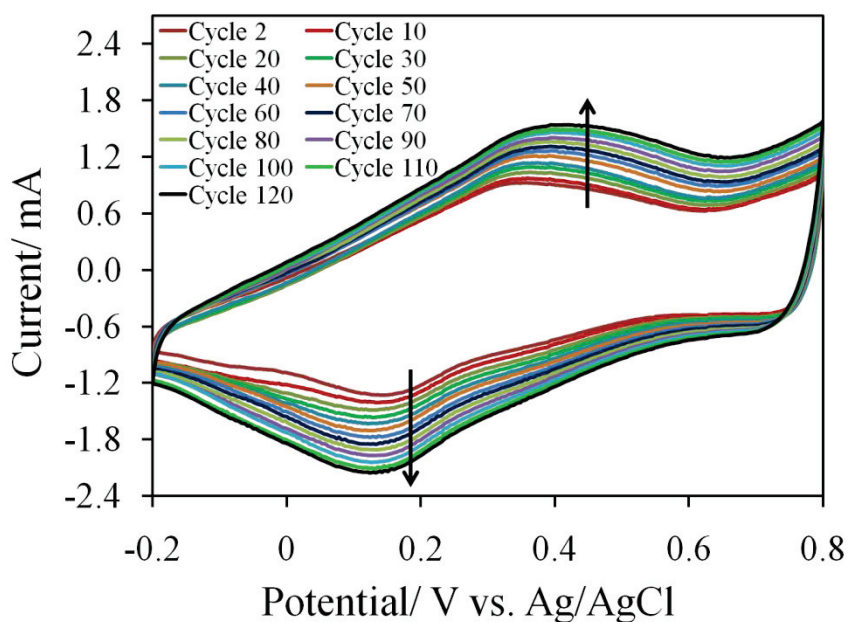

Figure 36: Electrodeposition of $RuO_2 \cdot xH_2O$ onto Au foil at 50 mV s^{-1}, and at 50 °C, in 5 mM $RuCl_3 \cdot xH_2O$. Arrows indicate increasing current with cycle number.

The electrode was transferred to 0.5 M H_2SO_4, which is less concentrated than the 1.0 M H_2SO_4 used previously, to determine if it would aid in the cycle life, and the small potential windows were employed. The electrode appeared stable in the 0.4 to 0.6 V window at 10 mV s^{-1}, therefore many cycles were performed in this window to test the stability, shown in Figure 37. The arrows indicate increasing cycle number, from cycle 10 (blue line) to cycle 80 (red line).
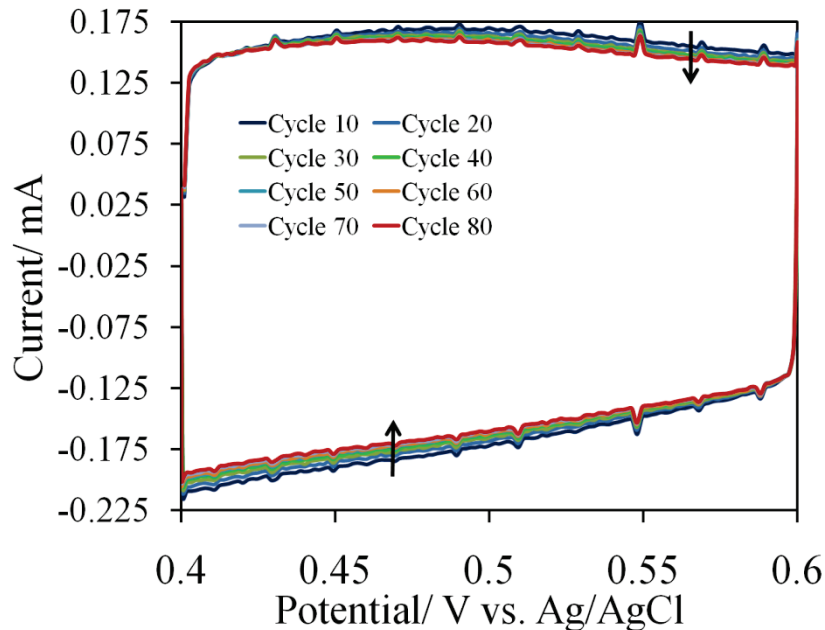
Figure 37: Cyclic voltammograms of RuO$_2$·xH$_2$O on Au foil at 10 mV s^{-1} with a 0.4 to 0.6 V potential window in 0.5 M H$_2$SO$_4$.

The RuO$_2$·xH$_2$O appears to be stable with in this potential window, with little decrease in current and little to no observed dissolution of the film. However, because the energy stored is related to the voltage through Equation 15, this is obviously not a practical potential window because the G is proportional to V^2. When the potential window was increased to a larger range (0.2 to 0.8 V), the RuO$_2$·xH$_2$O was again not stable, indicated by the decrease in current in Figure B.2 of Appendix B. The electrodeposition onto planar Au foil was originally planned to be a facile trial run compared to the deposition onto a complex substrate such as the carbon cloth, however, the Au deposition proved troublesome, perhaps due to the Au substrate causing issues. For the sake of time in this project, and that the Au deposition was not the goal of the work, the focus was shifted to the deposition onto a carbon cloth substrate.

7.3 ELECTRODEPOSTION ON CARBON CLOTH

Originally, the electrodeposition conditions were the same as the previous synthesis, following the procedure by Hu *et al.*[38] The sticky carbon current collector used in the Swagelok electrode holder was not ideal for this synthesis because the deposition is done at 50 °C, and the current collector would become soft at this temperature due to the wax component. Also, the Swagelok holder itself was not ideal because one whole geometric surface of the carbon cloth electrode would be against the current collector, and it may block deposition from occurring on part of electrode surface. As an alternative, a piece of Au wire was woven through a carbon cloth electrode, with no additional holder or support. The resulting cyclic voltammograms from 1 mV s^{-1} to 50 mV s^{-1} are shown in Figure 38, and the 4 mV s^{-1} cyclic voltammogram is shown by itself in Figure 39.
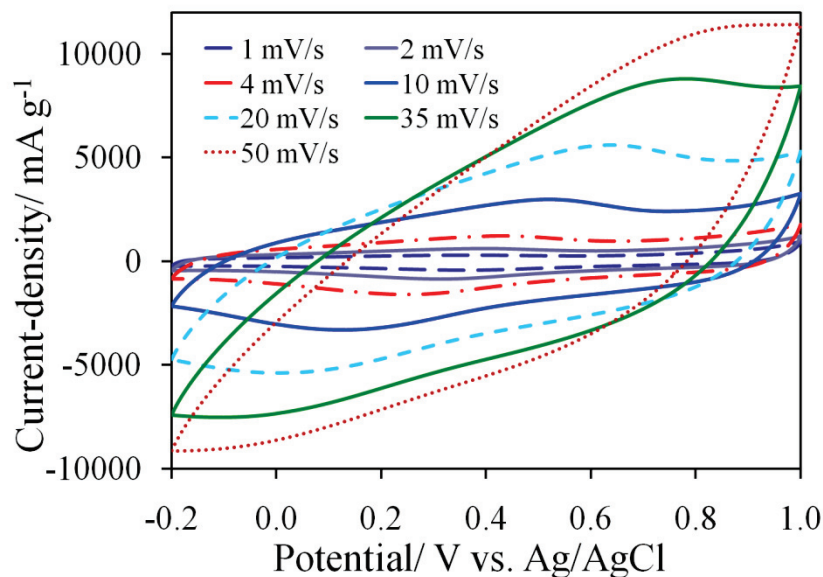

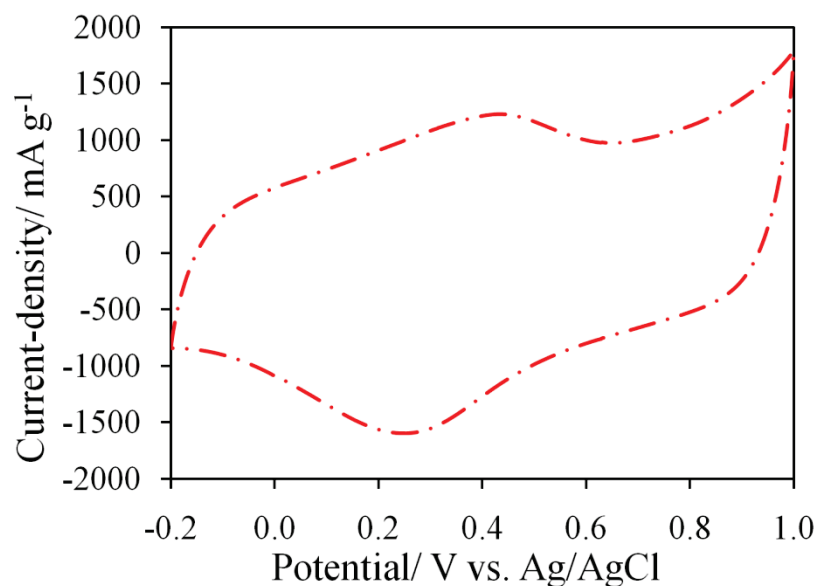**Figure 38: Cyclic voltammograms of Au wire woven through carbon cloth, at 1 mV s^{-1} to 50 mV s^{-1} in 1.0 M H$_2$SO$_4$.**

Figure 39. Cyclic voltammograms of Au wire woven through carbon cloth, at 4 mV s^{-1} in 1.0 M H$_2$SO$_4$.

The cyclic voltammograms for the carbon cloth electrode at low sweep rates (below *ca*. 10 mV $^{s-1}$) exhibit a more rectangular shape, indicating good capacitive behaviour. Also, the pseudocapacitance peak from the quinone/hydroquinone oxidation/reduction couple can be observed as the broad peaks in each cyclic voltammogram. For the 4 mV s^{-1} scan, the peaks are located at 0.4 V on the oxidation curve and 0.3 V on the reduction curve. The peaks become less reversible (farther apart) as the sweep rate is increased. Also, the peak at about 1.0 V is possibly the beginning of O$_2$ evolution, and it more evident in the slower sweep rates.

This arrangement has fairly reversible cyclic voltammograms at low sweep rates, but began to tilt and show resistance at about 20 mV s^{-1}. In an ideal capacitor, a plot of current versus sweep rate will increase linearly. In many supercapacitors, the electrode will not exhibit ideal capacitor behaviour at high sweep rates, and the plot of current versus sweep rate will deviate from linearity, as seen after *ca.* 20 mV s^{-1} in Figure 40.
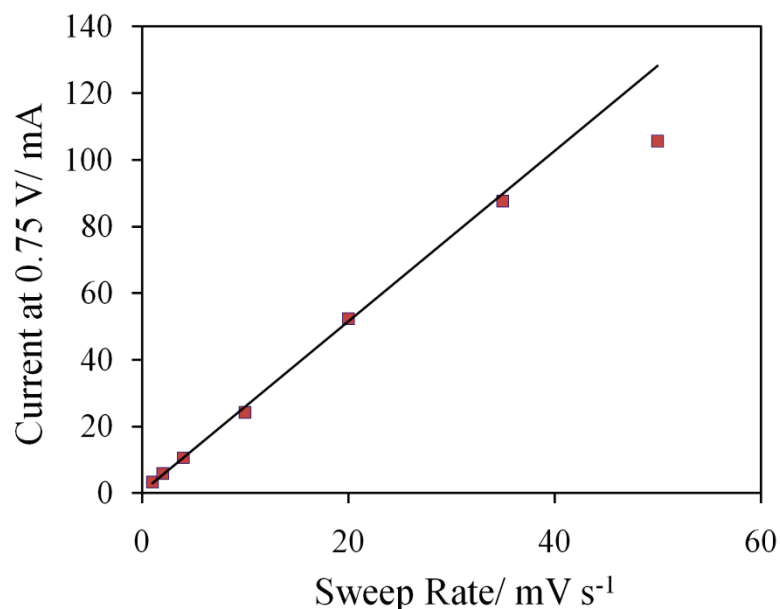
94

Figure 40: Plot of current against sweep rate of carbon cloth woven by Au wire.

The line in Figure 40 is a fit of the linear region of the data (up to 20 mV s^{-1}), and the fit is extrapolated to show the deviation from linearity of the 35 and 50 mV s^{-1} points. It should be noted that the y-axis in Figure 40 is labelled current at 0.75 V because we chose to measure the current at a consistent location on the various cyclic voltammograms, and a location which contains mostly double-layer capacitance rather than pseudocapacitance. This plot may be useful in determining the approximate sweep rates which are ideal for the electrodeposition on different areas of the carbon. If the current versus sweep plot deviates from linearity, it may indicate that the more narrow pores can not keep up with the sweep rate, and therefore $RuO_2 \cdot xH_2O$ may only deposit in the larger mesopores or on the surface. However, this deviation from linearity could be due to multiple factors.

The Au wire woven through the carbon cloth appeared to work. However, the carbon cloth was not well supported by the wire and tended to fall apart after some time

in the electrolyte. Because of this, a custom electrode holder was developed to support the electrode around the outer edge, shown in Figure 41.

Figure 41: Custom carbon cloth electrode holder.

The holder is made of PTFE, and the top cap connects into the bottom base, sandwiching the Au foil and carbon cloth resulting in good structural stability and electrical connection. The carbon cloth is supported around the entire outer edge by the coiled Au wire, similar to the Swagelok design but with access at both top and bottom in the deposition bath or electrolyte. The cyclic voltammograms for a carbon cloth electrode at various sweep rates in this holder are shown in Figure 42, and the cyclic voltammogram at 4 mV s^{-1} is shown in Figure 43.
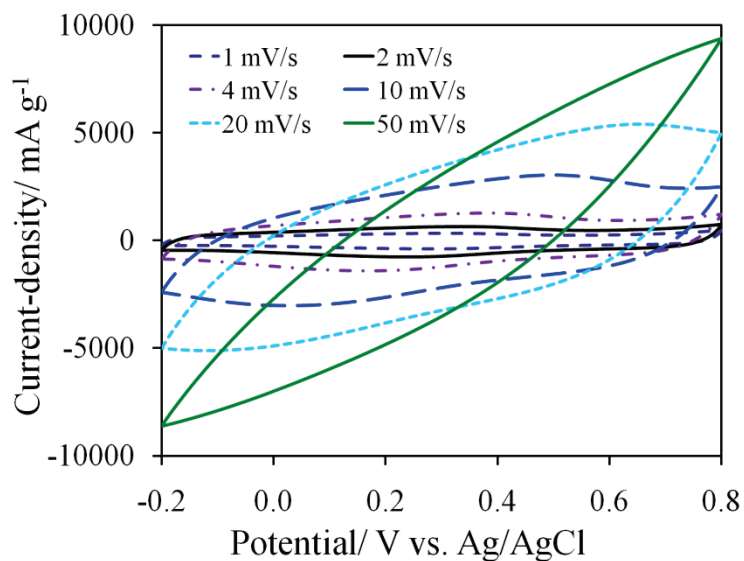
Figure 42: Cyclic voltammograms of a carbon cloth electrode in custom holder, at various sweep rates.
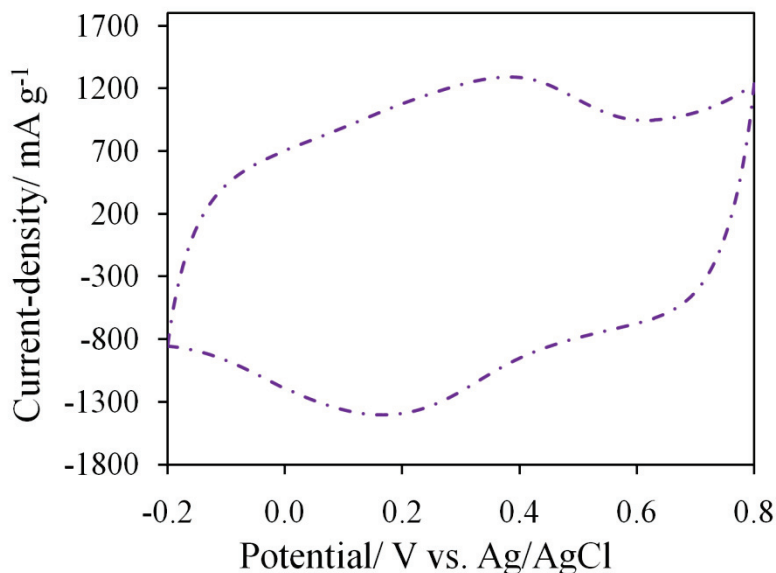

Figure 43: Cyclic voltammogram of a carbon cloth electrode in custom holder at 4 mV s^{-1}.

The cyclic voltammograms at low sweep rates have the more ideal rectangular shape, indicative of capacitive behaviour, but begin to show resistance at sweep rates of *ca.* 10 mV s^{-1}. The highest sweep rate of *ca.* 50 mV s^{-1} has more resistive characteristics than the carbon cloth which was woven with a Au wire in Figure 38, however the custom

holder was used for further studies because it supported the carbon cloth electrode much more efficiently. The plot of current versus sweep rate for the carbon cloth electrode in the custom holder is shown in Figure 44.
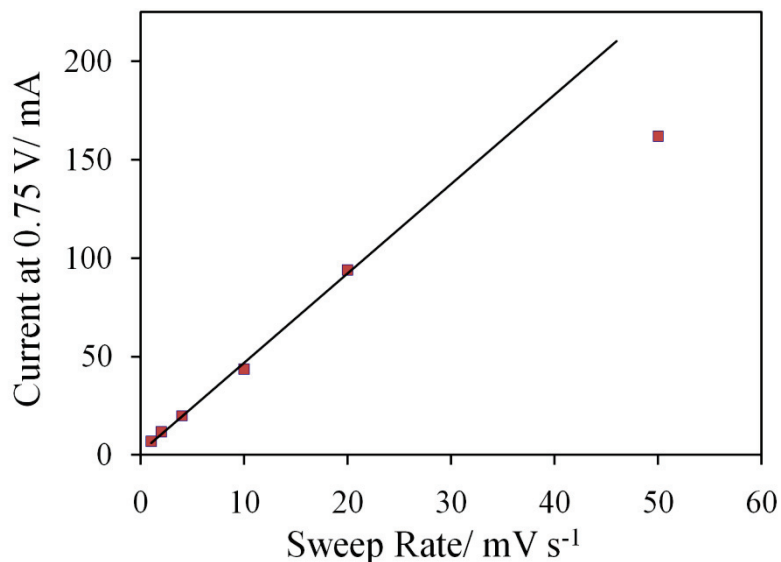

Figure 44: Plot of current versus sweep rate for a carbon cloth electrode in custom holder.

Figure 44 deviates from linearity at sweep rates above *ca.* 20 mV s^{-1}. For the electrodeposition experiments, a sweep rate around this value or above may not utilize the small pores as efficiently, and only deposit $RuO_2 \cdot xH_2O$ on the larger pores or the outer electrode surface. Slow sweep rates of *ca.* 1 mV s^{-1} may deposit $RuO_2 \cdot xH_2O$ onto more of the electrode surface, including the small pores.

Before the electrodeposition could be performed, another variable had to be addressed. It was hoped that at the high sweep rates, electrodeposition would not occur in the small pores. However, if the electrode is in the deposition bath for an extended period of time during the deposition, it is possible that the Ru(III) ions will diffuse into the smaller pores. The penetration depth of the current on the electrode may not access the

small pores at high sweep rates, and thus the Ru(III) ions would be present but would not be reduced and deposited. Then, when a slower sweep rate is applied to test the capacitance, the Ru(III) ions in the smaller pores may be reduced and deposited onto the carbon.

To test this hypothesis, a cyclic voltammogram was performed on a carbon cloth electrode at 1 mV s^{-1} in 1.0 M H$_2$SO$_4$. The cloth was then soaked in the deposition bath for six hours, with no electrochemistry being performed, to allow the ions to diffuse into the smaller pores of the carbon. The carbon cloth was removed from the deposition bath and soaked in deionized water for one hour, and then another cyclic voltammogram was performed on the electrode in 1.0 M H$_2$SO$_4$ at 1 mV s^{-1}. The before soaking and after soaking cyclic voltammograms are shown in Figure 45.

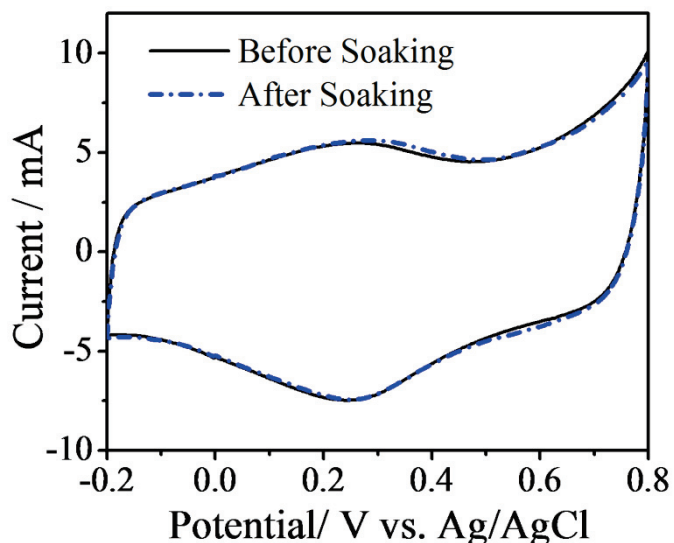**Figure 45: Cyclic voltammograms of a carbon cloth electrode at 1 mV s^{-1} in 1.0 M H$_2$SO$_4$ before and after soaking in deposition bath.**

There is no significant difference in the current between the two cyclic voltammograms, indicating that there is no reduction or oxidation of Ru(III) ions.

99

Therefore, after the electrodeposition is performed, soaking the electrode for one hour in deionized water should remove any residual electroactive deposition species.

The initial electrodeposition was performed at 50 mV s^{-1}. The deposition bath is more resistive than the 1.0 M H_2SO_4, and a resulting cyclic voltammogram from the electrodeposition is shown in Figure 46.
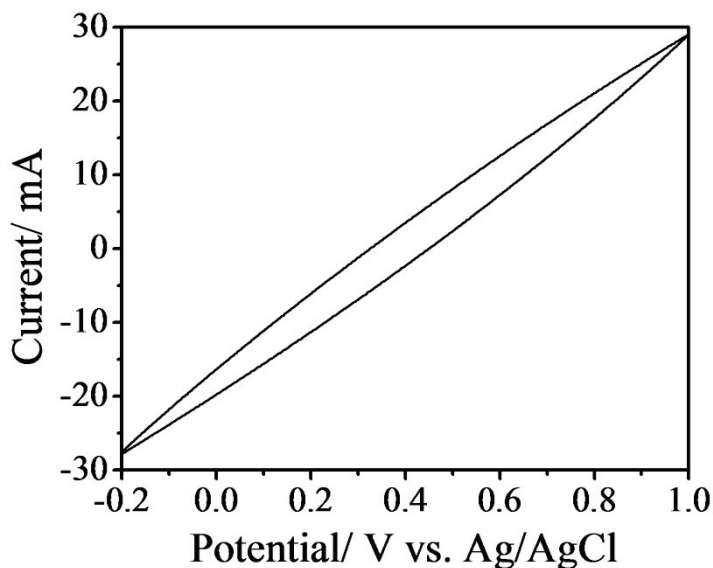

Figure 46: Electrodeposition onto carbon cloth at 50 mV s^{-1}, in 5 mM RuCl$_3$·xH$_2$O.

After 20 cycles at this sweep rate, there was still no difference in the capacitance of the carbon cloth electrode, indicating that there was no $RuO_2 \cdot xH_2O$ deposited. The 50 mV s^{-1} sweep rate was too fast to allow for deposition to occur, and so the electrodeposition was then performed at slower deposition rates of 1 and 2 mV s^{-1}. The cyclic voltammograms still exhibited resistive behaviour, although to a lesser degree, shown in Figure 47.
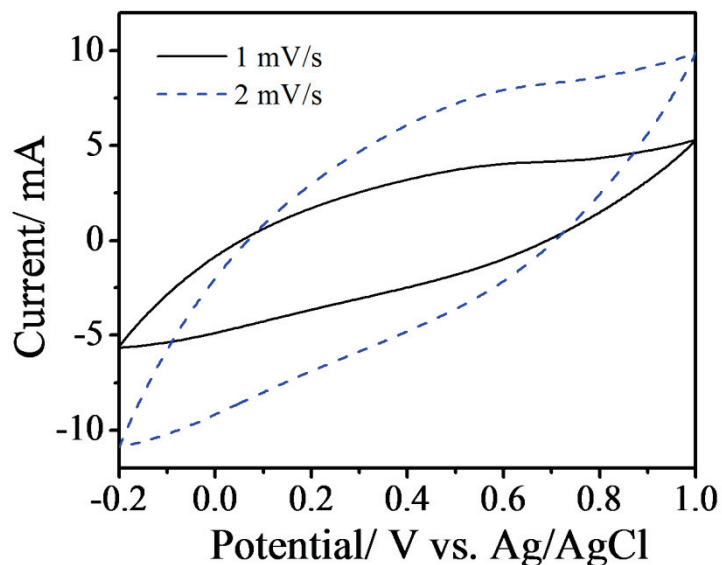
Figure 47: Electrodeposition of RuO$_2$·xH$_2$O onto carbon cloth at 1 and 2 mV s^{-1}, in 5 mM RuCl$_3$·xH$_2$O.

After 25 cycles at the slow sweep rates, there was little or no change to the capacitance of the electrode materials, indicating that no RuO$_2$·xH$_2$O had deposited. Also, these sweep rates are not ideal for the deposition as it would take an exceptionally long time to make the electrodes. The deposition bath was then altered slightly to have a higher initial pH of 2.5 rather than 1.96, because this pH was shown to give the maximum rate of deposition of RuO$_2$·xH$_2$O in another paper by Hu *et al.*[70] The next deposition was performed with a sweep rate of 4 mV s^{-1}, for 50 cycles, and the cyclic voltammograms for the deposition are shown in Figure 48.
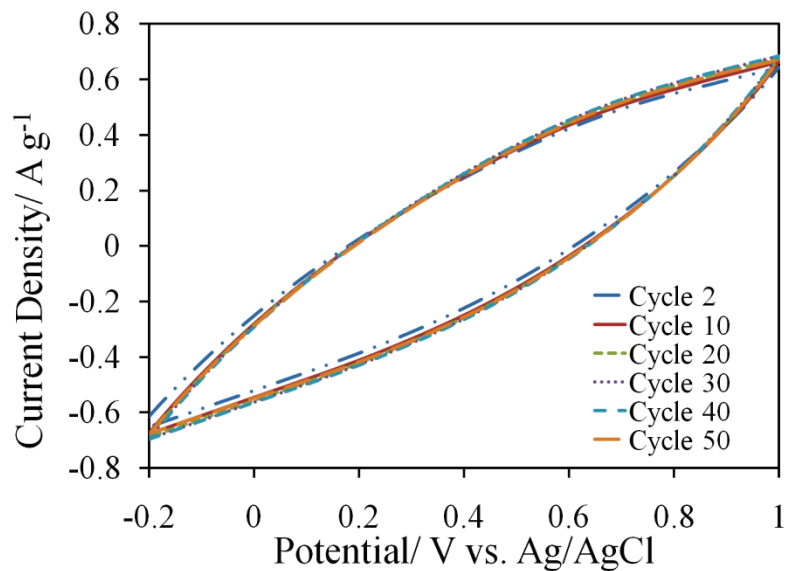
Figure 48: Electrodeposition of RuO$_2$·xH$_2$O onto carbon cloth at 4 mV s^{-1}, in 5 mM RuCl$_3$·xH$_2$O.

There is little change in the shape or angle of the cyclic voltammogram throughout the electrodeposition process, save for a minor change between cycles 2 and 10. However, this time when a cyclic voltammogram was performed on the electrode at 1 mV s^{-1} in 1.0 M H$_2$SO$_4$ after the deposition, there was a clear increase in the capacitance compared to before the deposition, shown in Figure 49.

Figure 49: Differential capacitance profile of carbon cloth before and after electrodeposition at 4 mV s^{-1}, in 5 mM RuCl$_3$·xH$_2$O. Also shown is the calculated RuO$_2$ component capacitance.
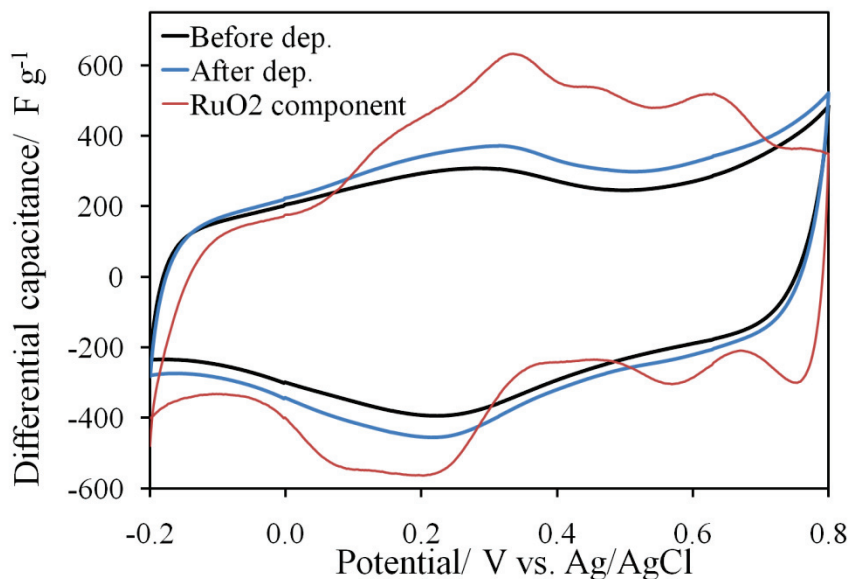
The current-density axis on the cyclic voltammogram was converted to differential capacitance by dividing by the sweep rate. After the electrodeposition, the electrode was dried in air overnight. From the mass difference before and after deposition, the loading of RuO$_2$·xH$_2$O was determined to be *ca.* 12 %. From the loading, the specific capacitance of the RuO$_2$·xH$_2$O component was determined, and is also presented in Figure 49. The RuO$_2$·xH$_2$O component had a maximum capacitance of *ca.* 632 F g^{-1} and an average of *ca.* 366 F g^{-1} on the oxidation curve and 350 F g^{-1} on the reduction curve. The electrodeposition of RuO$_2$·xH$_2$O onto carbon cloth was successful over 50 cycles at 4 mV s^{-1}. However, the areas of the carbon onto which the RuO$_2$·xH$_2$O deposited was not determined.

In an attempt to improve on the electrodeposition and potentially reduce the resistivity of the deposition bath, the RuCl$_3$·xH$_2$O concentration was increased to 25 mM,

while all other variables were unchanged. The cyclic voltammograms for the electrodeposition are shown in Figure 50.
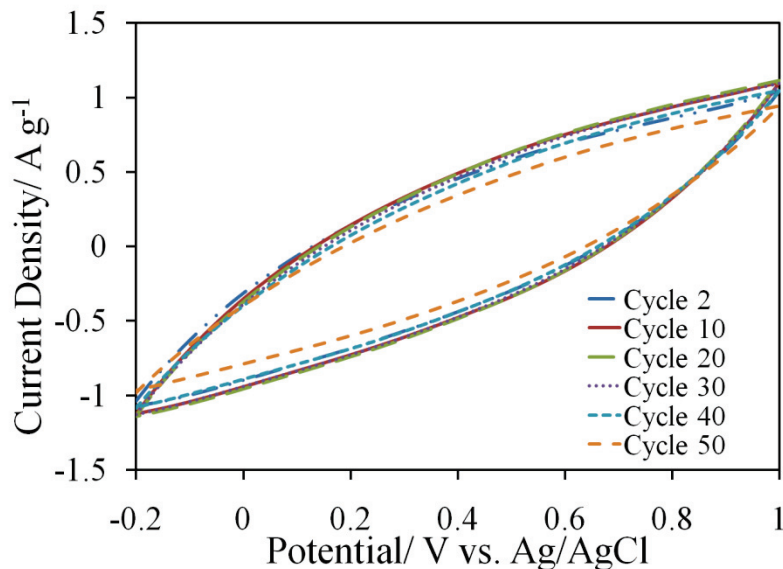

Figure 50: Electrodeposition of the RuO$_2$·xH$_2$O onto a carbon cloth electrode at 4 mV s^{-1}, in 25 mM RuCl$_3$·xH$_2$O.

The deposition bath with 25 mM RuCl$_3$·xH$_2$O had similar resistivity characteristics to the bath with 5 mM RuCl$_3$·xH$_2$O, indicating that the concentration of RuCl$_3$·xH$_2$O may not significantly affect the resistivity. During this deposition, the current did not remain constant as in the previous deposition. Regarding the current at 1 V, there is an initial increase until cycle 20, followed by a decreasing current for the rest of the deposition. A change in the deposition current has been observed in literature, and it was hypothesised that it could be due to the complex activity of chloride forming Ru(OH)$_\delta$Cl$_{3-\delta}$·cH$_2$O in the deposition solution as the RuO$_2$·xH$_2$O forms,[38, 70] due to a decrease in the RuCl$_3$·xH$_2$O concentration as the deposition proceeds. These factors may be influencing the deposition in this synthesis. The cyclic voltammogram performed on

the electrode at 1 mV s^{-1} in 1.0 M H$_2$SO$_4$ after the deposition showed a clear increase in

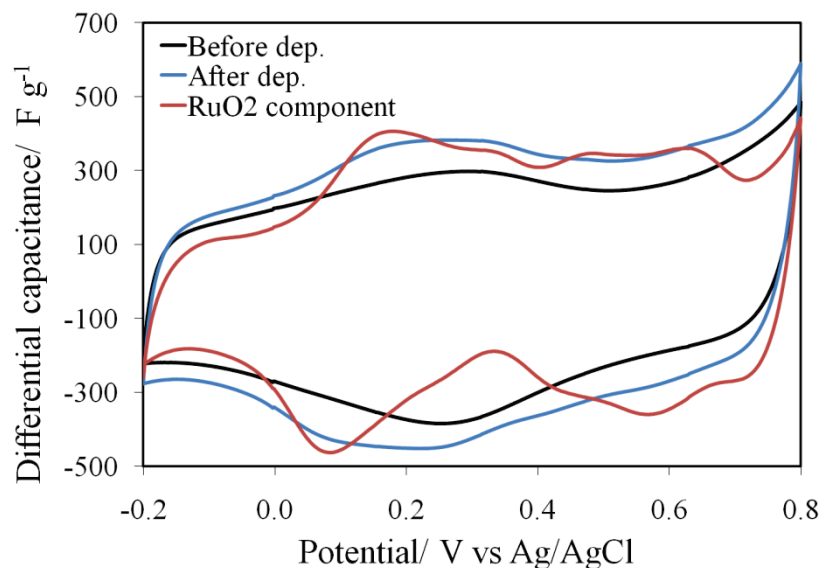the capacitance compared to before the deposition, shown in Figure 51.

Figure 51: Differential capacitance profile of carbon cloth before and after electrodeposition at 4 mV s^{-1}, in 25 mM RuCl$_3$·xH$_2$O. Also shown is the calculated RuO$_2$ component capacitance.

Once again the difference in mass of the electrode before and after deposition was

used to determine the loading of RuO$_2$·xH$_2$O, and it was found to be *ca.* 24 %. Although

the loading of the RuO$_2$·xH$_2$O is greater than with the previous synthesis, the RuO$_2$·xH$_2$O

component is used less efficiently and displays a maximum capacitance of *ca.* 464 F g^{-1},

and an average of *ca.* 277 F g^{-1} on the oxidation curve and *ca.* 273 F g^{-1} on the reduction

curve. It has been observed in literature that a higher loading of RuO$_2$·xH$_2$O can cause

decreased electrical contact with the substrate and poorer utilization of the RuO$_2$·xH$_2$O

component,[13] which may be occurring in this synthesis. Also, a higher loading of

RuO$_2$·xH$_2$O may also block or restrict electrolyte access to parts of the carbon surface

and cause the capacitance from the carbon component to decrease.[13] This is not

accounted for in the calculation of the specific capacitance of the RuO$_2$·xH$_2$O component.

Therefore, the specific capacitance of the $RuO_2 \cdot xH_2O$ component may be higher than calculated.

For the next deposition, the original $RuCl_3 \cdot xH_2O$ concentration of 5 mM was used, and the sweep rate was increased to 10 mV s^{-1}. It was hypothesized that even if the deposition bath is quite resistive, an increased sweep rate of 10 mV s^{-1} (relative to the 4 mV s^{-1} deposition with 5 mM $RuCl_3 \cdot xH_2O$) may deposit $RuO_2 \cdot xH_2O$ on a different area of the carbon (mostly in the mesopores) and cause a different capacitance. The cyclic voltammograms for the deposition are shown in Figure 52.

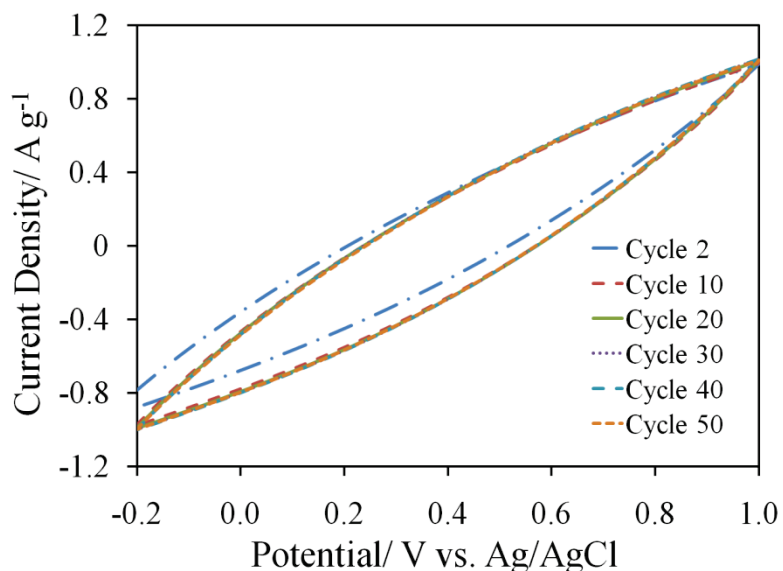**Figure 52: Electrodeposition onto carbon cloth at 10 mV s^{-1}, in 5 mM $RuCl_3 \cdot xH_2O$.**

The current during the deposition remains constant, save for a change between cycles 2 and 10, as with the previous 5 mM $RuCl_3 \cdot xH_2O$ synthesis. The cyclic voltammograms performed on the electrode at 1 mV s^{-1} in 1.0 M H_2SO_4 before and after deposition are shown in Figure 53.
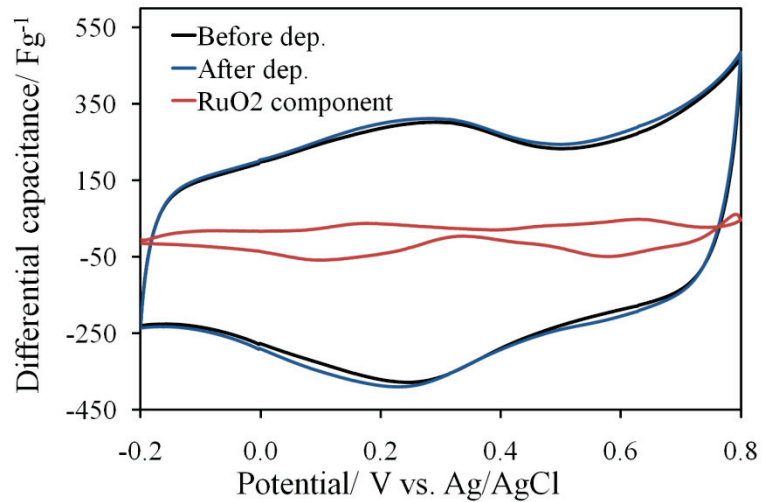
Figure 53: Differential capacitance profile of carbon cloth before and after electrodeposition at 10 mV s⁻¹, in 5 mM RuCl₃·xH₂O. Also shown is the calculated RuO₂ component capacitance.

The difference in mass of the electrode between before and after deposition showed that the loading of $RuO_2 \cdot xH_2O$ was *ca*. 35 %. The specific capacitance of the $RuO_2 \cdot xH_2O$ component is also shown in Figure 53, and has a maximum of *ca.* 61 F g⁻¹, and an average of *ca.* 28 F g⁻¹ on both the oxidation and reduction curves. The faster sweep rate appears to deposit more $RuO_2 \cdot xH_2O$ than the slower sweep rate (35 % loading vs. 11 % loading), after the same number of cycles. This is counter to what is expected as a slow sweep rate should deposit a larger amount of RuO_2 than a faster sweep rate, after the same amount of cycles.[71] The exact reason for the discrepancy is unknown, however, it could be related to the drying process of the electrode. The carbon is very porous, and perhaps electrolyte has remained in the micropores, making the loading appear higher. Regardless, as with the previous synthesis, the small capacitance of the $RuO_2 \cdot xH_2O$ could be due to poor electrical contact between the $RuO_2 \cdot xH_2O$ component and the carbon cloth substrate,[13] possibly caused by the fast deposition sweep rate. Also, the carbon

component could have a decreased capacitance, causing the capacitance of the $RuO_2 \cdot xH_2O$ component to appear lower, as described above.

To obtain surface areas, single point BET measurements were performed on the carbon cloth electrodes. The electrodes which had a deposition bath concentration of 5 mM $RuCl_3 \cdot xH_2O$ and sweep rates of 4 and 10 mV s^{-1} have surface areas of 897 ± 1 m^2 g^{-1} and 749 ± 1 m^2 g^{-1}, respectively. The unloaded carbon cloth has a surface area of 2131 m^2 g^{-1}, determined in a previous study. This could indicate that there is less available surface area on the loaded electrodes, especially on the 10 mV s^{-1} electrode, due to a blocking of the pores by the loaded $RuO_2 \cdot xH_2O$. It is expected that the 10 mV s^{-1} electrode has a smaller surface area as a higher loading was obtained for this sample, and $RuO_2 \cdot xH_2O$ has a much smaller surface area (*ca*. 200 m^2 g^{-1}) than the carbon cloth, discussed earlier.[68] However the smaller surface area observed for the loaded electrodes could simply be a result of the larger mass of $RuO_2 \cdot xH_2O$ compared to carbon. Therefore, the normalized surface area of the 35 % loaded electrode would appear lower because it would take less composite to reach the same mass as the 11 % loaded electrode, and similarly for both loaded carbon cloth electrodes compared with the non-loaded carbon cloth.

7.4 CONCLUSIONS

The electrodeposition of $RuO_2 \cdot xH_2O$ onto Au foil was successful, however, the $RuO_2 \cdot xH_2O$ formed was not stable in the acid electrolyte and dissolved over time. The deposition onto carbon cloth was found to be optimum when the deposition bath contained 5 mM $RuCl_3 \cdot xH_2O$, 0.01 M HCl, and 0.1 M KCl, with the initial pH of the bath adjusted to 2.5 via NaOH addition. The deposition was performed at 50 °C, with 50 cycles at 4 mV s^{-1}, and the $RuO_2 \cdot xH_2O$ component had a maximum specific capacitance

of 632 F g^{-1}. However, the deposition did not produce $RuO_2 \cdot xH_2O$ with a high specific capacitance when other sweep rates were employed. The resistance of the deposition bath was high, and the changes in current with increasing cycle number were not easily observed in the cyclic voltammograms. Deposition onto specific areas of the carbon was not successfully achieved, as intended, and therefore further studies need to be performed.

CHAPTER 8: FUTURE WORK

8.1 *IN SITU* ELECTROCHEMICAL-XAS

The noise level in the *in situ* electrochemical-XAS data must be minimized to produce more reliable data. A custom electrochemical cell has been designed and fabricated out of PTFE, but not yet utilized, which will reduce the amount of electrolyte through which the X-ray beam passes, and thus reduce beam attenuation and theoretically increase the data quality. Also, an electrolyte which contains less oxygen and more carbon (perhaps an organic electrolyte or a mixed organic/aqueous electrolyte) is preferred as it may have a smaller absorption coefficient and therefore result in less beam attenuation and higher quality data.

Also, the synthesis of RuO_2 nanoparticles which are fully or almost fully electroactive is desired, to compare the structural changes between a bulk and nano scale sample with changing potential.

8.2 ELECTRODEPOSITION

Further optimization of the deposition conditions is required for the electrodeposition of $RuO_2 \cdot xH_2O$ onto carbon cloth. This may involve altering the deposition bath so that deposition will occur successfully at multiple sweep rates with a high capacitance of the $RuO_2 \cdot xH_2O$. The deposition bath must be altered so that the cyclic voltammograms of the deposition show less resistivity, as the changes in current with cycle number during deposition has been shown to provide information on the film produced. Also, the composites produced need to be extensively characterized using a variety of techniques such as SEM, TEM, SAXS and BET to determine exactly where the RuO_2 is on the carbon.

CHAPTER 9: CONCLUSIONS

Changes in the structure of $RuO_2 \cdot xH_2O$ in RuO_2/carbon composites were induced by varying the annealing temperature, as well as altering electrochemical potentials and thoroughly characterized with a library of techniques including XRD, TGA, TEM, EXAFS (Ru K-edge), XANES (Ru K and L-edge), *ab initio* calculations, cyclic voltammetry and *in situ* electrochemical-XAS.

The effect of annealing temperature on the structure of $RuO_2 \cdot xH_2O$ nanoparticles in a RuO_2/carbon composite was investigated in detail. The RuO_2 transitions from a heavily hydrated to slightly hydrated form at *ca.* 100-150 °C, and further reduced to metallic Ru at *ca.* 350 °C. The latter phase transition occurs at lower temperatures than for bulk RuO_2. The RuO_2 nanoparticles had a higher stability against aggregation with respect to temperature than metallic Ru nanoparticles, which is proposed to be due to Ru-O-C bonds which can stabilize RuO_2 nanoparticles. Ru L_3-edge data showed that the phase transition from RuO_2 to metallic Ru occurs via an inside-out process, with the center of the RuO_2 particle becoming metallic and the surface remaining as crystalline metal oxide. Further analysis and characterization showed a decrease in the pore volume of the mesoporous carbon powder after loading with RuO_2, but no definite conclusions could be made as to whether the RuO_2 is actually filling the pores or not. The specific capacitance of the RuO_2 component in the 150 °C nanocomposite was low, suggesting that only a small amount of the RuO_2 present is electroactive.

An *in situ* electrochemical-XAS technique was developed in this thesis. Data from the *in situ* electrochemical-XAS support the above finding that only a small amount of the RuO_2 present in the 150 °C nanocomposite is electroactive. Specifically, no change in

the Ru K-edge XANES was observed when the applied potential to the 150 °C composite electrode was changed, and no reliable changes were observed in the EXAFS. The *in situ* electrochemical-XAS studies were able to detect changes in both the XANES and EXAFS regions for the Ru K-edge of bulk $RuO_2 \cdot xH_2O$. The XANES changes were subtle, but similar to those seen in literature. For the EXAFS, as the potential of the working electrode was increased, the intensity of the Ru-O shell decreased, possibly due to an increase in disorder of the Ru-O shell with increasing potential.

The electrodeposition of $RuO_2 \cdot xH_2O$ onto Au foil was initially successful, however, the $RuO_2 \cdot xH_2O$ formed was not stable in the acid electrolyte. The deposition onto carbon cloth was found to be optimum when the deposition bath contained 5 mM $RuCl_3 \cdot xH_2O$, 0.01 M HCl, and 0.1 M KCl, with the initial pH of the bath adjusted to 2.5 via NaOH addition. The deposition was performed at 50 °C, with 50 cycles at 4 mV s^{-1}, and the $RuO_2 \cdot xH_2O$ component had a maximum specific capacitance of 632 F g^{-1}. However, deposition on different areas of the carbon with different sweep rates, as intended, was not successfully achieved.

Overall, much information has been gained on the way RuO_2 behaves while in a carbon composite. It has been shown that RuO_2 nanoparticles in a composite have a different response to high temperatures than their bulk counterparts. When depositing RuO_2 electrochemically, it is important to understand that the resistance of the deposition bath is greater in the pores of a carbon cloth than on a planar substrate, and optimization of the deposition conditions are likely substrate dependent.

REFERENCES

(1) Winter, M.; Brodd, R. J. What are Batteries, Fuel Cells, and Supercapacitors? *Chem. Rev. (Washington, DC, U. S.)* 2004, *104*, 4245-4269.

(2) Conway, B. E. In *Electrochemical Supercapacitors: Scientific Fundamentals and Technological Applications;* Kluwer Academic/ Plenium Publishers: NY, 1999.

(3) Frackowiak, E. Carbon Materials for Supercapacitor Application. *Phys. Chem. Chem. Phys.* 2007, *9*, 1774-1785.

(4) Conway, B. E.; Pell, W. G. Double-Layer and Pseudocapacitance Types of Electrochemical Capacitors and their Applications to the Development of Hybrid Devices. *J. Solid State Electrochem.* 2003, *7*, 637-644.

(5) Atkins, P. W. In *Physical Chemistry;* W. H. Freeman and Company: NY, 1994.

(6) Conway, B. E. Transition from Supercapacitor to Battery Behavior in Electrochemical Energy-Storage. *J. Electrochem. Soc.* 1991, *138*, 1539-1548.

(7) Zheng, J. P.; Jow, T. R. A New Charge Storage Mechanism for Electrochemical Capacitors. *J. Electrochem. Soc.* 1995, *142*, L6-L8.

(8) Hu, C. C.; Chen, W. C. Effects of Substrates on the Capacitive Performance of RuOx Center Dot nH(2)O and Activated Carbon-RuOx Electrodes for Supercapacitors. *Electrochim. Acta* 2004, *49*, 3469-3477.

(9) Liu, X.; Pickup, P. G. Carbon Fabric Supported Manganese and Ruthenium Oxide Thin Films for Supercapacitors. *J. Electrochem. Soc.* 2011, *158*, A241-A249.

(10) McKeown, D. A.; Hagans, P. L.; Carette, L. P. L.; Russell, A. E.; Swider, K. E.; Rolison, D. R. Structure of Hydrous Ruthenium Oxides: Implications for Charge Storage. *J. Phys. Chem. B* 1999, *103*, 4825-4832.

(11) Hu, C.; Chen, W.; Chang, K. How to Achieve Maximum Utilization of Hydrous Ruthenium Oxide for Supercapacitors. *J. Electrochem. Soc.* 2004, *151*, A281-A290.

(12) Dmowski, W.; Egami, T.; Swider-Lyons, K. E.; Love, C. T.; Rolison, D. R. Local Atomic Structure and Conduction Mechanism of Nanocrystalline Hydrous RuO_2 from X-Ray Scattering. *J. Phys. Chem. B* 2002, *106*, 12677-12683.

(13) Liu, X.; Pickup, P. G. Ru oxide/carbon Fabric Composites for Supercapacitors. *J. Solid State Electrochem.* 2010, *14*, 231-240.

(14) Kim, H.; Popov, B. N. Characterization of Hydrous Ruthenium oxide/carbon Nanocomposite Supercapacitors Prepared by a Colloidal Method. *J. Power Sources* 2002, *104*, 52-61.

(15) Sato, Y.; Yomogida, K.; Nanaumi, T.; Kobayakawa, K.; Ohsawa, Y.; Kawai, M. Electrochemical Behavior of Activated-Carbon Capacitor Materials Loaded with Ruthenium Oxide. *Electrochem. Solid-State Lett.* 2000, *3*, 113-116.

(16) Pico, F.; Morales, E.; Fernandez, J. A.; Centeno, T. A.; Ibanez, J.; Rojas, R. M.; Amarilla, J. M.; Rojo, J. M. Ruthenium oxide/carbon Composites with Microporous Or Mesoporous Carbon as Support and Prepared by Two Procedures. A Comparative Study as Supercapacitor Electrodes. *Electrochim. Acta* 2009, *54*, 2239-2245.

(17) Kim, B. C.; Wallace, G. G.; Yoon, Y. I.; Ko, J. M.; Too, C. O. Capacitive Properties of RuO_2 and Ru-Co Mixed Oxide Deposited on Single-Walled Carbon Nanotubes for High-Performance Supercapacitors. *Synth. Met.* 2009, *159*, 1389-1392.

(18) Zhang, J.; Jiang, D.; Chen, B.; Zhu, J.; Jiang, L.; Fang, H. Preparation and Electrochemistry of Hydrous Ruthenium oxide/active Carbon Electrode Materials for Supercapacitor. *J. Electrochem. Soc.* 2001, *148*, A1362-A1367.

(19) Liu, X.; Huber, T. A.; Kopac, M. C.; Pickup, P. G. Ru oxide/carbon Nanotube Composites for Supercapacitors Prepared by Spontaneous Reduction of Ru(VI) and Ru(VII). *Electrochim. Acta* 2009, *54*, 7141-7147.

(20) Hu, C.; Huang, Y.; Chang, K. Annealing Effects on the Physicochemical Characteristics of Hydrous Ruthenium and Ruthenium-Iridium Oxides for Electrochemical Supercapacitors. *J. Power Sources* 2002, *108*, 117-127.

(21) Hu, C.; Liu, M.; Chang, K. Anodic Deposition of Hydrous Ruthenium Oxide for Supercapacitors: Effects of the AcO- Concentration, Plating Temperature, and Oxide Loading. *Electrochim. Acta* 2008, *53*, 2679-2687.

(22) Foelske, A.; Barbieri, O.; Hahn, M.; Kotz, R. An X-Ray Photoelectron Spectroscopy Study of Hydrous Ruthenium Oxide Powders with various Water Contents for Supercapacitors. *Electrochem. Solid-State Lett.* 2006, *9*, A268-A272.

(23) Hiemenz, P. C.; Rajagopalan, R. In *Principles of Colloid and Surface Chemistry;* Marcel Dekker, Inc: NY, 1997.

(24) Skoog, D. A.; Leary, J. J. In *Principles of Instrumental Analysis;* Harcourt Brace College Publishers: NY, 1992.

(25) Skoog, D. A.; Holler, F. J.; Nieman, T. A. In *Principles of Instrumental Analysis;* Thomson Learning, Inc.: Toronto, Ontario, 1998.

(26) Hoffman, E. N.; Yushin, G.; El-Raghy, T.; Gogotsi, Y.; Barsoum, M. W. Micro and Mesoporosity of Carbon Derived from Ternary and Binary Metal Carbides. *Microporous Mesoporous Mat.* 2008, *112*, 526-532.

(27) Lang, X.; Dalai, A. K.; Bakhshi, N. N.; Reaney, M. J.; Hertz, P. B. Preparation and Characterization of Bio-Diesels from various Bio-Oils. *Bioresour. Technol.* 2001, *80*, 53-62.

(28) Langford, J. I.; Wilson, A. J. C. Scherrer After 60 Years - Survey and some New Results in Determination of Crystallite Size. *J. Appl. Crystallogr.* 1978, *11*, 102-113.

(29) Stevens, D. A.; Dahn, J. R. An in Situ Small-Angle X-Ray Scattering Study of Sodium Insertion into a Nanoporous Carbon Anode Material within an Operating Electrochemical Cell. *J. Electrochem. Soc.* 2000, *147*, 4428-4431.

(30) Sandi, G.; Thiyagarajan, P.; Winans, R. E.; Carrado, K. A. Small Angle Neutron and X-Ray Scattering Studies of Carbons Prepared using Inorganic Templates. *Abstr. Pap. Am. Chem. Soc.* 1997, *214*, 58-FUEL.

(31) Stevens, D. A.; Zhang, S.; Chen, Z.; Dahn, J. R. On the Determination of Platinum Particle Size in Carbon-Supported Platinum Electrocatalysts for Fuel Cell Applications. *Carbon* 2003, *41*, 2769-2777.

(32) Bertin, E. P. In *Introduction to X-Ray Spectrometric Analysis;* Plenum Press: NY, 1978.

(33) Bunker, G. In *Introduction to XAFS: A Practical Guide to X-ray Absorption Fine Structure Spectroscopy;* Cambridge University Press: UK, 2010.

(34) Conley, M.; Palmer, D. CrystalMaker. 2006, *1.3.2*.

(35) Ankudinov, A. L.; Ravel, B.; Rehr, J. J.; Conradson, S. D. Real-Space Multiple-Scattering Calculation and Interpretation of x-Ray-Absorption Near-Edge Structure. *Phys. Rev. B: Condens. Matter Mater. Phys.* 1998, *58*, 7565-7576.

(36) Ressler, T. WinXAS. 2005, *3.11*.

(37) Bockris, J. O.; Reddy, A. K. N.; Gamboa-Aldeco, M. E.; Editors In *Modern Electrochemistry: Fundamentals of Electrodics.* Section Title: Electrochemistry; Kluwer Academic/ Plenum Publishers: NY, 2001; Vol. 2A.

(38) Hu, C.; Huang, Y. Cyclic Voltammetric Deposition of Hydrous Ruthenium Oxide for Electrochemical Capacitors. *J. Electrochem. Soc.* 1999, *146*, 2465-2471.

(39) Pico, F.; Ibanez, J.; Lillo-Rodenas, M. A.; Linares-Solano, A.; Rojas, R. M.; Amarilla, J. M.; Rojo, J. M. Understanding $RuO_2 \cdot xH_2O$/carbon Nanofiber Composites as Supercapacitor Electrodes. *J. Power Sources* 2008, *176*, 417-425.

(40) Zhang, P.; Naftel, S. J.; Sham, T. K. Multichannel Detection x-Ray Absorption Near Edge Structures Study on the Structural Characteristics of Dendrimer-Stabilized CdS Quantum Dots. *J. Appl. Phys.* 2001, *90*, 2755-2759.

(41) Wang, X.; Ruan, D.; Wang, P.; Lu, Y. Pseudo-Capacitance of Ruthenium oxide/carbon Black Composites for Electrochemical Capacitors. *J. Univ. Sci. Technol. Beijing* 2008, *15*, 816-821.

(42) Li, H.; Wang, R.; Cao, R. Physical and Electrochemical Characterization of Hydrous Ruthenium oxide/ordered Mesoporous Carbon Composites as Supercapacitor. *Microporous Mesoporous Mater.* 2008, *111*, 32-38.

(43) Sun, Z.; Liu, Z.; Han, B.; Wang, Y.; Du, J.; Xie, Z.; Han, G. Fabrication of Ruthenium-Carbon Nanotube Nanocomposites in Supercritical Water. *Adv. Mater. (Weinheim, Ger.)* 2005, *17*, 928-932.

(44) Su, F.; Lee, F. Y.; Lv, L.; Liu, J.; Tian, X. N.; Zhao, X. S. Sandwiched ruthenium/carbon Nanostructures for Highly Active Heterogeneous Hydrogenation. *Adv. Funct. Mater.* 2007, *17*, 1926-1931.

(45) Campbell, P. F.; Ortner, M. H.; Anderson, C. J. Differential Thermal Analysis and Thermogravimetric Analysis of Fission Product Oxides and Nitrates to 1500 Deg. *Anal. Chem.* 1961, *33*, 58-61.

(46) Murray, J. P.; Steinfeld, A.; Fletcher, E. A. Metals, Nitrides, and Carbides Via Solar Carbothermal Reduction of Metal-Oxides. *Energy* 1995, *20*, 695-704.

(47) Panic, V.; Vidakovic, T.; Gojkovic, S.; Dekanski, A.; Milonjic, S.; Nikolic, B. The Properties of Carbon-Supported Hydrous Ruthenium Oxide obtained from RuOxHy Sol. *Electrochim. Acta* 2003, *48*, 3805-3813.

(48) Zhou, J. G.; Fang, H. T.; Hu, Y. F.; Sham, T. K.; Wu, C. X.; Liu, M.; Li, F. Immobilization of RuO2 on Carbon Nanotube: An X-Ray Absorption Near-Edge Structure Study. *J. Phys. Chem. C* 2009, *113*, 10747-10750.

(49) Wu, Z.; Wang, D.; Ren, W.; Zhao, J.; Zhou, G.; Li, F.; Cheng, H. Anchoring Hydrous RuO_2 on Graphene Sheets for High-Performance Electrochemical Capacitors. *Adv. Funct. Mater.* 2010, *20*, 3595-3602.

(50) Zielke, U.; Huttinger, K. J.; Hoffman, W. P. Surface-Oxidized Carbon Fibers .1. Surface Structure and Chemistry. *Carbon* 1996, *34*, 983-998.

(51) Rolison, D. R.; Hagans, P. L.; Swider, K. E.; Long, J. W. Role of Hydrous Ruthenium Oxide in Pt-Ru Direct Methanol Fuel Cell Anode Electrocatalysts: The Importance of Mixed electron/proton Conductivity. *Langmuir* 1999, *15*, 774-779.

(52) Barbieri, O.; Hahn, M.; Foelske, A.; Koetz, R. Effect of Electronic Resistance and Water Content on the Performance of RuO_2 for Supercapacitors. *J. Electrochem. Soc.* 2006, *153*, A2049-A2054.

(53) Chakroune, N.; Viau, G.; Ammar, S.; Poul, L.; Veautier, D.; Chehimi, M. M.; Mangeney, C.; Villain, F.; Fievet, F. Acetate- and Thiol-Capped Monodisperse Ruthenium Nanoparticles: XPS, XAS, and HRTEM Studies. *Langmuir* 2005, *21*, 6788-6796.

(54) Zhan, B.; White, M. A.; Sham, T.; Pincock, J. A.; Doucet, R. J.; Rao, K. V. R.; Robertson, K. N.; Cameron, T. S. Zeolite-Confined Nano-RuO2: A Green, Selective, and Efficient Catalyst for Aerobic Alcohol Oxidation. *J. Am. Chem. Soc.* 2003, *125*, 2195-2199.

(55) Altwasser, S.; Glaeser, R.; Lo, A. S.; Liu, P.; Chao, K.; Weitkamp, J. Incorporation of RuO_2 Nanoparticles into MFI-Type Zeolites. *Microporous Mesoporous Mater.* 2006, *89*, 109-122.

(56) Harada, M.; Takahashi, S. Synthesis of Ruthenium Particles by Photoreduction in Polymer Solutions. *J. Colloid Interface Sci.* 2008, *325*, 1-6.

(57) Trudel, S.; Crozier, E. D.; Gordon, R. A.; Budnik, P. S.; Hill, R. H. X-Ray Absorption Fine Structure Study of Amorphous Metal Oxide Thin Films Prepared by Photochemical Metalorganic Deposition. *J. Solid State Chem.* 2011, *184*, 1025-1035.

(58) MacDonald, M. A.; Zhang, P.; Chen, N.; Qian, H.; Jin, R. Solution-Phase Structure and Bonding of Au(38)(SR)(24) Nanoclusters from X-Ray Absorption Spectroscopy. *J. Phys. Chem. C* 2011, *115*, 65-69.

(59) Bugaev, L. A.; Avakyan, L. A.; Makhova, M. S.; Dmitrienko, E. V.; Alekseenko, I. B. Resolution of Interatomic Distances by Fourier Analysis of Short Energy-Range X-Ray Absorption Spectra. *Opt. Spectrosc.* 2008, *105*, 881-888.

(60) Zanchet, D.; Tolentino, H.; Alves, M. C. M.; Alves, O. L.; Ugarte, D. Inter-Atomic Distance Contraction in Thiol-Passivated Gold Nanoparticles. *Chem. Phys. Lett.* 2000, *323*, 167-172.

(61) Zhang, P.; Kim, P. S.; Sham, T. K. Nanostructured CdS Prepared on Porous Silicon Substrate: Structure, Electronic, and Optical Properties. *J. Appl. Phys.* 2002, *91*, 6038-6043.

(62) Hu, Z.; von Lips, H.; Golden, M. S.; Fink, J.; Kaindl, G.; de Groot, F. M. F.; Ebbinghaus, S.; Reller, A. Multiplet Effects in the Ru L-2,L-3 x-Ray-Absorption Spectra of Ru(IV) and Ru(V) Compounds. *Phys. Rev. B* 2000, *61*, 5262-5266.

(63) Stefan, I. C.; Mo, Y. B.; Antonio, M. R.; Scherson, D. A. In Situ Ru L-II and L-III-Edge X-Ray Absorption Near Edge Structure of Electrodeposited Ruthenium Dioxide Films. *Electrochemical Capacitor and Hybrid Power Sources* 2002, *2002*, 291-296.

(64) Mo, Y. B.; Antonio, M. R.; Scherson, D. A. In Situ Ru K-Edge X-Ray Absorption Fine Structure Studies of Electroprecipitated Ruthenium Dioxide Films with Relevance to Supercapacitor Applications. *J. Phys. Chem. B* 2000, *104*, 9777-9779.

(65) Guittonneau, F.; Abdelouas, A.; Grambow, B.; Huclier, S. The Effect of High Power Ultrasound on an Aqueous Suspension of Graphite. *Ultrason. Sonochem.* 2010, *17*, 391-398.

(66) Oickle, A. M.; Goertzen, S. L.; Hopper, K. R.; Abdalla, Y. O.; Andreas, H. A. Standardization of the Boehm Titration: Part II. Method of Agitation, Effect of Filtering and Dilute Titrant. *Carbon* 2010, *48*, 3313-3322.

(67) Sing, K. S. W. Physisorption of Nitrogen by Porous Materials. *J. Porous Mater.* 1995, *2*, 5-8.

(68) Oh, S. H.; Nazar, L. F. Direct Synthesis of Electroactive Mesoporous Hydrous Crystalline RuO_2 Templated by a Cationic Surfactant. *J. Mater. Chem.* 2010, *20*, 3834-3839.

(69) Mo, Y.; Bae, I. T.; Sarangapani, S.; Scherson, D. A. In Situ Ru K-Edge x-Ray Absorption Spectroscopy of a High-Area Ruthenium Dioxide Electrode in a Nafion-Based Supercapacitor Environment. *J. Solid State Electrochem.* 2003, *7*, 572-575.

(70) Hu, C. C.; Chang, K. H. Cyclic Voltammetric Deposition of Hydrous Ruthenium Oxide for Electrochemical Supercapacitors: Effects of the Chloride Precursor Transformation. *J. Power Sources* 2002, *112*, 401-409.

(71) Hu, C. C.; Huang, Y. H. Effects of Preparation Variables on the Deposition Rate and Physicochemical Properties of Hydrous Ruthenium Oxide for Electrochemical Capacitors. *Electrochim. Acta* 2001, *46*, 3431-3444.

(72) Patake, V. D.; Lokhande, C. D.; Joo, O. S. Electrodeposited Ruthenium Oxide Thin Films for Supercapacitor: Effect of Surface Treatments. *Appl. Surf. Sci.* 2009, *255*, 4192-4196.

(73) Kim, I.; Kim, J.; Lee, Y.; Kim, K. Synthesis and Characterization of Electrochemically Prepared Ruthenium Oxide on Carbon Nanotube Film Substrate for Supercapacitor Applications. *J. Electrochem. Soc.* 2005, *152*, A2170-A2178.
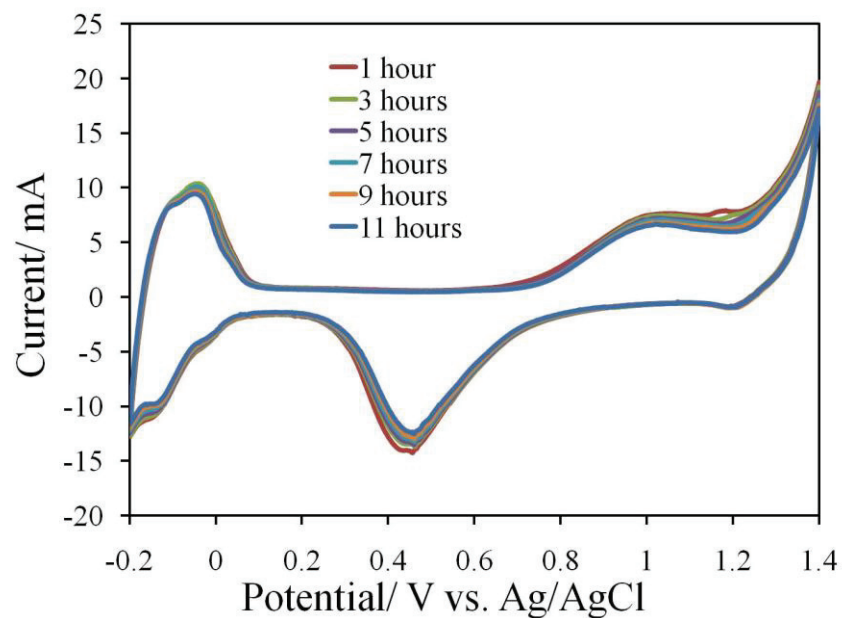
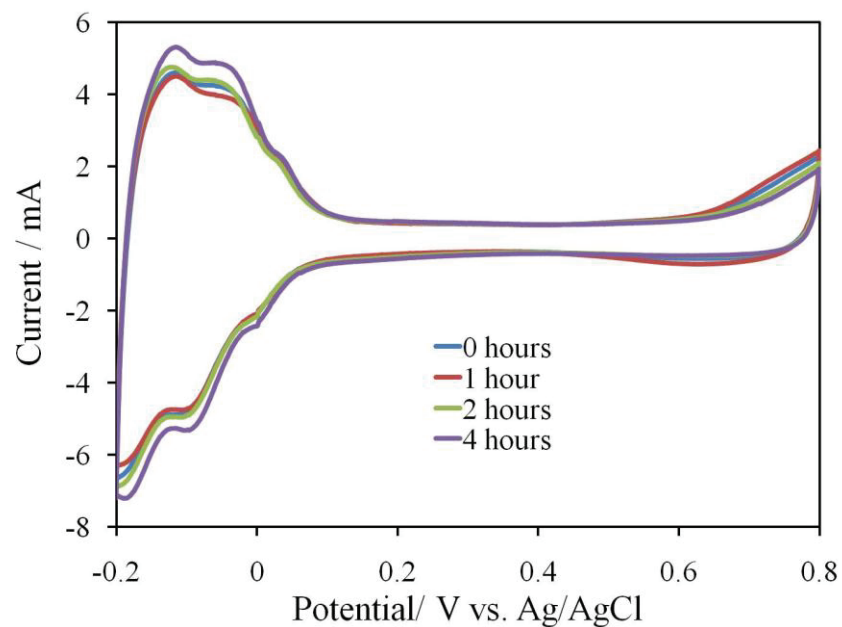**Figure A.1: Cyclic voltammograms of platinum in 1.0 M H$_2$SO$_4$, in the PTFE electrochemical cell.**

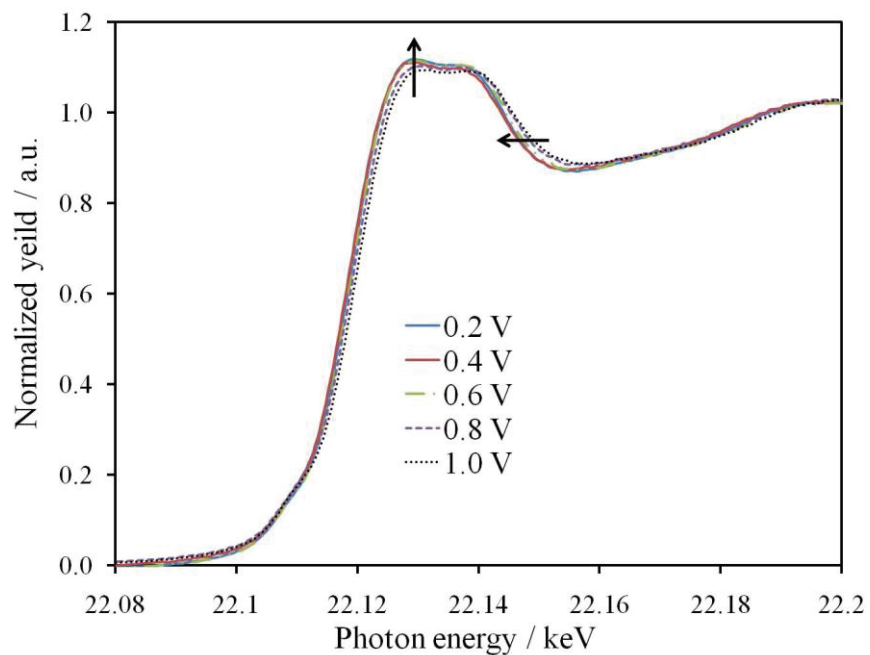**Figure A.2: Cyclic voltammograms of platinum in 1.0 M H$_2$SO$_4$ after N$_2$ bubbling has been stopped.**

Figure A.3: In situ XANES spectra for bulk RuO$_2$·xH$_2$O, collected at 0.2, 0.4, 0.6, 0.8, and 1.0 V.

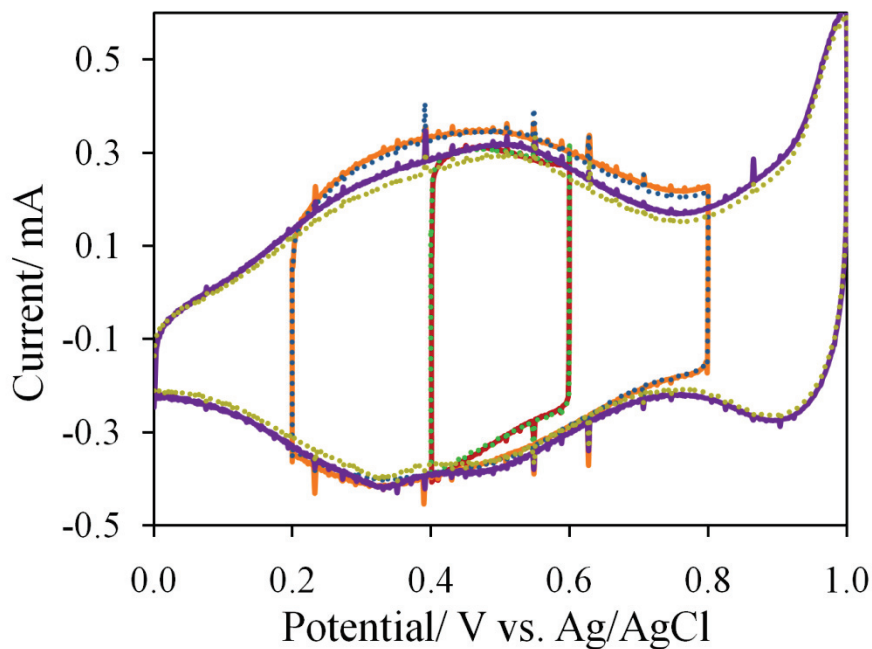**Figure B.1: Cyclic voltammograms of RuO₂·xH₂O electrodeposited on Au foil annealed at 50 °C for one hour, at 5 mV s^{-1} in 1.0 M H₂SO₄, with various potential windows.**
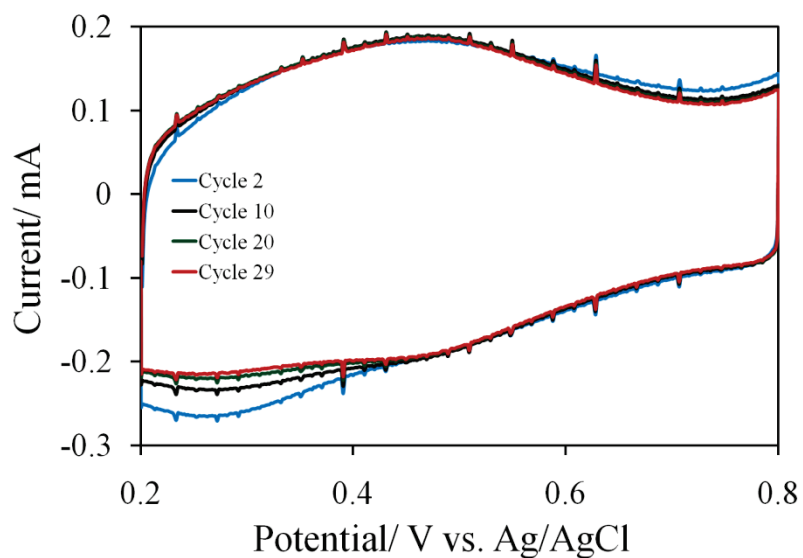

Figure B.2: Cyclic voltammograms at 10 mV s^{-1} of RuO₂·xH₂O electrodeposited on Au foil annealed in 0.5 M H₂SO₄.

APPENDIX C: COPYRIGHT PERMISSION

Chapter 4: Reproduced with permission from The Journal of Physical Chemistry C, submitted for publication. Unpublished work copyright 2011 American Chemical Society.

Chapter 6: Reproduced in part with permission from The Journal of Physical Chemistry C, submitted for publication. Unpublished work copyright 2011 American Chemical Society.